

https://dspace.org/

Physico-chemistry of ceria-coated nickel rich manganese cobalt oxides as cathode materials for lithium-ion batteries

Seotsanyana-Mokhosi, Itumeleng

2024-12

University of the Witwatersrand, Johannesburg

https://hdl.handle.net/10539/48709

Seotsanyana-Mokhosi, Itumeleng. (2024). Physico-chemistry of ceria-coated nickel rich manganese cobalt oxides as cathode materials for lithium-ion batteries. [PhD thesis, University of the Witwatersrand, Johannesburg]. WIReDSpace. https://hdl.handle.net/10539/48709

Downloaded from a DSpace repository. https://dspace.org/

Physico-chemistry of ceria-coated nickel-rich manganese cobalt oxides as cathode materials for lithium-ion batteries



UNIVERSITY OF THE
WITWATERSRAND,
JOHANNESBURG

Itumeleng Seotsanyana-Mokhosi

A thesis submitted to the faculty of Science at the University of Witwatersrand Johannesburg, in the fulfilment for the degree of

Doctor of Philosophy in Chemistry

Supervisor: Prof. Kenneth I. Ozoemena

December 2024

DECLARATION

I declare that this thesis is my own, unaided work. It is being submitted for the degree of Doctor of Philosophy in the University of the Witwatersrand, Johannesburg. It has not been submitted before for any degree or examination in any other university.

SIGNATURE:  DATE: 17th December 2025

DEDICATION

To my grandchildren Thabi, Thati and a sieo…

Be resilient in all you do, persevere and trust God

ACKNOWLEDGEMENTS

I could not have done this work alone. Many people helped me in many ways, and I would like to thank them and mention a few by name.

I pass my gratitude to my supervisor, Prof Kenneth Ozoemena. It was not easy, but you led from the front, you guided, you encouraged and supported immensely with knowledge and care.

I also thank the MEET group and CATMAT for robust insightful discussions and fun we shared. Some of you called, threatened, and cajoled when the ship was sinking. You were there when I needed you the most. A special mention goes to Dr Haruna for all the assistance he rendered.

I would also like to thank my family, my mum, my dear children, grandchildren, and my siblings (‘Masibilisi). There was COVID, we lost a sister, we were broken but you all picked me up and encouraged me to complete. You believed in me even when I had lost hope in myself.

To my dearest friends too many to mention by name, thank you for the support and the love and for keeping it real.

I would also like to thank Indabuko Institute for the financial support.

Finally, but most importantly, I thank God for everything.

PUBLICATIONS

Manuscripts for publication

1. **Itumeleng Seotsanyana-Mokhosi**, Kenneth I. Ozoemena, ““Enhancing the electrochemical performance of Nickel-Rich layered cathode material (NMC622) for Lithium-ion batteries by ultrathin conductive Ceria-surface coating.
   2024 European Journal of Inorganic Chemistry.(submitted)

2. **Itumeleng Seotsanyana-Mokhosi**, Kenneth I. Ozoemena, “Interrogating the effects of microwave-assisted surface-coating and doping with a little amount of CeO_2 on the electrochemical performance of $LiNi_{0.8}Mn_{0.1}Co_{0.1}O_2$ (NMC811)”, *Electrochimica Acta* 2024 (under review for submission)

CONFERENCES

1. Itumeleng Mokhosi , Kenneth Ozoemena Synthesis of fluorine and Ceria-dopes lithium manganese oxide spinel cathode Material for lithium-ion batteries. 70th Annual meeting of the ISE 2019
2. Seotsanyana Mokhosi, A. Haruna, K. O. Ozoemena *Effects of microwave irradiation on the physico-chemistry of lithium manganese oxide spinel cathode material Electrochemical Performance*. Pre satellite ISE meeting - “Energy Storage and Industry 4.0: Challenges and Prospects”. South Africa, 2019
3. Itumeleng Seotsanyana Mokhosi, K. I. Ozoemena *Manganese based Cathode materials for Lithium-ion batteries*. Indabuko Institute, CSIR South Africa 2019.

PROFESSIONAL ORGANIZATIONS

1. Chemical Society of Lesotho

2. Lesotho Maths and Science Teachers Association

ABSTRACT

The layered cathode materials, $LiNi_{0.6}Mn_{0.2}Co_{0.2}O_2$ (NMC622) and $LiNi_{0.8}Mn_{0.1}Co_{0.1}O_2$ (NMC811) have been lauded as robust and fitting candidates for the development of the next generation lithium-ion batteries for electric vehicles and other high energy demanding technological applications because of their high-energy density. Ni is responsible for the high-capacity/energy density, Mn contributes to structural and thermal stability, while Co contributes to the rate capability by mitigating the Ni/Li-ion mixing. It is therefore not surprising that the widespread commercialisation of NMC622 and NMC811 cathode materials have been frustrated by structural and thermal instability, capacity decay, and poor rate capability.

To overcome the poor electrochemical performance of the NMC622 and NMC811, this thesis investigated the use of ceria (CeO_2, a rare earth metal oxide) to coat or/and dope these two cathode materials. First, commercially available NMC622 was chemically modified with a very low amount of CeO_2 (~ 2%) to form an ultrathin CeO_2-coated NMC622 surface (NMC622-c). The NMC622-c exhibited enhanced electrochemical performance compared to the pristine counterpart (NMC622) in terms of i) the first cycle Coulombic efficiency was reduced by ~58% compared to the NMC622, and ii) capacity retention of 98 % after 50 cycles at 1C rate compared to the 82 % of the NMC622-c. This enhancement has been made possible by the NMC622-c

overcoming the destructive H2/H3 phase transition, reduced Ni/Li mixing, and improved ordered hexagonal structure. The results show that the electrochemical performance of the conventional commercial NMC622 cathode material can be significantly improved by optimising the CeO_2-surface coating.

Next, NMC811 (which is more energetic than the NMC622) was synthesized using the Taylor-Laminar flow method combined with microwave-assisted surface-coating and bulk-doping with about 2% CeO_2. Six samples were investigated, which are the pristine and microwaved samples (NMC811-p and NMC811-p_MW), CeO_2-coated and microwaved samples (NMC811-c and NMC811-c_MW), and CeO_2-doped and microwaved samples (NMC811-d and NMC811-d_MW). The NMC811-d and NMC811-d-mw outperformed other samples investigated in terms of the first cycle Coulombic efficiency and capacity retention. For example, NMC811-d_MW delivered a capacity of 220 $mAhg^{-1}$ with a capacity retention of 90 % over 50 cycles followed by the non-microwaved NMC811-d. The CeO_2 coating/doping eliminated the H2/H3 phase transition, which is known to lead to microcracks that propagate the degradation process. In summary, CeO_2 treatment offers alternative treatments that can be used to overcome degradation problems that are inherent in Ni-rich cathodes for Li-ion batteries, which can pave way to applications in electric vehicles and related high-energy demanding applications.

TABLE OF CONTENTS

DECLARATION ii

DEDICATION iii

ACKNOWLEDGEMENTS iv

PUBLICATIONS v

CONFERENCES vi

PROFESSIONAL ORGANIZATIONS vii

ABSTRACT viii

TABLE OF CONTENTS x

LIST OF FIGURES xiii

LIST OF TABLES xv

LIST OF SYMBOLS xvi

LIST OF ABBREVIATIONS xvii

Chapter 1 1

Introduction 1

1. Introduction **1**

1.1. Motivation 1

1.1.1. Population growth 1

1.1.2. Growth in technology 2

1.1.3. Environmental pollution 4

1.2. Renewable and sustainable energy sources 6

1.2.1. Energy storage and energy conversion devices 7

1.2.1.1. Supercapacitors 8

1.2.1.2. Fuel cells 9

1.2.2. Batteries 9

1.3. Aims and Objectives 10

1.3.1. Aim 10

1.3.2. Objectives 11

REFERENCES **12**

Chapter 2 14

Literature review 14

2. History of lithium-ion batteries **14**

2.1. Batteries 14

2.2. Cathode materials 24

2.2.1. Layered transition metal oxides. 31

2.2.2. NMC Cathode material 34

2.4. General synthetic routes for nickel manganese cobalt oxide 39

2.4.1. Sol-gel, solid state, freeze-drying and self-combustion methods. 39
2.4.2. Coprecipitation Method 40
2.4.3. Conventional mixing 41
2.4.4. Laminar mixing 42
2.5. Challenges of NMC cathode material 43
2.5.1. Residual lithium compounds 44
2.1.1. Phase transitions and capacity fading 47
2.5.3. Structural instability 51
2.6. Approaches to suppress the limitations of NMC 53
2.6.1. Washing 53
2.6.2. Physical barriers 55
2.6.3. Doping 55
2.6.4. Surface coating 57
2.7. Characterization techniques of NMC cathode materials 59
2.7.1. Physical techniques 59
2.7.1.1. Crystal lattice and morphology 59
2.7.1.2. Morphology 63
2.7.1.3. Chemical analysis 64
2.7.2. Theoretical background of electrochemical techniques 65
2.7.2.1. Cyclic voltammetry 65
2.7.2.2. Charge discharge technique. 73
2.7.2.3. Electrochemical impedance spectroscopy studies 76
2.8. Aim of the thesis 81

REFERENCES 82

Chapter 3 94

Experimental 94

3. Experimental 94
3.1. Reagents and characterizations 94
3.1.3. Electrochemical measurement 95
3.2. Synthesis of compounds 96
3.2.1. Preparation of NMC811 97
3.2.2. Preparation of coated NMC 99

REFERENCES 102

Chapter 4 103

Enhancing the electrochemical performance of $LiNi_{0.6}Mn_{0.2}Co_{0.2}O_2$ (NMC NMC622) by ultrathin conductive CeO_2 surface coating

..... 103

4. Introduction 103
4.1. Introduction to $LiMn_{0.6}Ni_{0.2}Co_{0.2}O_2$ 103
4.2. Experimental 106
4.2.1. Instrumentation 106
4.2.2. Electrochemical measurement 107
4.2.3. Preparation of CeO_2 coated NMC622. 108
4.3. Results and discussion 109
4.3.1. XRD 109

4.3.2. Raman spectra 112
4.3.3. SEM and TEM 113
4.3.4. Mapping 115
4.4. Electrochemical measurements 117
4.4.1. Cyclic Voltammetry 117
4.4.2. Galvanostatic charge-discharge. 120
4.4.3. Electrochemical Impedance Spectroscopy (EIS) 123
4.5. Conclusion 126
REFERENCES 127
Chapter 5 129
The effects of microwave-assisted surface-coating and doping with a little amount of CeO_2 on the electrochemical performance of $LiNi_{0.8}Mn_{0.1}Co_{0.1}O_2$ (NMC811) 129
5. Introduction 129
5.1. Introduction to $LiMn_{0.8}Ni_{0.1}Co_{0.1}O_2$ 129
5.2. Experimental 131
5.2.1. Characterization of the materials 134
5.2.2. Electrochemical measurement 134
5.3. Results and discussion 135
5.3.1. XRD 135
5.3.2. Scanning electron microscopy (SEM) 138
5.3.3. Transmission electron microscopy (TEM) 141
5.3.4. Thermogravimetric analysis 144
5.4. Electrochemical studies 146
CHAPTER 6 154
Conclusions 154
6. Conclusions 154
6.1. General Conclusion 154
6.1.1. $LiNi_{0.6}Mn_{0.2}Co_{0.2}O_2/CeO_2$ Electrocatalysts for High performance Lithium- ion batteries 155
6.1.2. $LiNi_{0.8}Mn_{0.1}Co_{0.1}O_2/CeO_2$ Electrocatalysts for High performance Lithium- ion batteries 155
6.2. Future work 156

LIST OF FIGURES

Figure 1-1 Graph of the outlook of world's energy consumption over fifty years. 2
Figure 1-2 The accelerating growth in technology over time (adapted from Micheal Lee, SA Museum) 3
Figure 1-3 A comparison of different EESS technologies in terms of specific power and specific energy. 7
Figure 2-1 Schematic representation of a Li-ion battery showing movement of Li^+ ions and electrons during charging and Li^+ ions during discharging. 16
Figure 2-2 A plot of gravimetric energy density vs volumetric energy density for different batteries. 18
Figure 2-3 The relative energy bands of different ions redox systems vs Li/Li^+ anion. 22
Figure 2-4 Binding energy of Li intercalated in several compounds, (b) some selected voltage profiles vs Li metal. 24
Figure 2-5 Different classes of oxide cathodes materials (a) the layered ($LiCoO_2$), (b) spinel, (c) olivine and (d) tavorite. 25
Figure 2-6 Schematic representation of the splitting of the Mn 3d orbital in Mn^{3+} (d^4**)** 29
Figure 2-7 Depiction of a layered structure of NMC charge delocalization occurs with minimum energy. 32
Figure 2-8 Change of qualitative energy diagrams of Li_xCoO_2 as a function of lithium the content. 33
Figure 2-9 Illustration of Conventional stirred reactor and laminar flow reactor 42
Figure 2-10 A cross section of a typical Laminar Continuous Taylor Reactor……..……..…43

Figure 2- 11 Change of qualitative energy diagrams of NMC showing relative Fermi level of the $Ni^{4+/3+}$ and $Co^{4+/3+}$ redox couples as a function of lithium content during charging (a) x = 1, (b) x= 0.5 (c0 x = 0) 48
Figure 2- 12 Phase transition and simultaneous gas evolution pattern for (a) NCA showing (i) crystal structure models for rhombohedral(layered), spinel, and rock-salt structures. (ii) TR-XRD patterns and simultaneously measured mass spectra (MS) profiles for(iii)O_2 and (iv) CO_2 released (b) MS profile for several samples of NMC for the release of O_2 together with measured phase transition measured with TR-XRD. 50
Figure 2-13 Summary of degradation mechanisms of Ni-rich NMC 52
Figure 2-14 Graphical representation of doping. 56
Figure 2-15 A typical cyclic voltammogram 66
Figure 2-16 Cyclic voltammograms of a reversible, a quasi-reversible and an irreversible electron transfer system. 68
Figure 2-17 . Factors affecting shape of voltammograms of LIBs. (a) nanoparticles, (a') nanosheets and scan rate, (b) scan rate and electrode thickness and (c) electrolyte concentration. 71
Figure 2-18 77
Figure 3-1 Schematic of a coin cell assembly for half cells. 96
Figure 3-2 Schematic of the synthesis of NMC811-p and NMC811-p_MW……..…….....98

Figure 3-3 Schematic of the synthesis of NMC811-d and NMC811-d_MW……...99
Figure 3-4 Schematic of the synthesis of NMC811-c and NMC811-c_MW……...100
Figure 3-5 Schematic of the synthesis of NMC811-c ..……..101
Figure 4-1 XRD patterns of A, NMC622, and B, CeO2-coated NMC622 and the insert shows the expanded area between 27-32 °. 110
Figure 4-2 Raman spectra of (a) NMC622-c and NMC622 (b) peak assignment.. ……112
Figure 4-3 SEM images of (a) NMC622 and (b) NMC622-c and EDS of (c) NMC622 and (d) NMC622-c..……..……...114
Figure 4-4 EDS mapping of (a) Ni, Mn, Co, C and O for NMC622 and (b) Ni, Mn, Co, Ce, C and O for NMC622-c…….……116
Figure 4-5 TEM images of (a) NMC622 and (b) NMC622-c ..…..…… 116
Figure 4-6 Comparative cyclic voltammograms of NMC622 and NMC622-c at 0.1mVs$^{-1.}$ ……118
Figure 4-7 Comparison of discharge capacities of pristine NMC and CeO_2 coated NMC622 at different C rates……..……121
Figure 4-8 Charge-discharge profiles and cycle performance with CE plots for (a),(b) NMC622 and (c), (d) NMC622-c over 50 cycles……..……..…....122
Figure 4-9 Comparative Nyquist plots of cells of (a) NMC622 and NMC622-c and (b, c)Equivalent electrical circuits used to fit NMC622 and NMC622-c, respectively……..……..……...124
Figure 5-1 XRD pattern of the prepared NMC811 powder materials and the corresponding partial enlargement of peaks (i)(003) and (ii)(108) and (110) ……136
Figure 5-2 Comparison of SEM images of : a) NMC-p, b) NMC-p_MW, c) NMC-d and d) NMC-c_MW e) NMC-c_MW and (f) NMC-d_MW……139
Figure 5-3 Typical EDS mapping of Ni, MN, Co, O and Ce for (a)Ce modified and (b) CeO2 coated NMC 811 …… 140
Figure 5-4 TEM images at low magnification of(a) NMC-c and (b)NMC-d at high magnification. ……141
Figure 5-5 Raman spectra of NMC-d_MW with its deconvoluted components and the overlain spectra of the NMC811 powders……..…..…..143
Figure 5-6 TGA of (a) 811-d_MW, (b)811-d, (c) 811-c, (e)811-p_MW and (f) 811-p and their corresponding mass signals curves in solid lines for 10K/min temperature ramp and 25-900 ^{0}C. 145
Figure 5-7 CV curves for (a) NMC811-p, (b) NMC811-p_MW, (c) NMC811-c, (d) NMC811-c_MW, (e) NMC811-d and (f) NMC811-d_MW, 147
Figure 5-8 Comparative Charge-discharge voltage profiles showing 1st, 2nd, 5th, 10th, 20, 30th 40th and 50th cycle at 0.1C rate for: (a) NMC811-p, (b)NMC811-p-MW, (c) NMC811-cv, (d) NMC811-c-MW, (e) NMC811-d, and (f) NMCV811-d-MW……..……149
Figure 5-9 Capacity retention and coulombic efficiency for (a) NMC811-p, (b) NMC811-p_MW, (c) NMC811-c, (d) NMC811-c_MW, (e) NMC811-d and (f) NMC811-d_MW……151
Figure 5-10 Rate performance of samples of NMC811 at 0.1C,0.2C, 0.5C. 1C……152

LIST OF TABLES

Table 2-1 A comparison of battery types in cost. 19
Table 2-2 Characteristics of some commercial battery electrode materials 36
Table 2-3 Comparison of the characteristics of Mn, Co, and Ni in MNC cathodes. 37
Table 2-4- Physicochemical and electrochemical properties of various NMC cathode formulations. 38
Table 4.1 Cation mixing parameters and lattice parameters of NMC622 and NMC622-c……...111
Table 4-2. EDX data for NMC622-c……...114
Table 4-3 CV peak potentials for NMC622 and NMC622-c and for the dominant peak……118
Table 4-4 Summary of cyclability studies for NMC622 and NMC622-c …….… 123
Table 4-5 Parameters from fitting EIS Nyquist's plots using the equivalent circuits. 125
Table 5-1 Intensity ratios, I(003) / I(104) and (I(006) / I(102))/ I(101) for the different cation materials……..…… 137
Table 5-2 The summary CV potentials for the NMC811 samples……... 149
Table 5-3 Initial and maximum discharge capacities of the NMC powders. 151
Table 5-4 Capacity retentions of the NMC811 powders. .152

LIST OF SYMBOLS

° - Degree

< - Less than

≤ - Less than or equal to

> - Greater than

~ - Approximately

Θ - Theta

Al - Aluminium

Ar - Argon

Co - Cobalt

Cu - Copper

F - Oxygen

Mn - Manganese

Mg - Magnesium

Ni - Nickel

O – Oxygen

LIST OF ABBREVIATIONS

CE :	coulombic efficiency
CEI:	Cathode electrode interphase
COP26:	UN climate Change Conference 2021
CV:	Cyclic voltammetry
DEC:	Diethylene carbonate
DMC:	Dimethyl carbonate
EC:	Ethylene carbonate
EESS:	Electric energy storage systems
EV:	Electric vehicle
G-CD:	Galvanostatic charge-discharge
GEIS:	Galvanostatic electrochemical impedance spectroscopy
ICE:	Internal combustion engines
LCO:	Lithium cobalt oxide
LCTR :	Laminar continuous Taylor reactor
LIB:	Lithium-ion battery
LIBOB:	Lithium bis(oxalate) borate
LMO:	Lithium manganese oxide
NCA:	Lithium nickel aluminium oxide
NMC:	Lithium nickel manganese cobalt oxide
NMP:	N-methyl pyrroline
PEIS:	Potentiostatic electrochemical impedance spectroscopy

PHEV:	Plug-in hybrid electric vehicle
PVA:	Polyvinyl alcohol
PVDF:	Polyvinylidone fluoride
SC:	supercapacitors
SEI:	Solid electrolyte interphase
Toe:	Tons of oil equivalent
TW	Terra Watts
UN:	United Nations
Vs:	Vs
V:	Voltage
dQ/dV	Differential capacity

Chapter 1

Introduction

1. Introduction

1.1. Motivation

The rapid growth in the world's population has encouraged development of new technologies including, the people's connectivity through cellular phones, smart tablets, laptops and drones. With these general technological advancements in many areas of our lives, mobility has also increased, leading to an increase in the demand of energy globally.

1.1.1. Population growth

The global human population has grown from 1 billion since 1800 to an estimated 7.7 billion currently and it continues to grow at between 1.1-2.2% annually. It is expected to rise to ~10.1 billion by 2100.[1] Inherently, as the human population increases, so does the demand for energy to perform everyday life activities. According to the United States Energy Information Administration, the energy demand has trebled over a period of fifty years.[2,3,4] Most of the energy is currently sourced from fossil fuels as shown in, Figure 1-1. It is predicted that the current annual energy production of 14 TW will have to be doubled by 2050 to cope with the current trend in demand.[5,6,7] This translates to a colossal amount of natural gas and oil that would need to be extracted on a year-to-year basis.

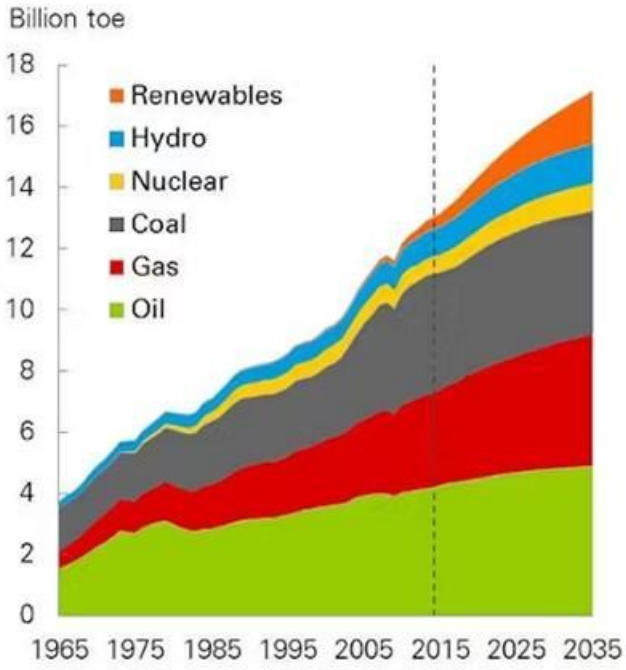


Figure 1-1 Graph of the outlook of world's energy consumption over fifty years.[4]

1.1.2. Growth in technology

Technology growth has also shown accelerated growth in recent times as seen by the representation in Figure 1-2. Urbanisation, advancements in information technology, accelerated connectivity and movement of the ever-increasing population are some of the markers of improved technological adaptations in our lives. Growth in technology is always fuelled and supported by access to resources and raw minerals which can only be available through adjustments in energy supply.

Thus, as technological growth accelerates, so does demand for energy. If there was ever any doubt about this relationship, the pattern seen during

the COVID-19 pandemic proved this beyond doubt. Spatial and temporal energy demand patterns changed a lot during the time of lockdowns.[8] Commercial and industrial demand declined while residential and medical energy supply increased, but because the former two always account for larger amounts of energy than the latter, there was an overall drop in energy consumption. During the peak of the pandemic, economic and travel restrictions and lockdowns were implemented globally and they coincided with a big drop in energy demand. Data collected for July 2020 showed a weekly drop in energy demand of between ~9% to ~24%, which varied based on the degree of restrictions observed. In India, there was first a drop in electricity demand followed by an increase due to a higher demand in industrial sectors and increased irrigation.[9]

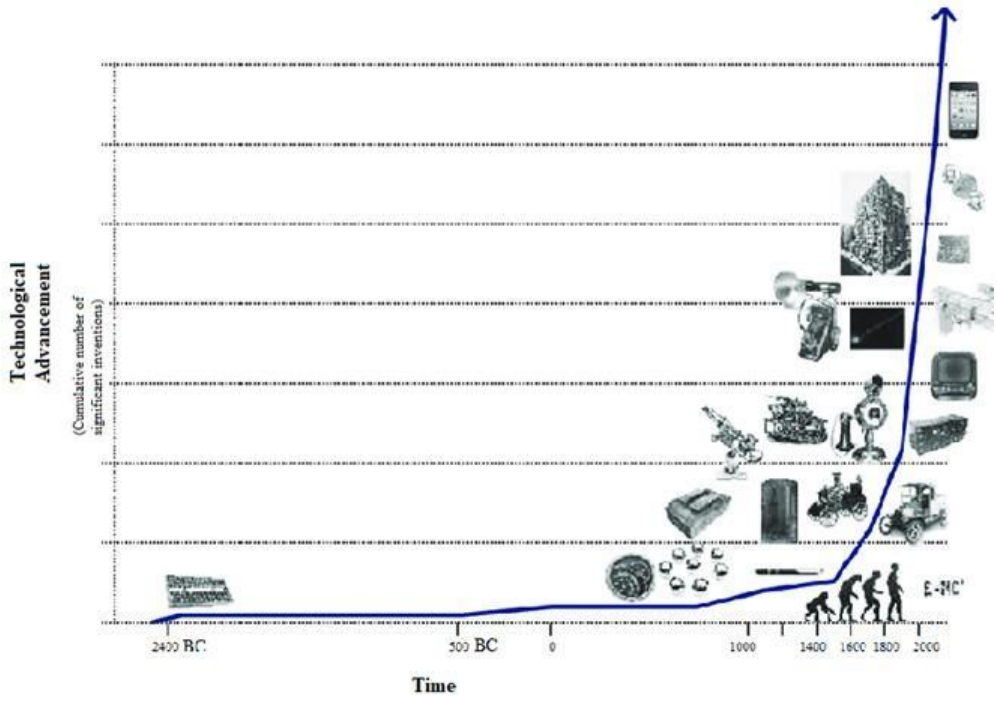


Figure 1-2. The accelerating growth in technology over time (adapted from Micheal Lee, SA Museum)

This proved how human activities are central to energy demand statistics. Furthermore, the travel restrictions and non-essential activities due to COVID-19 resulted in a marked improvement in waterways and air quality in most regions.[8, 10]

1.1.3. Environmental pollution

Access to and use of energy are almost always related to environmental distress. Air pollution, water pollution, climate change and solid waste pollution are some of the environmental problems that can be directly related to energy production. Oil spillages, emission of gases into the atmosphere and changes in water quality from mining and acid rain are just a few of the possible environmental ills.

The global energy outlook shown in Figure 1-1, reveals that most of the energy the world consumes originates from fossil fuels. Since fossil fuels' supply is not endless and they emit greenhouse gases when they burn, they are considered non-renewable sources that may lead to catastrophic environmental disasters. The latter can lead to climate change resulting in global warming and other natural disasters like flooding and other extreme weather conditions. China has already shut down some of its polluting industries. Recently, in 2022, Germany has declared that it will go 100% off fossil fuels by 2035. However, these moves are not enough, more countries must transition towards renewable energy.

The source of energy plays a crucial part in the carbon footprint. Fossil fuels used in transportation have a big carbon footprint. It is therefore desirable for the world to become less reliant on fossil fuels in many areas including in transportation. Efforts to curb the problem of pollution have resulted in policies that propose a ban on or drastic reduction in the production and use of internal combustion engines (ICE). Some Western and Eastern countries, including France (2040) and the UK (2040),[11] The Netherlands (2025), Norway (2025) and India (2030) are signatories to such conventions. The result of this is an increase in electric vehicles (EV) and plug-in electric vehicles (PHEV). However, this drive still needs a way of storing energy and thus, batteries and other energy conversion devices are needed.

South Africa produces 80% of its energy from coal and the country is ranked 15th globally in terms of countries with highest CO_2 emissions. South Africa is therefore under pressure to reduce its carbon emission by 80% by 2030. The country has agreed to phase down unabated coal and inefficient fuel subsidies as written in the 2021 Glasgow Climate Pact together with other members of the UN. At the COP26 meeting, the world leaders discussed ways of funding efforts to reduce carbon emissions by pledging some money towards coal and fossil-fuel replacement. This led to a commitment by South Africa's government to an investment package of $8.5 billion to accelerate the phasing out of coal and move to greener energy with France, Germany, the UK, the EU, and the USA as donor countries.

South Africa is well endowed with some of the metals that are known to form the backbone of the battery industry such as manganese and nickel. It has the world's highest reserves of manganese, and its annual production of 49000 tonnes of nickel places it amongst the top ten with a reserve estimated at 408.5 million tonnes.[12,13] Also, South Africa has access to nearly 3000 km of coastline, which potentially means it can develop to extract lithium from brine and even expand to recover some from recycled materials. There also exists an economic need to create jobs and encourage beneficiation and smelting of metals in South Africa for better profits. Thus, research on Lithium-ion batteries (LIB) also directs these economic efforts in the right direction to increase the chain value of some of the minerals mined here in South Africa.

1.2. Renewable and sustainable energy sources

The world is thus looking to increase the contribution of sustainable, cleaner, cheaper, and reliable renewable energy sources. Tidal, solar and wind are some of the leading renewable energy sources; these energy sources are typically converted into electricity. Renewable energy sources are inherently localised and intermittent. Nonetheless, it has been predicted that in the next two decades, renewable energy will make up 40% of the world's energy supply.[4] This can only be achieved by employing energy storage and conversion devices. It is therefore not surprising that sustainable and renewable energy supply, global warming and energy conversion and storage are such hot research topics.

1.2.1. Energy storage and energy conversion devices

An imperative factor in bridging and increasing the contribution of renewable energy sources is the balance between electricity generation, distribution, and consumption. Enablers in this energy conundrum would be the designs of better electrical energy storage and energy conversion systems (EESS) devices. Just about 1% of the energy consumed globally is stored, and most of it is done using pumped-storage hydroelectricity, which is only available in areas with the right terrain.[14] Electrochemical supercapacitors, batteries and fuel cells are the modern EESS technologies that have been marked as necessary to change the picture and help the world achieve a marked growth in sustainable clean energy adoption. A Ragone plot that compares these modern EESS is depicted in Figure 1-3.

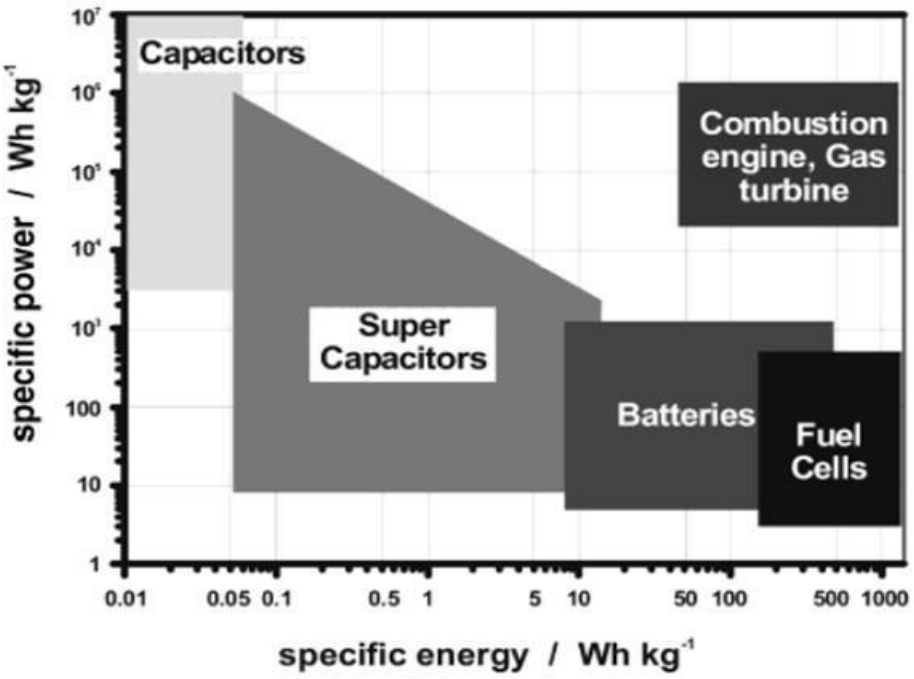


Figure 1-3 A comparison of different EESS technologies in terms of specific power and specific energy.[15]

While South Africa is transitioning to low-carbon fuels, it has also been hit by a series of electricity rations, load shedding and electricity reduction. Ageing infrastructure, poor quality coal, and the cost of running coal-powered generators are just some of the causes of the power instability in recent years. Consequently, consumers and even suppliers are looking for stable off-grid electricity with some opting to store energy during times when electricity is running while others go for alternative sources of energy such as solar energy. This has led to the rapid growth of an integrated plan where some energy generation is achieved through solar and wind in South Africa and other African states like Zimbabwe. These invariably translate to growth in the application of EESS devices.

1.2.1.1. Supercapacitors

Supercapacitors (SC) are electrochemical energy storage devices that store energy through the adsorption and desorption of ions on the interface between electrodes and electrolytes. They convert energy during charging and discharging through an electrochemical double-layer of two electrodes with large surface area capacitances. They are also referred to as ultracapacitors, double-layer capacitors or electrochemical capacitors. Because SCs operate through adsorption, electrodes offer high surface area and high electrical conductivity hence porous materials such as carbon, MnFe-O, NiO are often used. They are characterized by high power potential and rapid charge and discharge, poor self-discharge and general low cost. They charge or discharge in seconds and are good for bursts of

electricity. They are therefore applied in instances where rapid high power is needed rather than in cases where long-time gradual power is needed. They tend to use the dielectric charge between plates which operates through a build-up of charge between insulators by storing static electricity.

1.2.1.2. Fuel cells

Fuel cells are also electrochemical cells driven by the chemical energy stored within the fuel's bonds by converting it into electrical and heat energy. Hydrogen, metal hydrides, formic acid, some low-density hydrocarbons, and alcohols such as propane, ethanol and methanol are some of the fuels used. High efficiency, extremely high specific energy density, low amounts of pollution emissions and relatively low maintenance are the key distinguishing characteristics of fuel cells. They are more energy-dense than supercapacitors and some batteries. Fuel cells run on a constant supply of fuel which can require major infrastructure re-do for wide application. The fuel is highly flammable and poses the danger of fires. In some instances, fuel reformers are used to continuously supply the fuel. Currently specific energy costs for fuel cells are slightly high. This is because of the reluctance of communities to adopt the technology and invest in the infrastructure. Also, the catalysts used to bring about the redox processes are mainly expensive precious metals.

1.2.2. Batteries

Batteries are voltaic cells with one or more electrochemical cells which store and change chemical energy into electrical energy. The potential difference

between the electrodes is the key to driving the charge-discharge processes. Batteries come in different chemistries and technology, but they tend to have high specific density. Unlike fuel cells, once batteries are made, there is no need for a constant supply of any material for the battery to run. This work is focused on batteries which will be discussed at length in Chapter 2.

It is for the reasons mentioned earlier that low-cost, high-capacity batteries are sought after. Lithium-ion batteries (LIB) are a generation of batteries that can meet these requirements. Lithium-ion batteries have also been identified as prospects to power EVs and off-grid electrical energy storage systems. The first commercial LIB had $LiCoO_2$ cathode material, but now efforts to reduce Co and increase other transition metals are well underway and will be discussed in section 2.3. This work focuses on $Li(Ni_xMn_yCo_z)O_2$ (NMC) where (x+y+z=1) which has been coated with CeO_2 or doped with Ce. Although Ce is a rare element, it is the most abundant of the rare elements and very minute amounts of Ce are used when either coating or doping the cathode material.

1.3.Aims and Objectives

1.3.1. Aim

The focus of this study is to synthesize nickel-rich NMC cathode material for Li-ion batteries with improved electrochemical properties for higher performance.

1.3.2. Objectives

The objectives of this study are to:

1. synthesize CeO_2-coated NMC622.
2. investigate the effect of synthesizing NMC811, CeO_2-coated NMC811 and Ce- doped NMC811 using the conventional lab method and a laminar flow reactor.
3. subject some of the synthesized materials to microwave irradiation.
4. investigate the physico-chemical characterization of the synthesized materials using PXRD, Raman, TGA, BET, SEM, TEM, and HRTEM.
5. Fabricate coin cells using the material and apply the samples of Ni-rich NMC synthesized as cathode material and investigate their electrochemical performance using coin-type Li-ion cells.

REFERENCES

1. https://www.un.org/development/desa/en/news/population/world-population-prospects-2019.html

2 Li, M., 2017. World energy 2017–2050: annual report. *Department of Economics, University of Utah*.

3 Arias, L.A., Rivas, E., Santamaria, F. and Hernandez, V., 2018. A review and analysis of trends related to demand response. *Energies*, *11*(7), p.1617.

4 International Energy Agency Key World Energy Statistics 2011 (IEA, 2011); available at http://www.iea.org/publications/freepublications/publication/key_world_energy_stats-1.pdf.

5 https://www.ogj.com/ articles/2017/01/bp-energy-outlook-global-energy-demand-to-grow-30-to-2035.html

6 Siegel, E. Forbes. *How much does it take to fuel the world?* [Online] Forbes,. https://www.forbes.com/sites/startswithabang/2017/09/20/#609a223916d9.

7 Lewis, N.S., 2007. Powering the planet. *MRS bulletin*, *32*(10), pp.808-820.

8 Jiang, P., Van Fan, Y. and Klemeš, J.J., 2021. Impacts of COVID-19 on energy demand and consumption: Challenges, lessons and emerging opportunities. *Applied energy*, *285*, p.116441.

9 IEA. Covid-19 impact on electricity, International Energy Agency (IEA), Paris, France; 2020 <https://www.iea.org/reports/covid-19-impact-on-electricity> [accessed 26.10.2020].

10 Manoiu, V.M., Kubiak-Wójcicka, K., Craciun, A.I., Akman, Ç. and Akman, E., 2022. Water quality and water pollution in time of COVID-19: positive and negative repercussions. *Water*, *14*(7), p.1124.

11 Nathan, Stuart. The Engineer. *Electric revolution gathers pace with UK car policy announcement.* [Online] The Engineer, 26 July 2017. [Cited: 14 March 2018.] https://www.theengineer.co.uk/electric-revolution-gathers-pace-with-uk-car-policy-announcement/

12 Https//www.miningweekly.co/s-africa-to-remain-among-top-nickel-producers-2018-04-20

13 Evans, D.M., Hunt, J.P.P.M. and Simmonds, J.R., 2016. An overview of nickel mineralisation in Africa with emphasis on the Mesoproterozoic East African Nickel Belt (EANB). *Episodes*, *39*(2), pp.319-333.

14 Larcher, D. and Tarascon, J.M., 2015. Towards greener and more sustainable batteries for electrical energy storage. *Nature chemistry*, *7*(1), pp.19-29.

15 Kunze-Liebhäuser, J., Paschos, O., Pethaiah, S.S., Stimming, U. (2019). Fuel Cell Comparison to Alternate Technologies. In: Lipman, T., Weber, A. (eds) Fuel Cells and Hydrogen Production. Encyclopedia of Sustainability Science and Technology Series.

Springer, New York, NY. https://doi.org/10.1007/978-1-4939-7789-5_157

Chapter 2

Literature review

2. History of lithium-ion batteries

2.1. Batteries

A battery is a device that converts energy stored in chemicals to electric energy by undergoing an electrochemical reaction. There are two main types of batteries, the primary and the secondary batteries corresponding to non-rechargeable and rechargeable batteries, respectively. This work focuses on cathode material for LIBs rechargeable batteries.

Batteries come in different forms, sizes, and shapes and have different chemicals that store the energy with a history that spans over 273 years.[1] It was while experimenting with capacitors that Benjamin Franklin in 1749 formulated the term battery. The development of the first electrochemical battery was for a copper-zinc couple by Volta in 1800, followed by lead-acid by Planté in 1859 and a zinc-manganese-oxide dry cell in 1866. In1878 Leclanché developed a zinc-air battery which was followed by Jungner's in 1899 who worked on Ni-Cd and Ni-Fe batteries. Edison patented the latter in 1901. Sodium-sulphur batteries by Yao and Kummer followed in 1966 and Ni-MH batteries by Ovshinsky took off in 1962. Lithium was first used in lithium primary cells which were commercialised in the late 1960s. LiAl anodes were then used with TiS_2 cathodes in 1977-1979 by Exxon. Interestingly, the cathode was found to allow reversible intercalation of Li

ions over 1000 cycles in the TiS_2 compound and thus marked the advent of rechargeable batteries. The first Lithium-ion battery (LIB) prototype was developed by Yoshino in 1985 based on earlier research by Goodenough,[2] and Whittingham. This led to commercial LIB using $LiCoO_2$ cathode and carbon anode in 1992.[3,4]

The invention and impact of the LIBs on modern life were recently acknowledged and credited to John Goodenough, Stanley Whittingham, and Akira Yoshino by awarding them with the 2019 Nobel Prize in Chemistry. Other forms and chemistries of popular LIBs that followed were the Li-ion polymer and Li-ion nano phosphate in 1999 and 2001, respectively. The advent of new battery chemistry does not quash or replace old battery technologies instead, it either offers alternatives or augments them for improved or diversified application.

All batteries consist of two electrodes, anode and cathode, and an ionically conducting medium, the electrolyte, with a separator often employed to keep the anode from direct contact with the cathode to avoid direct chemical reaction. The electrodes have different reduction potentials so connecting them via an external circuit allows a spontaneous flow of electrons from the anode to the cathode while ions flow within the electrolyte to balance the charge difference created between electrodes. In essence, reduction takes place at the cathode and oxidation at the anode and the movement of electrons together with the accompanying redox reactions at the electrode continue until the reactants are used up for a primary cell. For a

rechargeable battery, this electrochemical reaction is reversible. A charger with a larger voltage restores the battery to its charged state by supplying electricity from an external source in the opposite direction. This means during discharge a battery's positive terminal is the cathode and the same electrode becomes the anode during charge.

1.1 Lithium-ion Batteries

Lithium-ion rechargeable batteries (LIBs) currently dominate in portable electronics, laptops, and mobile power tools. While a LIB is being charged, the anode material is reduced as it gains electrons as seen in Figure 2-1. This is then compensated by the migration of Li^+ ions from the cathode material through the electrolyte to balance the charge on the anode. Electrons move in the outer circuit generating an electric current. When the Li-ion battery discharges, the reverse occurs and Li^+ gets intercalated back into the cathode.

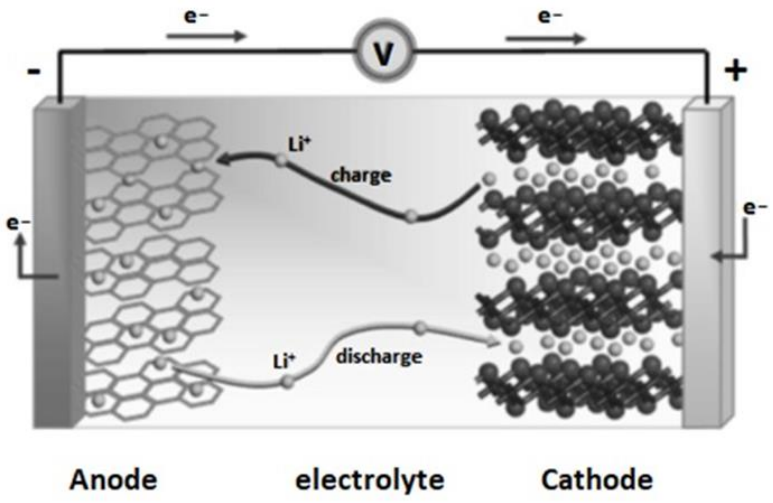


Figure 2-1 Schematic representation of a Li-ion battery showing movement of Li^+ ions and electrons during charging and Li^+ ions during discharging.

Examples of half-reactions that take place at the electrodes during the charging for $LiMO_2$ as cathode with M as a transition metal and carbon anode (C_6) are given in Equation 1 and Equation 2, and the overall reaction equation is given in Equation 3. During discharge, the reverse for each reaction occurs.

Negative electrode: $C_6 + x\,Li^+ + xe^- \xrightarrow{charge} Li_xC_6$ Equation 1

Positive electrode: $LiMO_2 \xrightarrow{charge} Li_{1-x}MO_2 + xLi^+ + xe^-$ Equation 2

Overall equation: $C_6 + LiMO_2 \xrightarrow{charge} Li_xC_6 + Li_{1-x}MO_2$ Equation 3

This means a single cathode electrode must allow the conduction of both lithium ions and electrons. Transition metals and some additives in a battery may exhibit poor conductivity, therefore carbon black is commonly included in the cathode fabrication to improve the conductivity. The carbon and the cathode material possess a powdery consistency; thus, they are often held together by a binder. During the rather sensitive and complex physical design, care is taken for the active materials, conductive carbon, and electrolyte to mix properly and thoroughly to achieve a homogenous mixture to minimise pockets of regions with different textures which can easily lead to added impedance regions within the same battery. Electrolytes are often salts of lithium such as $LiPF_6$ or LiBOB a boron oxalate coordinated compound dissolved in a combination of carbonate and ethers such as ethylene carbonate (EC), diethylene carbonate (DEC) or dimethyl carbonate (DMC) and solid electrolyte. Polymer electrolytes have also been used especially for flexible LIBs applications.[5] The electrolyte is an important essential conducting part of a battery because it affects the

performance in terms of energy density, fire and explosion safety, and leakage and stability.

Application of LIBs in portable devices stems from a combination of properties including long life span, relative environmental friendliness, and lightweight. LIBs can be produced in small sizes but with high energy density due to their high gravimetric and volumetric energy densities when compared with other conventional batteries as shown in Figure 2-2 and Table 1. Consequently, LIBs are deemed to be batteries with great potential for future-generation hybrid/full EVs and PHEVs. They have already been used in EVs for over a decade.[6]

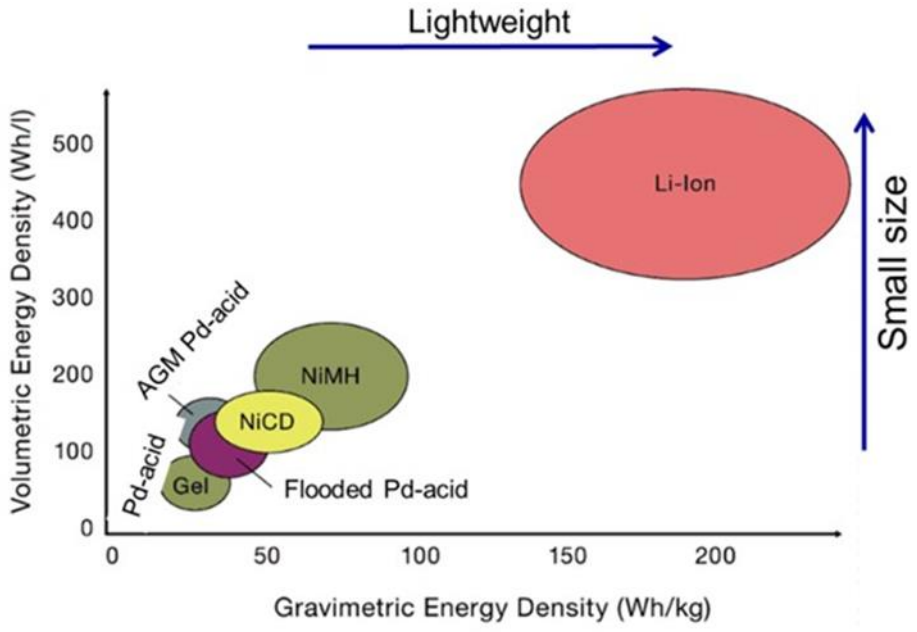


Figure 2-2 A plot of gravimetric energy density vs volumetric energy density for different batteries.[7]

Table 2-1 also shows how the cost per power offered by LIBs compared with other common batteries. Cathode material is the component of LIBs

that limits the energy density, and it accounts for more the 70% of the cost of a battery.[8]

Table 2-1 A comparison of battery types in cost. [8]

Type of battery	Cost per energy (US$/Wh)	Gravimetric energy density (Wh/kg)	Volumetric energy density (Wh/l)
Lead-Acid	0.17	20-50	40-140
Alkaline long life	0.19	110	320
Carbon-zinc	0.31	36	92
NiMH	0.99	95	150-300
NiCd	1.50	39-65	110-180
Lithium-ion	0.47	150-315	300-600

The desire to expand the use of LIBs for application in energy-intensive initiatives such as full plug-in and hybrid electric vehicles (EVs), grid storage applications and military applications has generated extensive research to find cathode material with improved aspects of safety, longer cycle life at elevated as well as low temperatures. [9-18]

In EVs the target is also to reach longer driving range on a single charge at a decent speed. Consequently, gravimetric energy density has more than doubled from 98 to 230 Wh kg^{-1} and the volumetric energy density has almost tripled to ~620 Wh L^{-1} since the inception of LIBs. However, gravimetric energy density is still below the 400 Wh kg^{-1} delivered by internal combustion engines on liquid fuels,[14, 15] hence the efforts to improve the LIBs continue. [19,20]

The low equivalent weight of LIBs is inherent to the nature of lithium which is the third lightest element with the lowest redox potential and smallest known ionic radii. Initially, lithium metal was used as the anode in rechargeable batteries. However , lithium metal is highly reactive and reacts with the electrolyte damaging other components of the battery. It also presented the dangers of explosions and fire hazards because of the development of metal dendrites during cycling.[16,21] The dendrites cause a battery to self-short circuit. The discovery and understanding of intercalation compounds offered a safer option of using lithium-ion batteries.

Intercalation chemistry describes the reversible incorporation of guest particles, which can be ions or molecules into the interstitial sites of the parent host. Generally, a Li-ion battery has at least one of the electrode materials as a structure that can reversibly accommodate lithium ions and allow lithium ions to shuttle between the electrodes during charge-discharge cycling. For cathodes in LIBs, lithium ions are the guest, and metal oxides, chalcogenides, or polyanions are the hosts. The guest moves about into and out of the host molecule, reversibly during charging and discharging. For a long and good cycle life of a battery, this “rocking chair” activity should not change the basic structure of the host compound.

Interest in intercalation compounds started when studies on solid-state chemistry revealed that the guest molecules could alter either the electronic, optical, or both properties of the host material. Even the conductivity of the

host material can change depending on the nature of the guest molecule or ion, for instance superconducting transition temperature could be enhanced by just the insertion of a guest molecule.[17,22] This can result in high free energy of the reaction,[18] a behaviour which was previously seen in electrochemical reactions when the guests was inserted into the host from the anode.[23] Using this background, Whittingham established the first rechargeable lithium battery system of Li ions intercalated between layered TiS_2 with a discharge voltage of less than 2.5 V, the Li ions originated from the lithium aluminium anode and proposed it as a possible energy storage electrode.[24]

Further studies of the system showed that it was one of the most gravimetrically favoured systems studied and it had all components in the same state, and good reversibility. It was not accompanied by structural changes when with or without lithium ions. This battery system has high gravimetric energy density and long cycle life and was made commercial by Exxon[25,26] This battery did not achieve much growth because of its low discharge voltage. [19-21]

Mizushima et al. did extensive work to try and replace the sulfides in Whittingham's battery to increase the cell voltage.[2] In LIBs, the voltage is determined by the chemical potential difference between lithium in the anode and lithium in the cathode. The cell voltage of a battery is a result of the energy difference between cathode and anode, Equation 4.

$$E_{cell} = E_{cathode} - E_{anode} \qquad \text{Equation 4}$$

In its elemental form, lithium has a different potential from Li in intercalation compounds. Figure 2-3 shows the energy diagram of different ions relative to Li/Li^+ energy state. The redox couple, Li/Li^+, is at the top, and at the bottom is O^{2-} with its highest occupied orbital being 2p. This gives oxides with Li the largest energy difference, and so the largest voltage. On the other hand, the S^{2-}:3p orbital band becomes the limiting energy band because it lies above the energy band of the upper oxidation states for the metals and would thus be more favoured energetically over the metal's orbitals for pairing up with Li.

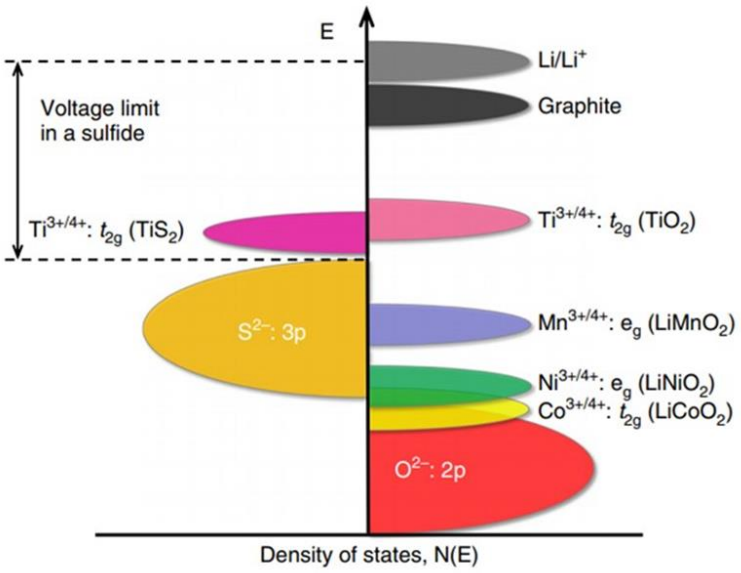


Figure 2-3 The relative energy bands of different ions redox systems vs Li/Li^+ anion.[23]

The highest occupied orbital of oxygen overlaps with the low-lying metal orbitals and makes the metal orbitals accessible for redox activity while

enjoying the stabilisation by the highest-lying oxygen orbitals. The voltage achieved was approximately 4 V and 2.5 V for compounds of metal with oxygen and metal with sulphur, respectively.

The potential of a battery is also a function of the amount of Li available in the intercalated compound and the cell voltage. The potential of Li as a metal differs from the potential of lithium in intercalated compounds and can be represented using Equation 5 where $\mu_{Li^{\circ}}$ is the chemical potential of Li metal and $\mu_{Li^{int}}$ is the potential in the intercalation compound.[24 29] The amount of Li available within a compound is indicated by x.

$$V(x) = -(\frac{1}{e)}\left(\mu_{Li^{int}}(x) - \mu_{Li^{\circ}}\right) \qquad \text{Equation 5}$$

The potential of Li in the intercalated compound is also determined by the cell energy as a product of the binding energy as shown in Equation 6. In Li-ion batteries, the binding energy is high for cathodes and low for anodes. [13-14]

$$-\mu_{Li^{int}}(x) = \ Lithium\ Binding\ Energy \qquad \text{Equation 6}$$

Figure 2-4 shows the binding energies of lithium in various intercalation compounds and LiF as a reference measured against lithium metal. Both cell voltage and the amount of Li ions available and transferable during cycling determine the overall energy density.

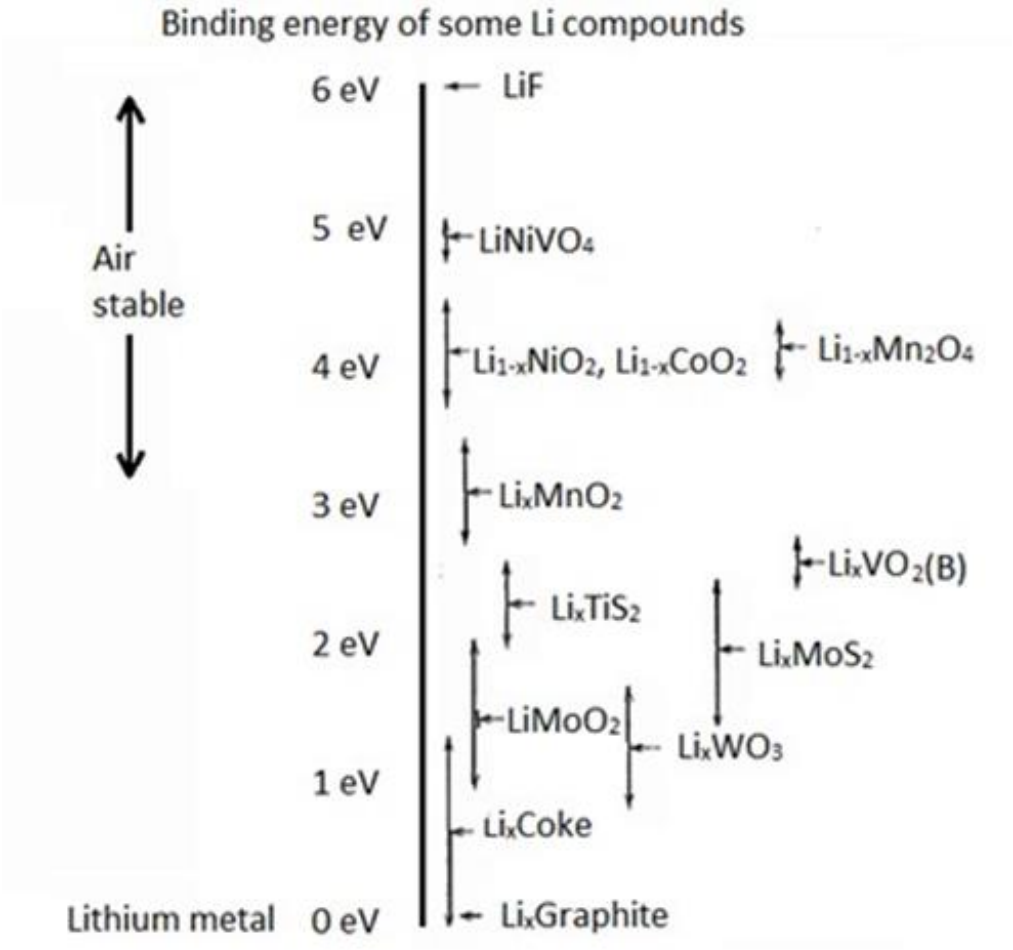


Figure 2-4 Binding energy of Li intercalated in several compounds, some selected voltage profiles vs Li metal. [25,]

2.2.Cathode materials

Another interesting work was efforts to replace the semi-metal titanium in the first studied rechargeable battery system with electroactive transition metals as central ions of the host material. This work yielded many of the present-day cathode materials. The pinnacle of success of that effort was designing the first successful commercial layered $LiCoO_2$ (LCO) cathode.[2] The cathode materials include two-dimensional layered compounds with a general formula $LiMO_2$ where M can be Co, Ni such as $LiCoO_2$, and three-

dimensional spinels with a general formula LiM_2O_4 with M = Mn, Mn_xNi_y like $LiMn_2O_4$ and one dimensional polyanions olivines, with the formula $LiMXO_4$, and tavorites like $liFePO_4$ and $LiFeSO_4F$, respectively. [26-31] Figure 2-5 shows some of the crystal structures of metal oxide cathode materials that have been discovered.

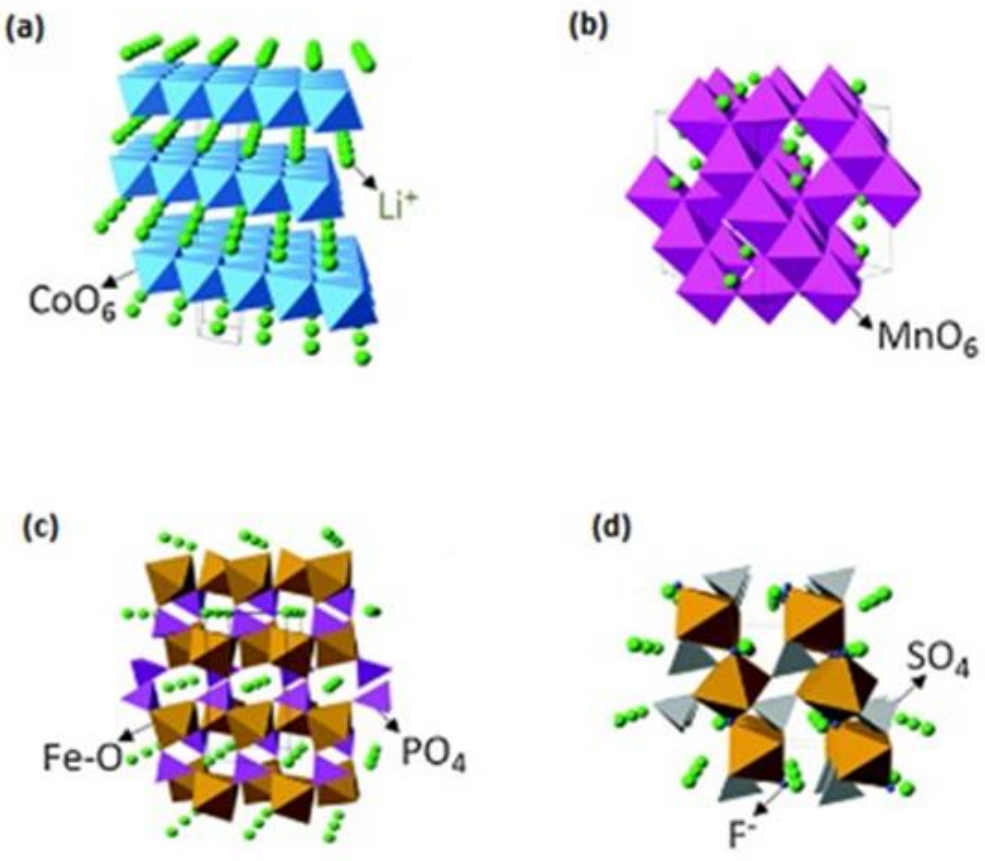


Figure 2-5 Different classes of oxide cathodes materials (a) the layered ($LiCoO_2$), (b) spinel, (c) olivine and (d) tavorite.[6]

The general requirements for a material to be used as a successful cathode material are as follows.

(i) The material must easily undergo redox reactions such as transition metals which have many oxidation states.

(ii) React reversibly and rapidly with lithium with a stable structure that does not change in the presence of Li for a high-power density.

(iii) Must have high free energy of the reaction to have high voltage, capacity, and energy storage.

(iv) Possession of good electronic conductivity which reduces the need for additives such as carbon to yield overall high energy density.

(v) It must be environmentally benign and low in cost.

Manganese was used because it is abundant, it has low cost, and it is environmentally benign. Lithium manganese oxide formulations, such as $LiMn_2O_4$ (LMO) which was discovered in 1983 was found to be favourable and was consequently commercialised by Moli Energy in 1996.

The manganese spinel, LMO, presents as a close-packed array of oxide ions forming a compound with an *Fd3m* space group. The three-dimensional spinel framework has the transition-metal cations ordered in all the layers. This creates a situation where Li^+ and $Mn^{3+/4+}$ are located at 8a tetrahedral sites and 16d octahedral sites, respectively. Lithium ions are thus able to easily diffuse through the vacant interstitial 16c octahedral sites while the electrons move through the Mn-Mn interactions on the octahedral edges. The polarity acquired from the different oxidation states of the Mn makes electronic movement easy. The lower internal resistance and

improved electronic and Li^+ ion conductivity of LMO. It allowed LMO the ability to undergo easier and faster charge cycling. Other attributes of LMO are good thermal stability, high operating voltage and power. Its capacity of less than 130 $mAhg^{-1}$ is less than that of LCO. However, the most documented limitations of LMO are poor cycle life and fast capacity decay. Capacity fading is caused by:

1. electrode degradation including Mn dissolution, [4,6,26,]and irreversible side reactions of the electrolyte,[31,32]
2. Jahn-Teller effects which can be due to the distortion or the collapse of the parent geometry of the host compound, [6,27-30]
3. oxygen and lithium deficiency. [32,33]

The electrochemistry of LMO is centred around the reversible $Mn^{3+/4+}$ redox pair during charging and discharging, Equation 7.

$$Mn^{3+} \rightleftharpoons Mn^{4+} + e^- \qquad \text{Equation 7}$$

However, disproportionation of the trivalent Mn also occurs where Mn^{2+} is also formed as represented in Equation 8. Unlike the previous equation, this is not a reversible process.

$$2Mn^{3+}(\text{solid}) \longrightarrow Mn^{4+}(\text{solid}) + Mn^{2+}(\text{solution}) \qquad \text{Equation 8}$$

Mn^{2+} escapes from the crystal lattice and dissolves in the electrolyte easily especially in an acidic environment, even the presence of a minute amount of H^+ ions hasten this reaction. The leached Mn reacts irreversibly with components of the electrolyte and causes the crumbling of the cathode material framework, some of the products of the leached Mn travel to the anode and poison it thereby shortening the cycle life of the cell.

Jahn-Teller effect is a theory that explains how a non-linear degenerate system undergoes symmetry distortion to lower the symmetry and stabilise the molecule. In the case of LMO, in a high spin environment, the 3d orbitals of Mn ion splits into $t_{2g}^3 e_g^1$ for Mn^{3+} and t_{2g}^3 for Mn^{4+}. The uneven occupancy of the two e_g orbitals on Mn^{3+} allows a closer approach of the electrons from one axis. The electron density will be more concentrated between the oxygen ligands approaching from this axis and the cation, resulting in an elongation or compression of the axis to lower energy. This creates a dissimilar electronic environment around the metal resulting in a tetragonal distortion of the octahedron, where one O-Mn-O axis experiences compression or elongation relative to the others as shown in Figure 2-6. Mn dissolution and the Jahn-Teller distortions lead to over-lithiated samples and consequently, irreversible phase transformations occur.

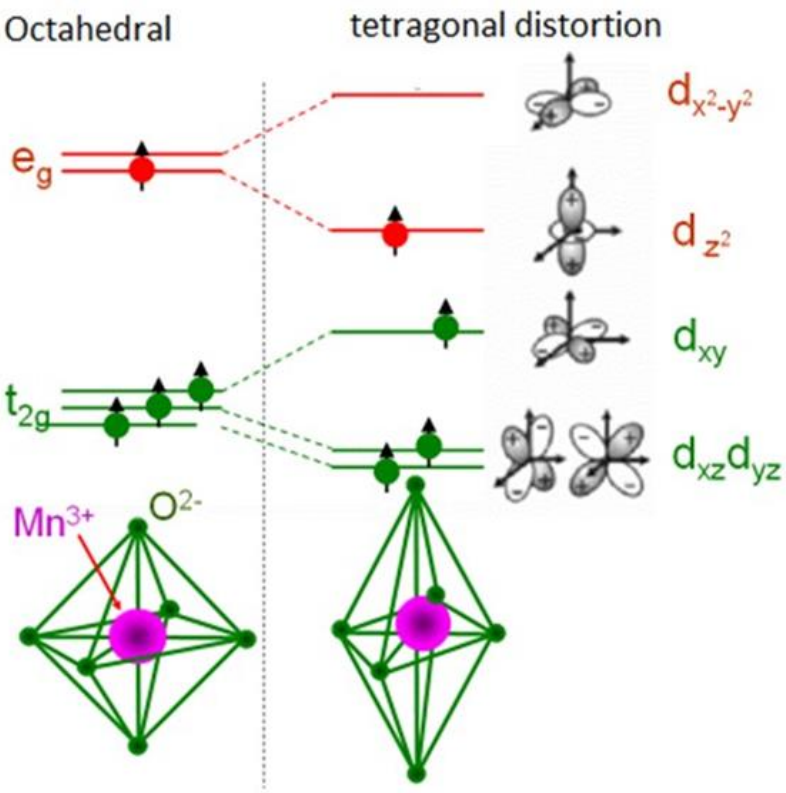


Figure 2-6 Schematic representation of the splitting of the Mn 3d orbital in $Mn^{3+}(d^4)$. [33]

A derivative of LMO was achieved by blending in with Ni to yield LMNO which is Co-free and therefore cheap. It has a cubic spinel with an even higher operating voltage (4.7 V vs Li/Li^+).[34].Owing to the reduced content of Mn^{3+}, degradation due to JT distortions is reduced in LMNO. However, operating at high voltage leads to electrolyte decomposition, formation of fouling by-products and diminished cycle life due to Mn dissolution.[35] The LMNO also suffers from capacity decay because of the side reaction that occur to form a film interphase on the cathode-electrolyte boundary which gradually thickens and impedes lithium ions migration. LMNO is difficult to synthesise since its Ni-O like impurities usually form during synthesis. Researchers have been working on getting the right electrolytes including

solid electrolytes[36,37] water-in-salt electrolytes [38-40] and engineering synthetic routes[41] to overcome these shortfalls.

Polyanions with a general formula XO_4^{3-} (X= S, P, Si, As, Mo, W),[6,] are the other oxide cathode materials that have been investigated. The redox potential of a metal with M = Fe, Mn, Ni, Co in a polyanion (MXO_4) tends to be higher than when with oxygen anion in metal oxides such as M_2O_3 or M_3O_4 and thus gives higher operating voltages; for instance, whereas Co-O-Co gives potential around 3.9 V, Co-O-P-O-Co gives a potential of 4.8 V. The most successful of polyanion cathodes is $LiFePO_4$ (LFP) which has an olivine crystal structure with Li^+ and Fe^{2+} occupying the octahedral sites while the P are on the tetrahedral sites. LFP possesses good characteristics such as high thermal stability and safety, high-power capacity, low toxicity, and low cost.

LFP has been commercialised despite its general low average potential, poorer electronic and ionic conductivity, and lower energy-density. The latter characteristics give LFP a low volumetric energy density. A processing property-correlation approach to mitigate this problem has been to synthesise LFP as small particles but this necessitates coating with more conductive substances such as carbon and cationic doping to cut down on interphase problems. [42,43] This further lowers its volumetric density. Recent studies have focused on transition metal oxide and polyanions, solid-state Li-ion, lithium-sulfur and lithium air batteries. [20 44]

2.2.1. Layered transition metal oxides.

The layered transition metal oxide compounds have a close-packed array of atoms, in which alternating sheets of TM atoms and anions have the lithium sheet inserted into the empty remaining layers, Figure 2-7. Like $LiTiS_2$, the first and most successfully commercialised cathode material LCO bears a layered structure like α-$NaFeO_2$. In LCO, layers composed of octahedrally coordinated cobalt atoms are connected to close packed oxygen atoms in a cubic arrangement bridged by oxygen. The trivalent Co^{3+} and monovalent Li^+ are located on octahedral positions in an ABCABC… stacking sequence, on (111) plane of a rock salt, O3 structure, in an alternating fashion, Figure 2-7. Cobalt forms a low-spin complex with oxygen in LCO with a tripositive state, Co^{3+}. In LCO, all the d-electrons are paired, resulting in a spin number, $S = 0$ and the d electron configuration of $(t_{2g})^6(e_g)^0$.

During LCO cycling, lithium ions move through the hexagonal holes going from one hole to the next creating a series of vacancies within the lithium planes. The ordered layered configuration greatly improves Li^+ diffusion from one octahedral site to the next in a two-dimensional plane resulting in fast improved conductivity.[45-48] The ordered arrangement enhances and supports efficient lithium ions diffusion.

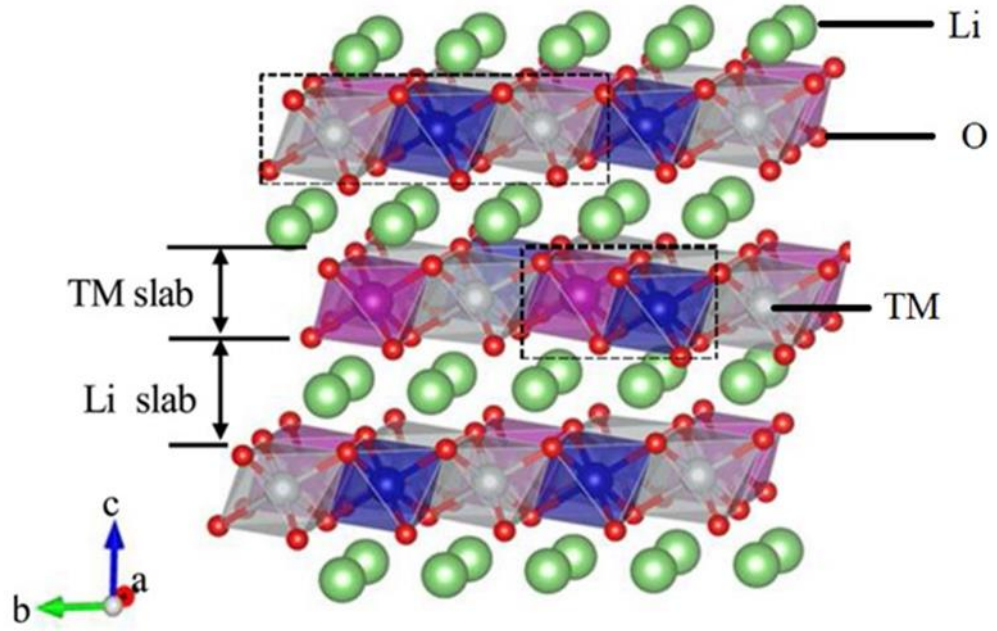


Figure 2-7 Depiction of a layered structure of NMC [48,49]

There is no cation mixing observed between Li^+ and Co^{3+} ions because they differ a lot in size and charge hence, they do not easily replace each other in their relative positions. This cuts out the loss of the ions within the M-O framework and preserves the span of a battery.

The electrical conductivity of LCO changes each time a Li^+ is released. During charging, the remaining Li in $Li_{1-x}CoO_2$ behave more metallic and more conductive. The good electronic character and Li^+ conductivity, (5×10^{-9} cm^2/s), make charging and discharging highly reversible and fast which is consistent with the ability of LCO cathode to cycle at 4 mA/cm^2. Consequently, LCO has a high theoretical specific capacity and volumetric capacity of 274 mAh g^{-1} and 1363mAh cm^{-3}, respectively. However, the dramatic change in conductivity with composition poses a challenge in

performance consistency, especially at low temperatures when both diffusion of Li^+ and electronic conductivity are hampered. LCO's other attributes are low self-discharge, high voltage, and good cycling performance.

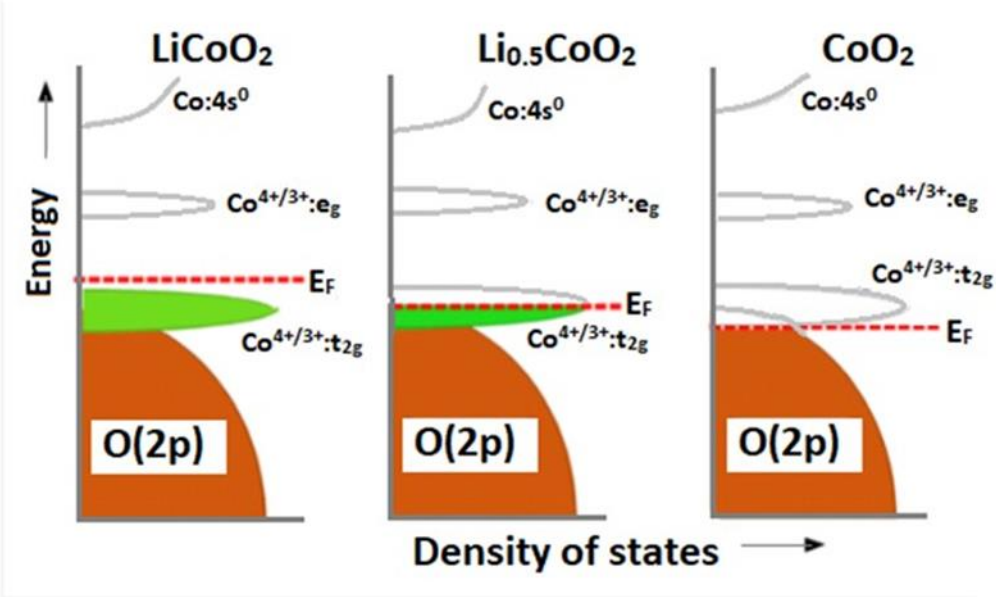


Figure 2-8 Change of qualitative energy diagrams of Li_xCoO_2 as a function of lithium the content.[31]

Contrary to the advantages, the overlap of O^{2-}:2p and Co^{3+}/Co^{4+} energy bands as shown in Figure 2-8, makes it easy for oxygen atoms to be lost from the bulk lattice. This happens whenever $Li_{1-x}CoO_2$ ($x > 0.5$) is reached which means anytime more than 50% of Li ions are removed through charging, oxygen gets lost from the matrix. This means deep discharging of LCO batteries destroys the cathode's framework and, in some cases, irreversibly. This situation worsens at elevated temperatures when significant metal ion dissolution may also occur. Consequently, this raises gas evolution problems, compromises safety, and leads to irreversible

structural modification and capacity fading. Importantly, only about 50% of the theoretical capacity, ~140 mAh g^{-1}, can be reached without this destruction of the cathode material.[31] LCO does not exist as a single uniform phase since the structure distorts when Li composition changes from when completely lithiated to when it is delithiated. This means as Li composition changes, there is some energy loss associated with just rearranging atoms which leads to sluggish Li diffusion. These rearrangements are not 100% reversible and may lead to further loss in capacity and poor cycling efficiency.

The unit cell of LCO adopts a rhombohedral symmetry at elevated temperatures with Li, Ni and O in 3a,3b and 6c sites, respectively, which makes it easy for the molecule to transition into a monoclinic phase which hampers the reversibility of the Li^+ ion movement. This leads to low thermal stability,[31] and fast fading at high discharge currents which make LCO unsuitable for use in high energy thirsty applications.[47] Cobalt is also costly, relatively toxic[31] and there exists politically controversial ways during its mining.[50,51] Therefore, owing to the discussed shortfalls of LCO a concerted effort to replace Co using other 3d transition metals (TM) has been made.

2.2.2. NMC Cathode material

Different TM have been investigated as replacements or partners with cobalt in Li-ion battery materials. Vanadium, nickel, chromium, molybdenum and others were also investigated to try and conserve the layered structure while not compromising much on the good attributes of cobalt in LCO. The

performance of Li-ion batteries depends on the nature of the TM incorporated in the material. [52, 53] For instance, insertion of Co improves cycle life, and conductivity, nickel results in high specific energy and capacity while Fe decreases specific power but increases cycle life. In general, several technical and economic parameters should be considered for successful batteries and those influence which battery chemistry goes commercial. Costs of synthesis and commercial processing are also considered. Table 2-2 shows some commercialised Li-ion cathodes and anode materials and their properties.[54] Blended metals were also investigated. Generally, inclusion of transition metals with higher valency can lead to higher oxygen vacancy content and higher capacity.[55] This resulted in cathodes such as nickel and cobalt and aluminium $LiNiCoAlO_2$ (NCA) and nickel, manganese, and cobalt, $LiNi_xMn_yCo_zO_2$ where x+y+ z = 1 (NMC).[52- 66] However, some metals with high valency and many oxidation states like vanadium may experience some drastic irreversible changes in phases during cycling and the presence of the many options of possible oxides complicates the synthesis. A complementary synergy with different ratios of the metals helps to achieve a cathode with different qualities. For example, in NMC the manganese improves the stability and makes it possible to add nickel with the desired oxidation state that supports the maintenance of the desired structure while allowing desired redox reactions necessary for high capacity. The cobalt maintains the layered structure. Table 2-3 shows a comparison of the traits of the metals in a blend of nickel, manganese, and cobalt. [67]

Table 2-2 Characteristics of some commercial battery electrode materials

Electrode Cathodes	**Potential vs. Li/Li^+ (V)**	**Specific Capacity (mAh/g)**	**Advantages**	**Disadvantages**
$LiCoO_2$	3.9	140	Performance	High cost, limited specific capacity, low thermal stability,
$LiNi_{0.8}Co_{0.15}Al_{0.05}O_2$	3.8	180–200	High capacity and voltage, excellent rate performance	Safety, cost and resource limitations of Ni and Co
$LiNi_{1/3}Mn_{1/3}Co_{1/3}O_2$	3.8	160–170	High voltage, moderate safety	Cost and resource limitations of Ni and Co
$LiMn_2O_4$	4.1	100–120	Low cost, abundance of Mn, high voltage, moderate safety, excellent rate performance.[26,27]	Limited cycle life, low capacity, fast fading
$LiFePO_4$	3.45	170	Excellent safety, cycling, and rate capability, low cost and abundance of Fe, low toxicity	Low voltage and capacity (substituted variants), low energy density
Graphite	0.1	372	Long cycle life, abundant	Relatively low energy density; inefficiencies due to Solid Electrolyte Interface (SEI) formation
$Li_4Ti_5O_{12}$	1.5	175	"Zero strain" material, good cycling and efficiencies	High voltage, low capacity (low energy density)

Table 2-3 Comparison of the characteristics of Mn, Co, and Ni in MNC cathodes.[23]

Parameter	Trend
Chemical stability	Mn > Ni > Co
Structural stability	Co > Ni > Mn
Electrical conductivity	Co > Ni > Mn
Abundance	Mn > Ni > Co
Environmental benignity	Mn > Ni > Co

The cathode material with the general formula of is $LiNi_xMn_yCo_zO_2$ (x +y + z = 1), produces batteries with high operating voltage of 3.0-4.2 V vs Li/Li^+, specific energy of 150-220 Wh/kg, a cycle life of between 1000-2000 cycles, a thermal runaway of 210 °C and a cost of \$420 kWh^{-1} meet most parameters desired for good batteries. NMC layered oxide material is isostructural to LCO and can be expected to perform similarly. NMC can be synthesized in different compositions, the most common of which are NMC333 (also known as NMC111), NMC532, NMC622 and NMC811; the number indicate the molar ratio of Ni to Mn to Co, in that order in a sample. There are also the Li and Mn-rich NMC cathode materials and several other formulations in between. [66,67]

Nickel-rich $LiNi_xMn_yCo_zO_2$ ($x \geq 0.6$) are desirable because they present higher discharge capacity (160-200 mA h g^{-1}), and high energy density at relatively lesser costs than LCO because of lower constituent Co.[66] Ni-rich NMC also presents a possible high cut-off voltage of 2.5-4.6 V vs the Li/Li^+ and is reversible because of the $Ni^{3+/4+}$ redox couple. It also has a high

discharge capacity. However, achieving the high discharge capacity requires deep delithiation at a high voltage. Deep delithiation comes at a trade-off with critical capacity fading and thermal stability because of structural failure. Normally, only <70% of the theoretical 276 mAh g^{-1} is achieved.

NMC111 and NMC532 are more thermally stable with higher cyclability and have been commercially adopted as shown in Table 2-4.[67] In contrast, most nickel rich NMC formulations have not been commercialised except NMC622.[11, 68, 69] The commercial NMC is in use in motor industries including BMW, Chevy, Toyota Prius and Nissan Leaf.

Table 2-4 Physicochemical and electrochemical properties of various NMC cathode formulations.[70, 71]

Formulation	**NMC333**	**NMC532**	**NMC622**	**NMC811**
BET, $m^2 g^{-1}$	0.48	0.24-0.51	0.28	0.49
pH	11.1	11.15-11.56	11.65	12.13
Li_2CO_3 %	0.05	0.08-0.13	0.25	0.64
LiOH %	0.03	0.02-0.1	0.13	0.43
Capacity, mA h g^{-1} at 4.3 V.	154.8	166.1-187.0	175.8	203
Rate Capacity Retention, %	94.8	93.4-94.9	93.4	94.0
% Capacity Retention after 50 cycles	98.3	95.6-99.2	98.1	93.4

Because of the potential improvement in electrochemical performance of Ni-rich NMC, researchers have focused efforts on understanding them and improving on its shortfalls.

2.4. General synthetic routes for nickel manganese cobalt oxide

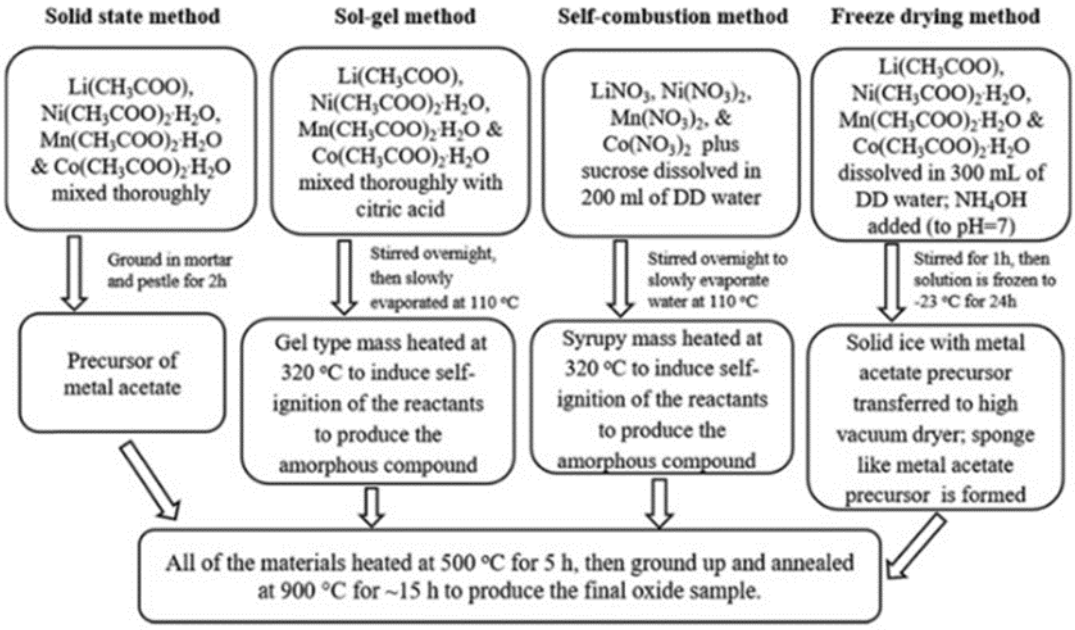
Many research groups have designed methods of synthesis of NMC. The synthetic route taken can influence the powder properties of the cathode material such as the microstructure, tap density, surface area and in turn electrochemical behaviour of the sample. The methods focus on proper mixing of the metal ions before calcining. The mixing stage is believed to have an influence on cation ordering and the microstructure property which highly affect the performance of the material. Metals cations are often introduced as carbonates, acetates, sulphates, nitrates or other salts to form a precursor that finally gets calcined into the oxide.

2.4.1. Sol-gel, solid state, freeze-drying and self-combustion methods.

Scheme 1 summarises some of the methods including the sol-gel,[72] solid state, freeze-drying and self-combustion methods.[73] Sol-gel method focuses on preparing a homogenous gel mixture before calcining.[64, 74] It entails mixing stoichiometric amounts of the metal salts with a chelating agent such as citric acid at moderately high temperatures over a long time and stirring until the mixture becomes a gel which then gets heated to encourage self-ignition to form a precursor product. The precursor then gets calcined in a two-step heating process; first at a lower temperature, followed

by cooling, milling and further calcining at an elevated temperature to form the solid NMC product.

The last heat treatment steps are almost universal to all methods to form highly crystalline materials which are imperative for the desired efficiency of the cathode materials. Calcining has been done in different environments such as oxygen atmosphere or high air flow atmospheres where these two were found to give better performing products than in a normal air environment.



Scheme 1 Summary of some synthetic routes for NMC[75]

2.4.2. Coprecipitation Method

This method involves making soluble solutions of the metal salts in the desired stoichiometric relationship and coprecipitating the metal ions out as either hydroxides or carbonates using a combination of sodium hydroxide

and ammonium hydroxide as the precipitating agent and the chelating agent, respectively.[76-78] When precipitated out as carbonates, sodium carbonate is used as the precipitating agent while ammonium carbonate acts as the chelating agent. The NMC precursor precipitate is then washed and dried. The next step is adding lithium and finally, calcining into an NMC powder. During calcination, hydroxides decompose into metal oxide, and water while the carbonates decompose into the oxide and carbon dioxide in a good supply of oxygen or air. Normally metal sulphates are used as the source of the metal ions.

Researchers always look for a method that can be easily reproduced and the way the reagents are mixed is another variable in the synthesis. Different methods of mixing can have an impact on the microstructural properties of precursors of the NMC materials and consequently affect the electrochemistry of the NMC.

2.4.3. Conventional mixing

When using conventional stirring the reactor is normally upright with the stirrer close to the base of the reactor. Whilst this method has been widely used, it can create multiple regions within the reactor purely because the turbulence created with stirring is concentrated on a small region close to the stirrer while the bulk of the region is unaffected as shown Figure 2-9. Although the speed reached can be high near the stirrer, its sphere of influence is very limited.

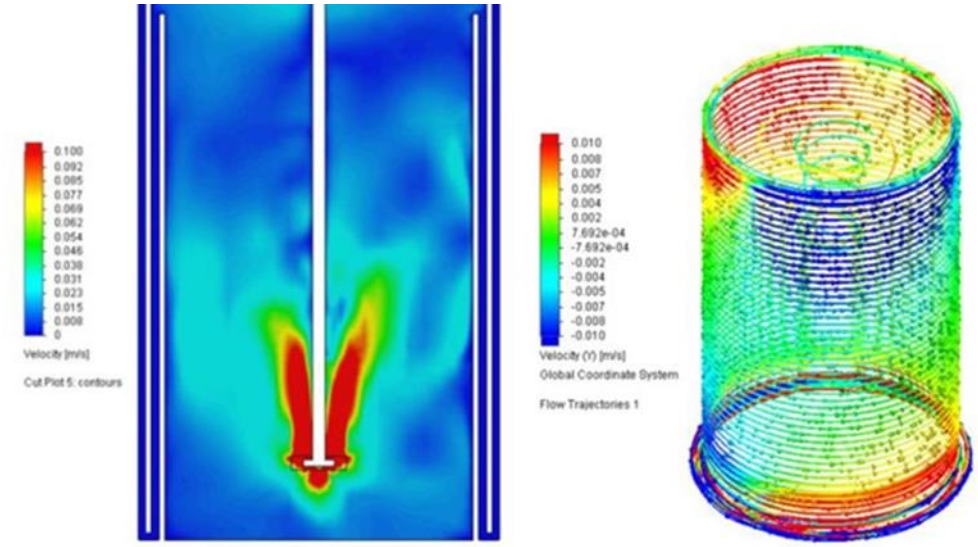


Figure 2-9 Illustration of Conventional stirred reactor and laminar flow reactor

2.4.4. Laminar mixing

Laminar reactors are more efficient to achieve uniform mixing. The flow of particles in laminar mixing is along a larger region and occurs at a slower pace. This allows for better and longer mixing as particles move along the path. Laminar reactors are also lauded for their scalability, continuity and ability to offer controllable conditions which results in higher purity due to the uniformity in mixing, Figure 2-9. The laminar flow can be achieved by using a Laminar Continuous Taylor Reactor (LCTR), Figure 10. The LCTR is a temperature and pH controllable jacketed cylinder with a rod at the centre that can spin at a controllable speed, which agitate the reagents and effects mixing. The reagents can be fed in by pumping at a controllable rate through holes near the start of the vessel. The turbulence created allows mixing to occur throughout the length of the reactor.

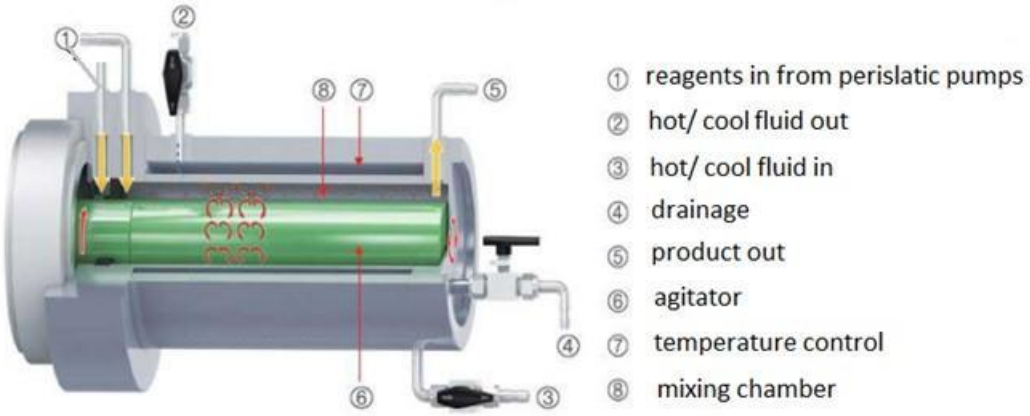


Figure 2-10 A cross section of a typical Laminar Continuous Taylor Reactor.

Because of the fashion in which particles move, they do not reach very high speeds which allows for relatively slow nucleation to occur. An added advantage to using LCTR is that a continuous flow of reagents is possible making the system easily scalable.

2.5. Challenges of NMC cathode material

Several authors have conducted comprehensive review analysis on Ni-rich NMC cathode materials, [79, 80] and identified battery degradation, capacity fading and thermal instability as primary drawbacks of this material. Chemical, structural and mechanical degradation mechanisms can happen during different stages in the life of the Li-ion cathode material. It can happen on the initial contact of cathode material with the carbonate electrolyte, during charge-discharge cycling and even in storage of the cathode powder.

They all lead to capacity and voltage fading. The degradation mechanisms are sometimes interrelated, and they are going to be discussed next.

2.5.1. Residual lithium compounds

Chemical degradation due to lithium compounds has been described by Kim et al. as also originating from the powder structure.[9] The powdery surface of NMC material is clad with residual Li compounds such as LiOH and Li_2CO_3 which are formed during synthesis and continue to form during storage and sometimes even during charge-discharge cycling. [9, 81] Nickel-rich cathodes are more susceptible to the presence of the Li compounds because the presence of these compounds on the surface is directly proportional to the fraction of nickel in the NMC formulation, [13] the higher the composition of nickel, the higher the amount of these compounds. Some of the different ways in which these lithium compounds affect the cathode materials are as follows: -

Firstly, they cause parasitic side reactions with the electrolyte.[82] Lithium carbonate has a higher affinity for water and creates ideal conditions for solubilising more Li from the electrolyte, normally $LiPF_6$, to form hydrofluoric acid (HF). Corrosion of the electrode occurs in the presence of highly reactive HF. Equations 9-13 summarise some of the reactions including dissociation, and hydrolysis that can occur as side reactions, but which hinder smooth lithium-ion conductivity.

$$PF_6^- + Li^+ + 2e^- \rightarrow 3LiF \downarrow + PF_3 \qquad \text{Equation 9}$$

$$\boldsymbol{LiPF_6 \rightleftharpoons LiF + PF_5} \qquad \text{Equation 10}$$

$$PF_5 + H_2O \rightarrow POF_3 + 2HF$$

Equation 11

$$PF_5 + 2xLi^+ + 2xe^- \rightarrow Li_xPF_5 \downarrow + xLiF \downarrow$$

Equation 12

$$POF_3 + 2xLi^+ + 2xe^- \rightarrow Li_xPOF_{3-x} \downarrow + xLiF \downarrow$$

Equation 13

Kim reported that the acidic conditions aggravate and hasten the solubilizing of the metal ions and corrosion of the electrode.[83] Moreover, the solid precipitates formed add to the passivation layer on the electrode, the cathode electrode interphase (CEI) and impact negatively on the diffusion of lithium ions during charge-discharge, causing high charge transfer resistance, increased impedance and capacity decay.[84,85] Lithium is irreversibly consumed in this scheme which results in irreversible cycling and thus voltage fading. This encourages dissolution of Li from the host structure to form several solids which deposit on the electrodes.

Aurbach et al. used an electrochemical quartz crystal microbalance to weigh the mass changes of electrodes while also monitoring charge of the atoms. These in-situ studies investigate different solid lithium deposits and dissolution with different solvents as electrolytes and reported that formation of lithium-containing surface films form during ageing upon cycling.[85,86] The technique allowed them to follow mass change from the onset when electrodes were first exposed to the electrolyte to when deposits formed on the electrodes. The solid precipitates formed can add to the passivation layer, the cathode electrode interphase (CEI) and impact negatively on the diffusion of lithium ions during charge-discharge, causing high charge

transfer resistance, increased impedance and capacity decay.[58,69,87] Lithium is irreversibly consumed in this scheme which results in irreversible cycling.

Secondly, the presence of Li compounds enhances gas evolution reactions of the NMC. The reactions that occur can be classified as acid-base reactions between Li_2CO_3 and HF represented by Equation 14. Berkesm et al. reported that Li_2CO_3 residues undergo several reductive transformations of the electrolyte that lead to evolution of CO_2 and CO as represented in Equation 15.[88]

$$Li_2CO_3 + 2HF \longrightarrow 2LiF + H_2O + CO_2 \quad \text{Equation 14}$$

$$2ROCO_2R + 4Li^+ + 4e^- \longrightarrow (ROLi)_2 + LiROLi + CO + CO_2 \quad \text{Equation 15}$$

The initial charge cycle normally encompasses the formation of a solid electrolyte interphase (SEI) which protects the electrode material from further direct contact with the rest of the electrolyte. However, if this layer gets too thick due to continuous deposition of the solid products of electrolyte degradation, it leads to capacity fading. Also, LiOH makes the slurry basic and gelatinous during fabrication which can cause corrosion of the aluminium current collector and lead to uneven coating of the current collector.[89,90]

Of concern is the effect of the gases released which always pose a threat of thermal runaway. According to Bang et al.'s proposal, there are four steps that lead to thermal runaway in layered cathodes.[91]

Firstly, there is a slight structural deformation into a spinel-like crystal structure that goes along with the loss of oxygen from the cathode material

that occurs during normal cycling. Then step (2) involves the oxygen lost which reacts with components of the electrolyte with a low flash point such as ethylene carbonate (EC) in an exothermic reaction. The heat evolved in step (3) provides enough activation energy for more severe decomposition of the cathode material which releases even more oxygen and heat. Finally step (4) involves both the heat and the oxygen, which fuel combustion of the other components such as the carbonates releasing carbon dioxide, water and more heat that can cause thermal runaway.

Similar steps have been associated with changes observed during cycling over a voltage range where three distinct stages of gas evolution were identified. Step (1) occurs at lower voltage where oxidation of the anode and electrolyte solvents generate CO_2, ethane and mostly ethene. This happened at approximately 3.7 V and was followed by gas consumption stage around 4.1 V, and finally oxidation at much higher voltages of ~4.7 V which marks the second stage of evolution with the gases H_2, CO, O_2 and CO_2 being released.[13,35,35,92] Elevated temperatures also encourage more gassing because of faster oxidative decomposition of the polymeric binder and other components.

2.1.1. Phase transitions and capacity fading

Phase transitions occur commonly during the charge-discharge process of layered cathode materials. During charging and discharging, manganese redox couple, $Mn^{4+/3+}$, does not get involved because its energy band lies above that of O^{2-}:2p as seen in Figure 2-11; only cobalt and nickel are

involved. During charging, NMC produces a highly oxidising and unstable species of Ni^{4+}. When in contact with the electrolyte, Ni^{4+} drives phase transitions on the surface of the material. This is because it easily reacts with oxygen from the electrolyte to form stable Ni-O like solids. As nickel escapes from the lattice phase transitions from the layered, *R*$\underline{3}$*m*, it transitions into spinel-like *Fd*$\underline{3}$*m* lattice which can easily transforms into the *F*$\underline{3}$*m*$\underline{3}$*m* rock-salt phase. The rock-salt phase is inactive during cycling and is not reversible. This is prevalent in Ni-rich cathode, and it destroys the structure of the cathode and consumes the electrolyte.

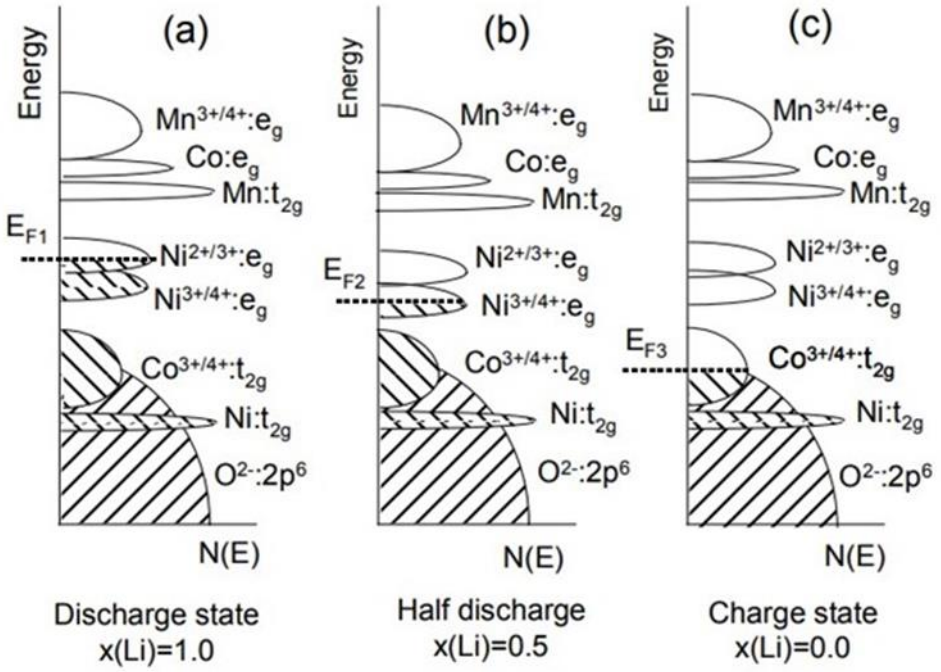


Figure 2-11 Change of qualitative energy diagrams of NMC showing relative Fermi level of the $Ni^{4+/3+}$ and $Co^{4+/3+}$ redox couples as a function of lithium content during charging (a) x = 1, (b) x= 0.5 (c0 x = 0)[31]

The $Ni^{3+/4+}$ energy band overlaps with the O^{2-}:2p bends. In a charged state at high voltage, there are more species of highly unstable Ni^{4+} which

spontaneously gets reduced to the divalent species when it reacts with organic electrolytes. The Ni^{2+} ions react with oxygen to form stable Ni-O-like species which form layers on the bulk of the cathode. The layers negatively impact the electronic and ionic conductivity properties of the cathode material. Concurrently, some oxygen gets irreversibly lost from the bulk cathode metal-oxygen framework when it oxidises into molecular oxygen resulting in vacancies in the oxygen layer and crumbling of the structure. These events introduce a low-energy pathway for manganese ions to migrate from the octahedral sites of the TM layer to tetrahedral sites in the Li metal layer, since Mn is responsible for the integrity of structure, a slip in position starts up phase transitions leading to voltage and capacity decay. [10,94,95] Replacement of occupancy by Mn in the Li layer changes Li ability to diffuse and reduces the available Li for cycling thus, capacity fading occurs.

Bak et al. carried out an in-situ technique that combines time resolved synchrotron X-ray diffraction and mass spectroscopy for Ni-rich NCA and NMC and they were able to show that the phase changes coincide with oxygen and carbon dioxide release as shown in their results in Figure 10. [96] Most of these catastrophic events to the cathode material occur more at elevated temperature when cycling at high voltage.

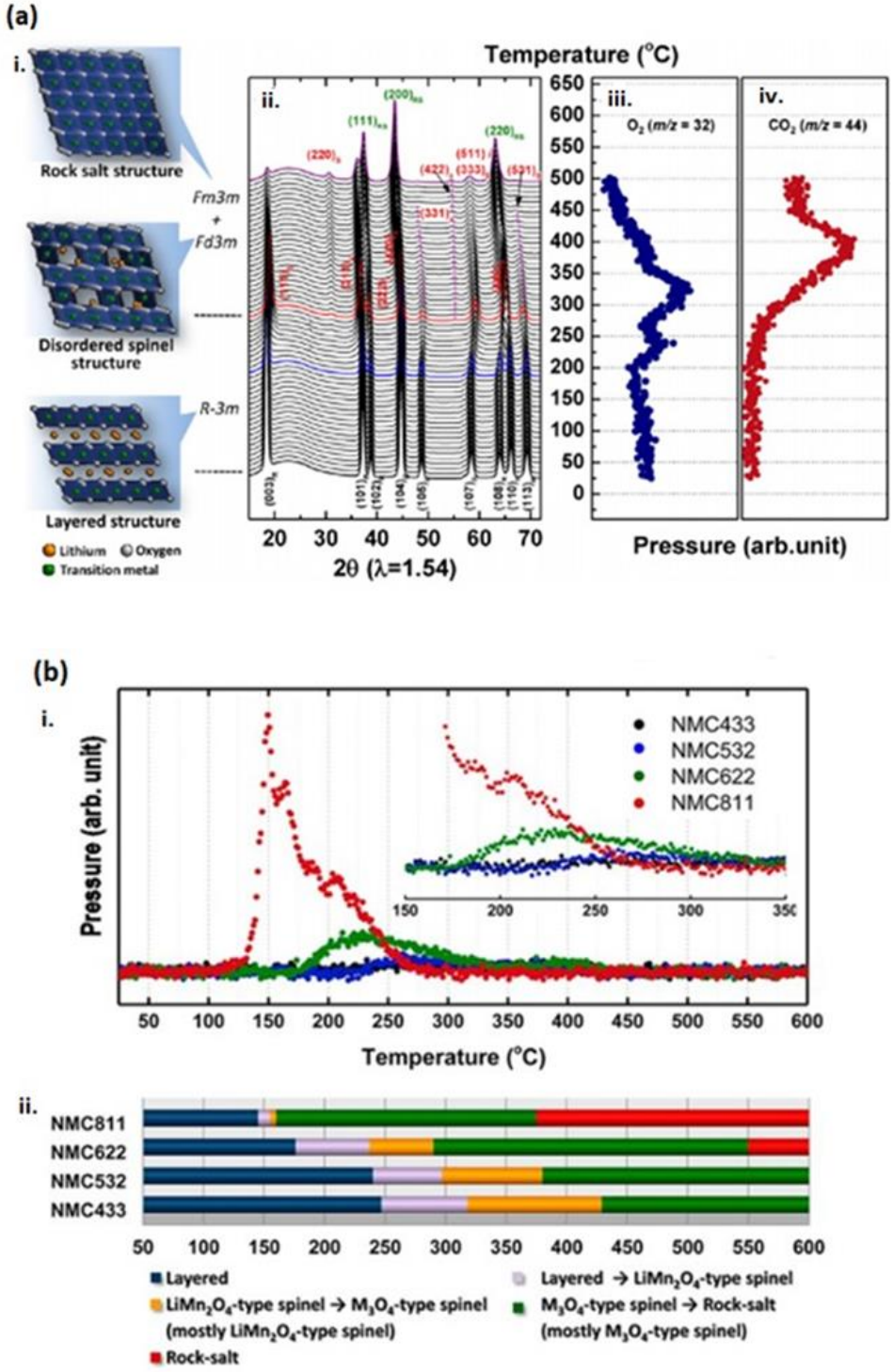


Figure 2-12 Phase transition and simultaneous gas evolution pattern for (a) NCA showing (i) crystal structure models for rhombohedral(layered), spinel, and rock-salt structures. (ii) TR-XRD patterns and simultaneously measured mass spectra (MS) profiles for(iii)O_2 and (iv) CO_2 released [38, 96] (b) MS profile for several samples of NMC for the release of O_2 together with measured phase transition measured with TR-XRD. [36]

The high composition of Ni encourages a lot of cathode-mixing between Li^+ and Ni^{2+} ions since they have similar ionic radii of 76 and 69 Å, respectively.[93,97] This interferes with the two-dimensional diffusivity of Li ions.

In summary, structural phase transitions, cathode mixing, Ni-ion dissolution, electrolyte decomposition and gas evolution all affect Li^+ diffusion and in turn its conductivity and lead to capacity fading.

2.5.3. Structural instability

In their review Sun et al. focus also on the development of microcracks within the secondary particle which they documented as one of the major setbacks of Ni-rich NMC.[99] These are caused by anisotropic strain and lattice contraction within individual particles.[100-102] Regular charge-discharge cycling can also lead to weakness of the secondary particles because of expansion coefficients and volume changes experienced due to Li intercalation.[103-106] This happens because of inhomogeneous changes in the electrostatic forces during cycling. The electrostatic force acting on the bonds within the particle changes as the overall charge of a particle changes during cycling because the bond lengths and polarity also change, this adds stress on the particle. For instance, repulsion forces within the oxygen layer are different from the attraction forces the oxygen layer has towards the transition metal layer and the extent of these electrostatic forces change during cycling depending on the level of charge. In addition, the development of microcracks further facilitates phase transitions to rock-salt structure because they allow seepage of the electrolyte in between which

increases the electrolyte-electrode surface area interaction and consequently cell impedance increases because of charge transfer resistance from increased SEI thickness. The increased resistivity causes capacity fading. Li et al. showed that removing 80% Li ions creates a 5% lattice shrinkage. This phenomenon has been observed for both Ni-poor and Ni-rich NMC formulations and may also lead to catastrophic volume changes[38-41, 103] which can cause collapse of the particles. In general degradation mechanisms for Ni-rich NMC can be summarised in Figure 2-13.

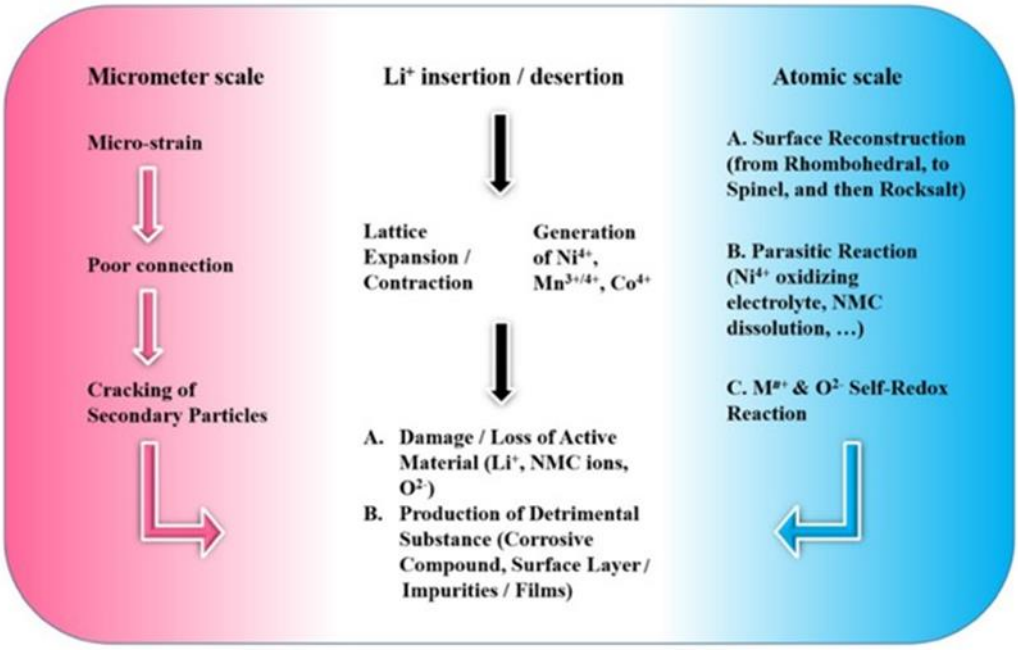


Figure 2-13 Summary of degradation mechanisms of Ni-rich NMC[104]

Cracking accompanied by volume expansion that occur in secondary particles is another of the notable modes of NMC811 and some researchers have been involved in quantifying it.[105] In their recent review Krause et.al puts together several papers that credit structural instability to expansion

which happens during charging and discharging cycles.[106] This causes pressure in batteries which can lead to compromised performance and safety issues. Sometimes it even affects contact within components of a battery and may lead to gas evolution. These are crucial even for assembled batteries.

Other problems of NMC are connected to cell fabrication. Ni-high NMC has a low density which translates into low volumetric energy density. Compressing the material to try and increase the density causes particle integrity failure and reduces the amount of electrolyte that can get in, to wet the material. Inadequate electrolyte reduces ionic conductivity while increasing thermal instability because chances of self-heating increase for a highly compressed electrolyte. Polycrystalline material is more vulnerable to the collapse of the cathode particles due to thermal decomposition when under pressure than single crystal particles. This thwarts efforts to increase energy density of the electrodes by the compression of the material during battery fabrication.

2.6. Approaches to suppress the limitations of NMC

Several strategies research groups have come up with strategies to improve and place NMC at a position of wide applicability. These approaches will be discussed next.

2.6.1. Washing

Washing the electrode material to eliminate residual Li compounds has been done before. In a different setting washing was done however its

success was short-lived because although the washed product initially had less topical Li and showed higher capacity, it became more prone to chemical attack than the unwashed sample upon cycling.[107] Washed samples ended up with higher amounts of Li_2CO_3 even in storage. This suggests that NMC should not be washed but it also suggests the stringent storage environment is required for NMC-rich cathode materials. It should be stored in a dry, oxygen-free environment.

An interesting report by Reddy et al. follows a synthetic route that involves washing the cathode material thoroughly after calcining to remove excess salts. However, the work was focusing on doping LCO with Mg and was not set to compare washed material with unwashed material, but the resultant washed products still gave decent electrochemistry even after numerous charge-discharge cycling.[108] This can further be pursued to investigate the effect of dual treatment of washing and doping.

In industry washing would add a processing stage which increases the time and cost factors. A one-pot solid synthesis to eliminate the wash stage would be preferred. Some researchers use techniques like improved electrolytes and process optimization such as changing the atmosphere during calcining and other battery technologies like particle size optimization and tweaking annealing ways to try and improve and overcome the shortfalls of Li-ion cathode materials. [13,109,110] Amongst the tried methods many authors believe the physical barrier methods, doping and coating, work best at improving the stability of the structure.

2.6.2. Physical barriers

Gradual degradation of performance of cathode material can be stopped or slowed down by applying a physical barrier between the electrode material and the electrolyte. The barrier can raise the activation energy for the reactions that cause degradation. Physical barriers can be categorised into bulk or surface coating which refers to doping, and coating, respectively. Chen et al. investigated and defined coating by dividing it into three categories namely, surface coating, core shell structure and ultra-thin film coating. [111] All these are done to stabilise the surface structure of NMC, improve the rate capability and make the material more heat tolerant during cycling. Coating can promote cathode stability by creating a physical barrier or by raising the activation energy for parasitic surface reactions that reduce the efficiency of the cathode material and to maintain the structural integrity of the cathode material.

2.6.3. Doping

Doping refers to the introduction of a small amount of one or more elements as impurities into a substrate to alter the substrate's properties. The doping ions partially substitute the metal or oxygen ions in the host material, Figure 2-14. This usually involves adding a small amount of the dopant's precursor as one of the reactants during synthesis, before calcination. The dopant then replaces either some of the TM or the O^{2+} ions in the lattice. They can enhance the overall performance, improving conductivity, and structural stability and suppressing detrimental side reactions without changing the intrinsic structure of the electrode material. Dopants may improve

conductivity by lowering the activation energy for the insertion of lithium ions for better cyclability and voltage stability. They also reduce charge transfer resistance thereby suppressing impedance and improving electronic conductivity. Sometimes this is achieved when the dopant reaction with oxygen and other components of the electrolyte is favoured over the reaction with TM in the lattice and the products of such reaction can be better-conducting compounds which improve ionic and electron transport.

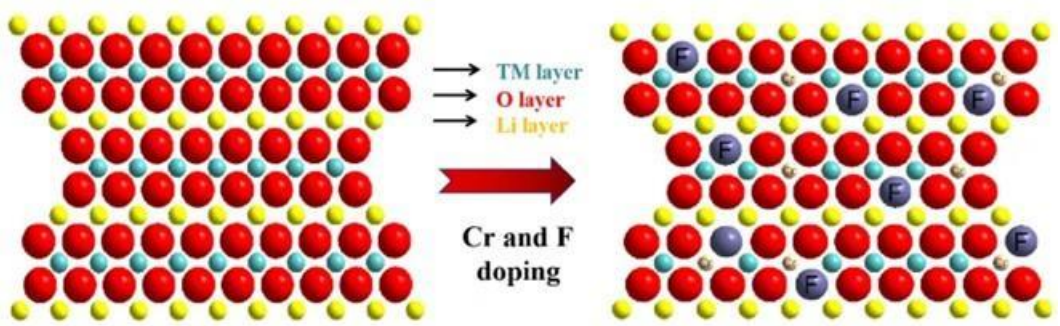


Figure 2-14 Graphical representation of doping.[112]

Side reactions with the electrolyte can also be suppressed or quenched by acting as scavengers of destructive molecules like HF. Also, dopants can act on the host structure to prevent undesired phase transitions by creating better morphology and microstructure that improve stability or support better performance. Different elements have been used for bulk doping of Li-ion material using ions of both nonmetals and metals like B, Br, S, F, Mg, Al, Zn, Zr, Mo, Nb, Co, Ti, Cr, Fe, Cu and even rare earth metals like Gd, Sm, Nd, La and Ce.[113-123]

Aluminium has been reported to be good at stabilising the surface chemistry and reducing charge-transfer impedance of the cathode material, thus improving conductivity while Mg has been reported to change the surface chemistry of the electrode and to suppress the high activity of Ni^{4+} which triggers most of the reactions that lead to structural collapse.[115, 117,118,120] A good dopant must also be of low cost and easily available hence, aluminium and magnesium are popular and more favoured. Lithium-ion cathodes doped with Mg and Al displayed more capacity retention during cycling, and less charge transfer resistance. Studying their surfaces revealed some Al or Mg molecules on the surface which were more conductive and thus good for ionic conduction.[120,122] Aurbach et al. reported that aluminium prevents oxygen evolution by hindering the migration of Ni ions from the TM layer to the Li layer by changing the redox properties of the Ni, thus stabilising the structure.[120] Essentially this influence leads to higher cation ordering as less Ni^{2+}/Li^{+} cation mixing occurs which also improves lithium-ion migration channels. Magnesium was also found to elicit similar behaviour in the study of Mg-doped NMC622.[113]

2.6.4. Surface coating

Surface coating refers to forming a physical film as a way of curing the cathode material. A coat creates a physical barrier between the electrolyte and the electrode material and can improve the electrochemical performance of cathode materials through different mechanisms of preventing most of their known drawbacks. Most coatings are metal oxides, silicates and some electrochemically inactive species such as metal

fluorides, tungstates and aluminates and even coating with other Li-ion cathode materials and creating a hybrid of cathode materials. [6, 99,123-126] NMC coated with Al_2O_3 displayed 40% improved cycling performance and much lower increase of the charge transfer component of the impedance than its uncoated counterpart.[120] A hybrid of Ni-rich NCA and NMC displayed improved properties over the individual cathode materials.[91] The hybrid had a higher discharge capacity, longer battery life, less cracking of the particles, improved thermal stability and lower impedance, even after 1000 cycles.

This is done by engineering the core shell of the cathode to be of the Ni-rich family which are inferior in capacity retention and coating them with a thin layer of Ni-poor cathode. The thin layer allows for the extraction of Li ions from the core material while offering a protective layer from possible surface reactions responsible for fast fading. Oxides of aluminium, zirconium, zinc are scavengers of HF which often triggers the dissolution of transition metals from the cathode. Adding some phosphoric acid to change to raise the pH of the slurry. These results seem to corroborate work by Kang and Thackery who changed acidity of the cathode material by fluorinating the cathode material.[98] Yan et al. further assert that surface modification of the cathode material is not enough as they suggest ingrowing of solid electrolyte into the layered Ni rich cathodes.[125] When solid electrolyte is infused it allows fast ion diffusion, it cuts out detrimental effect of SEI experienced with liquid electrolyte and penetration of the electrolyte into the microcracks.[127] Some researchers have focused on managing the synthetic

route to have layered material that has a controlled core and shell composition.[77] They argue that bulk solid synthesis leads to material with varied metal content and in turn density which leads to more anisotropic cracking during cycling, [77,80] controls the synthesis by systematic coprecipitation of the metal hydroxide precursors.'

2.7. Characterization techniques of NMC cathode materials

The study of LIBs falls under energy, materials and electrochemistry. And due to its ever changing and evolving chemistries a lot of work has gone into comprehending the properties and characterization of these cathode materials. The characterization techniques can be classified into the physical techniques and the electrochemical techniques.

2.7.1. Physical techniques

2.7.1.1. Crystal lattice and morphology

X-ray diffraction studies have been applied to physically characterise cathode materials. This is important because the electrochemical performance of cathode materials has been strongly correlated to its lattice parameters and crystal structure. X-ray diffraction is a crystallographic technique that is employed to study pattern and symmetry of crystalline solids. It is a non-destructive rapid analytical technique that is used to identify phases in crystalline material and even give information on the dimensions of a unit cell. Solid state can be used to describe a continuum from perfectly arranged particles to a complete disorder of particles which correspond to perfectly crystalline particles or amorphous solid. XRD helps

to classify crystals into small pockets known as systems which tell about the symmetry and arrangement of atoms in a unit. X-rays are a form of electromagnetic radiation with much shorter wavelengths than visible light, of the order ~10^{-1} nm. In agreement with $E = h\nu$, X-rays have much higher energy than visible light. The background for this technique lies on the ability of crystalline materials to diffract monochromatic light in three dimensions. X-ray radiation represents displacement of electrons from the innermost K shell and electrons from outer shells replacing the displaced electrons thereby emitting X-ray radiation. The ray gets filtered into monochromatic incident radiation which are bundled and directed to interact with particles of a rotating sample. The intensity and angles of the reflected X-rays is used to create a three-dimensional picture of the density of electrons. The angles of the diffracted light will depend on the size and symmetry of the unit cell of atoms which can be indicative of the chemical bonds and their crystallographic order within the crystals. The relationship between wavelength of the electromagnetic radiation, the diffraction angle and the lattice spacing is expressed in Bragg's law, in Equation 16.

$$n\lambda = 2d_{hkl}\, sin\, sin\, \theta \qquad \text{Equation 16}$$

In a crystal the atoms are connected through the imaginary parallel lattice planes miller indices *hkl* which represent the electron densities in space. A reflection is connected to imaginary evenly spaced sheets that run through the centres of atoms. The miller indices describe the positioning of these sheets and d is the distance or spacing between them. X-rays from adjacent diffracted from adjacent planes will display a constructive interference if the

angle θ between them is an integer multiple of the wavelength. The reflections for a particular wavelength are then indexed to reflect unit-cell parameters, bond lengths, angles and space group.

Ideal crystal would have atoms positioned at perfect periodic positions in a lattice which will give rise to narrow peaking. When scanning happens through a range of 2θ degree angles, all probable diffraction rays can be detected, collected and counted. Fluid or amorphous solids' atoms interact differently with the incident ray and display anisotropy and will result in the broadening of peaks.

Both ex situ and in-situ XRD studies have been done on NMC material. Ex situ XRD studies allows for the determination of crystal phase structure which is greatly enhanced when used in conjunction with Rietveld refinement. NMC has a pure phased structure indexed for α-$NeFeO_2$ and an R-3m space point group. XRD pattern and Rietveld refinement can be used to determine the lattice expansion or contraction especially in cases where slight modifications to the structure like addition of a dopant has happened to explain incorporation of smaller or bigger atoms. Another application of ex situ XRD is to reveal the presence of impurities in the bulk structure. A pure phase bulk will have a diffraction pattern that can be compared to a documented indexed script card, however in the presence of an impurity extra peaks will be seen. This is usually obvious when a sizable bulk phase of the impurity is present. Sometimes the extra peaks are not

discernible but peak shifts may occur. Moreover, the relative positions of the peaks and relative intensity often tell how open the lattice is for Li migration. Splitting of peaks (110)/(108) and (006)/(102) represents a well-layered hexagonal structure which is needed for high performance of layered structure. Additionally, the merging of these twin sets of signals, indicates a shift of structure to rock-salt phase which does not allow reversible Li intercalation and so affects the energy density. Interestingly, ex situ XRD has also given an insight on degree of cation mixing because performance of NMC material is best when there is less cation mixing. The ratio and intensity of the peaks such as $I_{(003)}/I_{(104)}$ indicates the degree of cation mixing. When the ratio <1.2 it indicates sizable cation mixing. Cation mixing occurs because of similar ionic radii of the metal cations to that of the Li^+ ions and for NMC the biggest concern is the mixing of Ni into the layer of Li layer. Cation mixing robs the structure of the available Li ions for intercalation and it messes up the 2-dimensional Li ion corridors. When Li does not move freely, capacity becomes low.

Some researchers have carried out in-situ XRD where they monitor the change in the XRD during charge-discharge process. [104] This has shown that structural changes as delithiation occurs are an inherent property of NMC. They were able to see how the structure oscillates between R3m and Fd3m during NMC battery cycling. Importantly, it has shown the emphasis of the a-axis and c-axis lattice parameters which are indicative of the openness of the channels through which Li ions migrate within the crystals

during cycling. In-situ studies on the other hand have helped to indicate that during the charge-discharge cycle, there are changes in the lattice parameters which are a nature of NMC. It showed how shrinkage of both the a-axis and c-axis lattice parameters are an anisotropic change that has been linked to degradation of NMC structure. Other in-situ studies were done to monitor gassing and thermal changes. [95] In all cases it was observed that when degradation occurs, the structure changes from the layered rhombohedral R3m to spinel-type and to rock-salt, which does not allow reversible intercalation of Li ions. In this work we used ex situ XRD studies.

2.7.1.2. Morphology

Transmission electron microscopy (TEM) and scanning electron microscopy (SEM) are often used to study the microscopic nature of NMC and other cathodes. The shapes of the particles and their aggregates, whether needle like, elongated, spherical or any other shape can be studied using microscopy. Microscopy can also be used to study changes in particle shape and development of microcracks post cycling that show structural damage. Usually, this post-mortem analysis involves disassembling the coin cells or batteries in a glove box, washing away the electrolyte off the electrodes, and finally investigating the changes using SEM. They can be used to estimate both secondary and primary particle sizes. TEM images can also be used to show coatings and measure its thickness. High resolution transmission electron microscopy (HRTEM) can also be used to

show and measure the fringe lattices and imaging of subregions on cathode material.[65,69, 95, 127,]

2.7.1.3. Chemical analysis

One important method of analysing NMC-based cathodes is by conducting an elemental analysis to establish the chemical composition. This is a semi-quantitative technique that can be used to compare batches of the cathode material with especially those that have been modified by either adding dopants or coatings or even gaining some elements through storage. Energy dispersive spectroscopy (EDS) is a mapping analysis tool that is used to find the spread and distribution of individual elements within a sample, and it can also semi quantitatively estimate the percentage composition.

X-ray photoelectron spectroscopy (XPS) is another technique that can be used to analyse the surface of the NMC making it possible to quantify and identify elements. Through XPS transition metal elements, their electronic state and oxidation states within the material can be established. This is made possible by the binding energies which are specific and characteristic to elements' electronic states. The individual peaks' area and intensity can be monitored to establish changes in the amount of the transition metals. Orbitals of the metals like the 2p for Ni, Mn, and Co together with the 1s for oxygen are used to reveal the oxidation states through the positions of $2p_{1/2}$ and $2p_{3/2}$ because the binding energy of each state is located at a different position from the other. XPS has also been used widely to pick out the

presence of impurities in NMC material. Elements like C(1s) in carbonate has been tracked a lot to differentiate between freshly prepared samples and samples that have gone through degradation already.[128]

2.7.2. Theoretical background of electrochemical techniques

In battery chemistry, electrochemistry can be used for characterising the material, diagnosis, measuring and testing the effectiveness of material as an electrode material. Cyclic voltammetry (CV), charge/ discharge tests and electrochemical impedance spectroscopy (EIS) will be discussed as analytical techniques used to characterise NMC cathode in this work. It is important to explain that these techniques are applied after fabricating coin cells using NMC as the cathode and lithium foil as the anode to make half cells, the details of the fabrication will be included in the experimental section.

2.7.2.1. Cyclic voltammetry

Cyclic voltammetry is an analytic technique used widely in electrochemistry to characterise electrochemical systems. CV is a very versatile technique which offers a way of scanning through changing potential of a cell at a given rate to locate the redox potentials between specified potential limits for an electroactive substance while extracting information about the changing current response and adsorption properties.[129] CV can be used to study several aspects of the electroactive material including determination of electroactive species, its concentration, mechanism of operation and even reaction kinetics while determining whether it is a charge transfer or

mass transport operation and determining whether it is reversibility. With reference to batteries CV can be used to determine the voltage at which Li^+ ions intercalates/deintercalates, Li^+ diffusivity, capacitive reactions and stability of the system.[130]

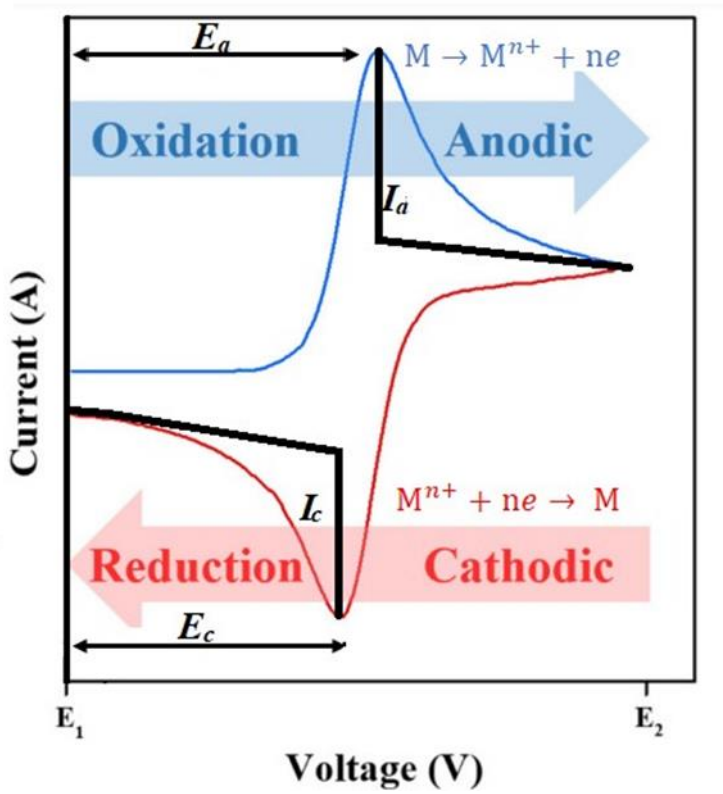


Figure 2-15 A typical cyclic voltammogram

During the acquisition of a cyclic voltammogram the potential of a stationary working electrode is swept from initial value (E_1) to the final value (E_2) and triangulated in a wave form back to the E_1. As this happens, a potentiostat monitors the current response for the electrochemical reactions that occur on the electrode interface as a function of time. The slope of the voltage change over time is the scan rate defined in units Vs^{-1}. A cyclic voltammogram shows a current peaking whenever redox processes take place on the interface and so it records current response as a function of

the applied voltage, Figure 2-15. In the forward potential sweep anodic current response will be obtained and a cathodic current response on the reverse scan. Important parameters from a cyclic voltammogram are the anodic potential and peak current, E_a and I_a, the cathodic potential and peak current, E_c and I_c, respectively These can be used to determine the reversibility and stability of a redox process. And it is this information that can be used further to inform on the thermodynamics of the redox reaction. Although the shape of the voltammogram can inform on the degree of reversibility where a reaction can either be reversible, quasi-reversible or irreversible,[131] as shown in Fig.2-16, it is through calculations using Equation 17 that the determination can be confirmed to be a reversible equation. A redox reaction in which the oxidised and the reduced species are stable, and the electron transfer is rapid at the working electrode interface will produce a reversible couple.[132] A reversible redox system satisfies Equations 17 and 18 at 25°C. The separation between the anodic and cathodic potential in volts, $\triangle E_p$, is independent of the scan rate, it also has a ratio of peak current as unity, $i_{p,c}/i_{p,a} = 1$.

$$\Delta E_p = E_a - E_c = \frac{RT}{nF} = \frac{0.058}{n} \; at \; 298 \; K \qquad \text{Equation 17}$$

where F is the Faraday constant, *n* is the number of electrons transferred, R is the gas constant and T is the temperature in Kelvin. Moreover, the peak currents are proportional to the square root of the scan rate according to Equation 18, Randels-Sevcik equation. [133]

$$i_p^{rev} = \pm(2.69 \times 10^5)\, n^{\frac{3}{2}} \times ACD^{\frac{1}{2}}v^{\frac{1}{2}} \quad \text{at 298 K} \qquad \text{Equation 18}$$

where A = area of the electrode, C = bulk concentration, D = diffusion coefficient and *v* = scan rate. Owing to the complicated applications of the equation, a commonly applied approximation for a reversible system is given by Equation 14.

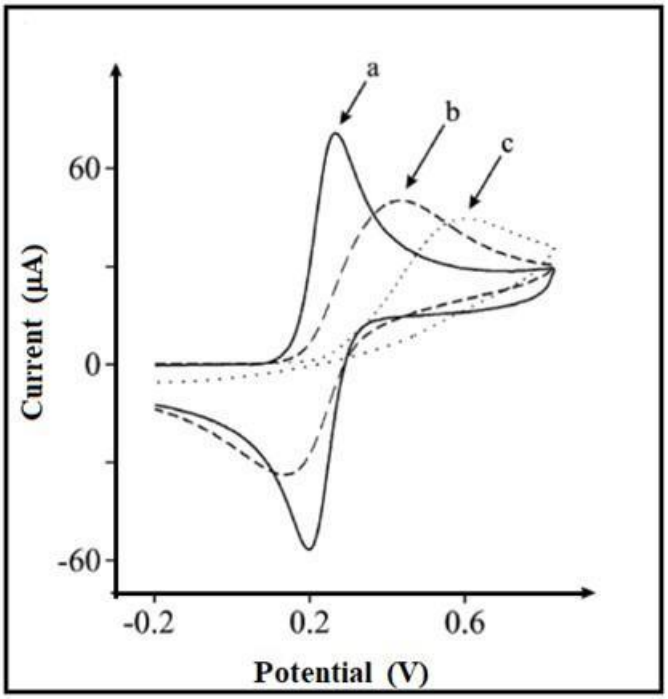


Figure 2-16 Cyclic voltammograms of a reversible, a quasi-reversible and an irreversible electron transfer system.[134]

Where E° = standard potential for a redox reaction and $E_{\frac{1}{2}}$ is the characteristic potential of a species. In cases where multi-electron processes are possible, several distinct peaks are observed for each redox couple or step.

Intercalation of Li^+ usually has anodic and cathodic peaks that are dependent on the scan rate and are therefore a quasi-reversible process. Quasi-reversible voltammograms tend not to obey Randels-Sevcik equation

and have slower electron transfer processes. Overpotential causes quasi-reversible voltammograms with peak shifts to higher potential values when scan rate is increased than reversible processes.

Irreversible systems are commonly seen with organic complexes. Their voltammograms exhibit either a single oxidation or reduction peak without the reverse current peak. In some cases, the peak potentials are widely separated and have very different shapes and sizes. These happen because the electron exchange kinetics with the working electrode are very slow and independent of the scan rate. Totally irreversible processes also show peak shift as scan rate changes; moreover, they have a peak separation higher than 0.058/*n* volts.

Cyclic voltammetry can be carried out using large surface electrodes like in batteries or using microfibre electrodes. Small electrodes have application in probes especially in biological analysis while batteries can use macro electrodes. An informative aspect of cyclic voltammetry is how ions and or electrons move during a potential sweep. They can move by diffusion, stirring and migration. Electrolyte addition in LIBs encourages movement by diffusion since there is no stirring. With intercalation compounds two separate boundaries with different conditions exist and need to be considered when describing diffusion in relation to scan rate. There is a finite diffusion process which dominates when scan rate is slow and a semi-infinite diffusion during fast scan rate. Whereas under slow scan rate the peak current is proportional to scan rate, it is proportional to the square root

of the scan rate under fast scan rate. Thus, under finite diffusion conditions the peak current can be calculated with Equation 19.

$$I_p = \frac{n^2F^2vlAC}{2RT} \qquad \text{Equation 19}$$

where *l* = distance of electrode, A = area of electrode and C = concentration of electrolyte. I_p, *n, F . R, T* and *v* as defined for Equations 17 and 18. Aoki et al [135, 136] have generalised this observation at all scan rates by Equation 20.

$$i_p = 0.44nFS\left(\frac{D}{l}\right)C\beta^{0.5}tanh\,(0.56\beta^{0.5}+0.05\beta) \qquad \text{Equation 20}$$

where β is ($nFv(l^2/D)/RT$) a dimensionless time factor parameter.

Diffusion coefficient for a single-phase diffusion-controlled kinetics without phase transitions has been estimated by plotting i_p vs, $v^{1/2}$ whose slope would be given by Equation 21 which can be rearranged to determine D.

$$\text{slope} = 0.446nFAC\left(\frac{nFD}{RT}\right)^{1/2} \qquad \text{Equation 21}$$

With Ni-rich NMC charge-discharge processes are accompanied by phase transitions, so this model would not be accurate.

In equations 17-21 the relationship of current peaks and voltage peaks with scan rate also harbours other parameters like diffusion coefficient, concentration and area of electrode and others. It is therefore not surprising that some of these internal or external battery conditions can affect the shape of the voltammogram as shown in Fig 2-17.[137] Some of these will also affect the performance of the battery like particle size of the electrode materials,[138,139] concentration of the electrolyte, operating temperature, thickness of the electrode and scan rate.

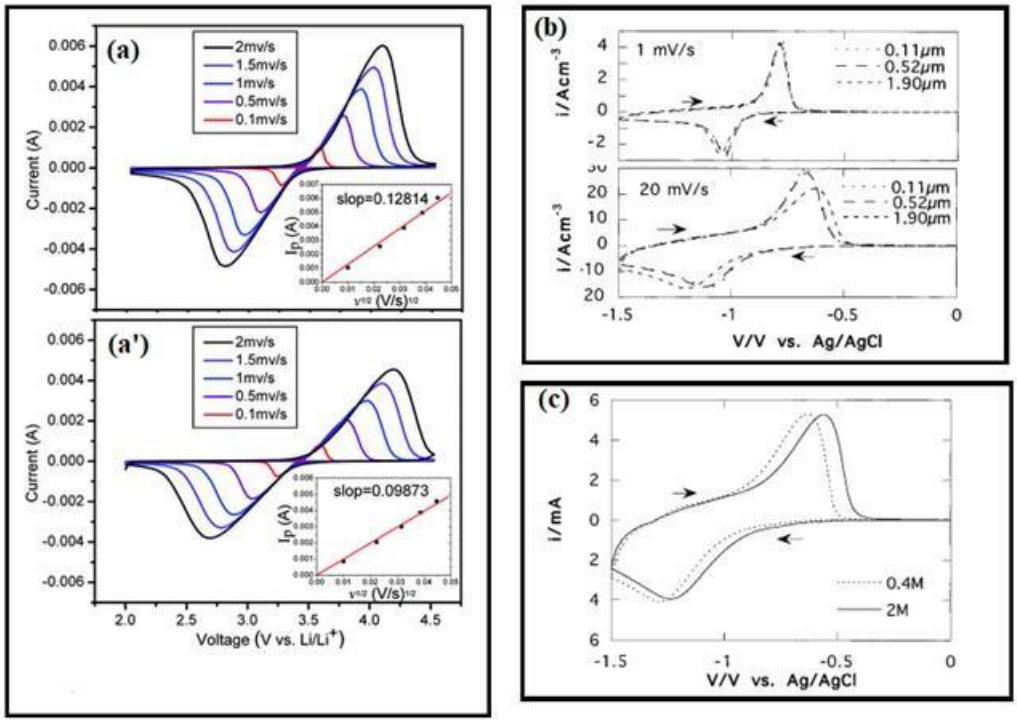


Figure 2-17. Factors affecting the shape of voltammograms of LIBs. (a) nanoparticles, (a') nanosheets and scan rate [138] (b) scan rate and electrode thickness and (c) electrolyte concentration.[139]

Smaller particles have larger surface area in contact with the electrolyte. This can result in shorter Li^+ diffusion distances which can positively affect the kinetics of the redox reactions which can lead to larger current responses even though the scan rate and other factors are the same while at the same time it can lead to more formation of the SEI which can negatively affect the performance of the battery. Although the concentration of the electrolyte does not affect Li ion diffusivity which would not affect the intensity of the peak current, it can affect the peak potential positions. According to Nernst equation, a shift towards more positive potentials can be expected as the concentration increases. This behaviour has been found to differ from one intercalation ion to another. In a diffusion-controlled

reaction, when the temperature increases the rate also increases, which results in higher current peaks because Li ions diffuse faster within the bulk material and at the electrode interface. In the case of capacitive current, a small peak split when temperature increases are a normal indication of dominance of a diffusion-controlled process on the interface, and this happens when the capacitive current is independent of the temperature. The effect of temperature on a non-Faradaic process which operates on the principle of accumulation of charge density is different in that the decrease in the splitting of the peak at elevated temperature indicates a fast electrochemical reaction. This would result in an early development of a corresponding peak potential.

CV plots can also be used to track the change occurring as repetitive cycling is done to show the effects of the formation of the SEIs.[140,141] Usually first cycles have totally different shapes of CV from the subsequent ones because of the irreversible event of SEI formation.[142] This means CV can show both the beneficial reactions for the generation of current and the side reactions that are detrimental to the optimum performance of a LIB cell. By varying scan rate studies, aspects of surface and diffusion-controlled reactions and the Li^+ diffusivity can be studied. A stepwise window analysis can even allow studies of the anionic redox processes. This is normally done by comparing a series of successive dQ/dV plots at relatively high voltage cut-off to observe where they change in profile and correlate it with the charge capacity to see how much capacity is recovered on reduction.

Sometimes cathode materials display capacitance behaviour as well. In that case, cyclic voltammetry can also be used to estimate the charge storage capacity.[143,144] This is done by comparing the anodic and cathodic peaks and integrating the area below the curves as explained by Equation 22.

$$C_{sp}(Fg^{-1}) = \int_{E_1}^{E_2} idE/2E(E_2 - E_1)mv \qquad \text{Equation 22}$$

Where C_{sp} (F g^{-1}) is specific capacitance of the half-cell electrode, *i* (A) is the current and the E_2-E_1 (V) is the potential window, the differential function of the area below the cathodic and the anodic peaks on the voltammograms is $\int_{E_1}^{E_2} i(E)dE$ and *m* is the mass of the electroactive material and *v* (V s^{-1}) is the scan rate. Within a fixed voltage window, capacitance is constant and can determine the storage charge, Equation 23.

$$\Delta Q = C \times \Delta U \qquad \text{Equation 23}$$

where △Q and △U are capacity (mAh) and voltage window (V), respectively.

2.7.2.2. Charge discharge technique.

Battery charging and discharging tests can be run as galvanostatic cycling with potential limitations (GCPL). This means restrictive current conditions can be applied within a limited potential while running in an open circuit phase. Usually the testing involves three phases, the resting period voltage, the charging and the discharging period.

Commonly plotted curves under charge discharge testing are the voltage(V) versus capacity ($mAhg^{-1}$). The plots easily follow the material performance

through repetitive charge-discharge cycles. They can show the capacity of a particular cell. Theoretically cell capacity can be calculated using Equation 24

$$C(mAhg^{-1}) = n_{\mu}F/3.6M_w \qquad \text{Equation 24}$$

Where n_{μ} is the number of electrons exchanged per cycle per mole of the cathode material and M_w is the formula weight. However, owing to experimental conditions this is often not achieved which makes it important to determine a battery's capacity. Data from such runs can give important information about the performance of the cell, the reversibility of the electrochemical reaction involved, degradation and how degradation occurs. Cell degradation or improvement can be seen when curves from different charge cycles interpolated do not completely overlap and have different capacity.[145]

There can be an initial capacity loss which is easily discernible when capacity for the first charging cycle is not efficiently reflected in the discharge cycle. This is because of irreversible reactions that happen immediately when current passes through a cell, and it can also be due to the formation of the SEI. Moreover, the charge-discharge curves easily show the extent of capacity gain associated with the activation stage of a cell which can be seen by an increase in capacity with subsequent cycling until capacity levels off. Sudden capacity loss can also easily show when a cell experiences shock followed by accelerated loss in capacity. In addition, capacity loss with aging can be seen as a gradual decrease in capacity over

several charge-discharge cycles. When conducting comparison studies, fading needs to be normalised and plotted against cycle number for easy distinct graphs even when the maximum capacities for the materials under study are different. Presence of extra small peaks can also be seen at the beginning of a charge/discharge curve as evidence of impurities. Degree of polarisation can also be estimated by looking at the voltage change at the same capacity for different cycles.

Charge/discharge data can also be used to obtain differential capacity curves which show dQ/dV plotted against V. In most cases the differential curves can show phase transition occurring at different voltages during charging or discharging. In high Ni NMC the transitions are from H1(hexagonal) to monoclinic phase (M) and then further hexagonal phases, H2 and H3, which occur as Li^+ is lost and lattice parameters change.[146] The conversion of the latter hexagonal phases has been associated with the largest volume changes.[66,147] It is through the differential capacity plots that it can also be seen how operating at high voltage cut-offs leads to irreversible degradation. Some researchers plot dQ/dV versus Q curves from which much the same information of where phase transitions occur is obtained.[148] The charge discharge tests can also help determine the C rating which is, the performance of a battery in relation to the current at which it is charged and discharged. A 1C rate (1C current) means a battery

that delivers 1 Ah capacity when fully charged should be able to provide 1 A for 1 hour.

In plots dQ/dV curves may seem similar because they are based on a common principle, but they are not equivalent. Cyclic voltammetry has information of rate, *v,* information that is totally lacking in differential charge plots. One can convert CV curves to dQ/dV plots by using the following conversions.

$$V = vt$$

$$dt = dV/v$$

$$I = dQ/dt$$

Thus $I/v = dQ/dV$

where v (Vs^{-1}) is the scan rate, V (V) is the voltage, I (A) is current, Q (h A) is charge and t (s) is time. However, obtained in this manner the information is obtained under different experimental conditions in that when running GCPL, the current is kept constant throughout the acquisition whereas for CV, current will change when the electrochemical reaction gives enough energy to drive the reaction while the potential increases linearly with time.

2.7.2.3. Electrochemical impedance spectroscopy studies

Electrochemical impedance spectroscopy (EIS) is a measure of the opposition to current flow through internal batteries. EIS is a non-destructive technique that can affect the performance of a battery in terms of its operating voltage, its efficiency and its rate capability. A battery has many components like the electrodes such as the electrolyte, separators, the

current collectors and conducting metal contacts which all contribute either resistive, capacitive or inductive impedance. To measure the impedance of an electrochemical cell can be done by two modes, the galvanostatic mode (GEIS) and the potentiostatic mode (PEIS) for current and voltage excitation, respectively. Measurement is done while a cell is being excited by a sinusoidal wave potential or current of a certain amplitude over a range of frequencies and a sinusoid AC current response is measured. The range of frequencies allow for a generation of an impedance spectrum. The spectrum can be presented as a Nyquist plot Figure 2-18, which plots the imaginary part of the impedance against the real part. Generally, for LIBs the Nyquist plot is best done by equivalent circuit modelling in which parameters of a physical electrical circuit to represent the physical and chemical processes of a battery.[149]

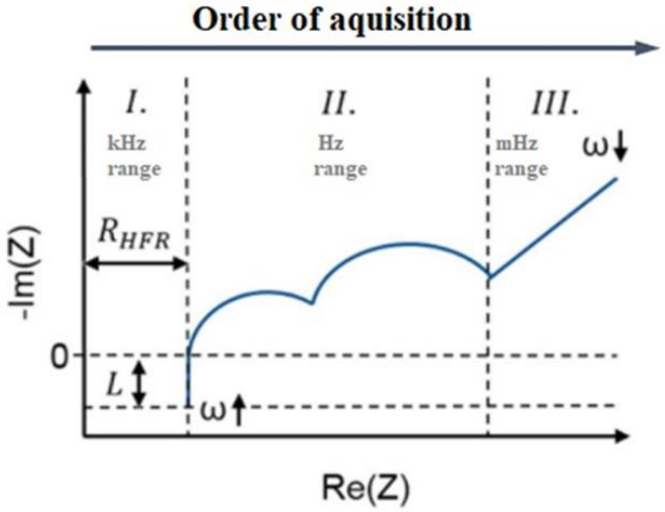


Figure 2-18 The schematic representation of a Nyquist plot typical for a LIB battery.

Figure 2-18 shows three parts, I, II and III, [143,150] of the impedance curves which is interpreted as follows:

- Part I This section is the high frequency section which normally represents the fast mass transfer phase. This section represents Li^+ diffusion within the electrolyte and results in electrolyte resistance so it is normally added as a resistor on the equivalent circuit. The part marked as L represents the electronic conduction in the metal components of a cell and it is also an Ohmic resistance element.
- Part II is the mid-section representing the mid frequency area. It is characterised by two semi-circles, which appear depressed because of the unevenness of the surfaces. The lower normally smaller semi-circle represents the ion migration through the surface layer, the SEI layer. The larger semi-circle is the charge transfer impedance between the electrolyte and the surface of the electrodes, and it is a double layer solid-liquid interphase. This second semi-circle indicates the state of health (SOH) of the battery, which increases in diameter as the battery goes through repetitive cycling and ages; also, the CEI layer thickens thus increasing the radius of the first semi-circle as well. However, modification of the active material by coating with the right coats, can reduce the impact of aging on these components.[151]
- Part III is the low frequency acquisition area which appears as a tail and an angle, referred to as Warburg impedance. It represents the slower mass transfer processes that occur due to Li^+ diffusion

through the solid active material and electrolyte pores in the corridors that are observed at very low perturbation frequencies. Diffusion occurs as a result of concentration gradient and as such it tends to fade off when the gradient gets less and as such represents the capacitive component of the battery.

Other than in batteries, EIS has uses in corrosion studies, fuel cell studies, and sensors where it provides parameters on corrosion rates, electrode surfaces porosity, coating, mass transport, and interfacial capacitance measurements.

Other tests that can be done to battery material are thermal stability test which can be done using differential scanning calorimetry (DSC), Fourier transformed infrared spectroscopy (FTIR) and Raman spectroscopy which can be used to identify impurities on the surface of the materials. In DSC studies heat flow from the material is measured to establish its heat stability. The peaks will show at a temperature at which a particular exothermic reaction occurs, and they can be integrated to show the amount of heat per each exothermic process. Some endothermic processes like decomposition of Li may also be seen. Combining DSC with thermal gravimetry (TG) can help record mass change during heating which will indicate the decomposition reactions. These however are more obvious in a case where the measurements are done on material in the electrolyte where reactions that can be due to a loss of oxygen or adsorbed impurities are easily seen. Raman spectroscopy can be used to show the vibrational modes of bonds in molecules. In NMC, the peaks of the band shift due to A_{1g} and E_g of the

transition metals Ni, Mn and Co can be identified using Raman spectra. In certain cases, it may be possible to see the contaminants and impurities as they will also produce their signal.

In summary, Ni-rich NMC remains as one of the most promising cathode materials for energy intensive application however, it is still riddled with all sorts of degradation pathways that do not allow it to reach its potential. As a way towards combating one of the degradation problems of NMC, coating was applied. The qualities of a good cathode were listed earlier in Section 2.3. and in addition, it has been discussed what the shortcomings of NMC811 are and how coating and doping have helped improve the electrochemical performance of cathode materials for LIBs. With these in mind, we are led to the aim of this work. The target of this work was to use Ce as a dopant and its oxide as a coating for NMC811.

This was done through first running preliminary studies with NMC622 by coating and then analysing the nature of the coating in order to optimise how to coat with CeO_2. This work was followed with synthesis NMC811 which was either coated with CeO_2 or doped Ce.

Moreover, synthetic routes that used microwave irradiation were applied and compared with a route in which irradiation was not utilised. The other variation

to the general coprecipitation method was to use conventional stirring versus laminar flow stirring to prepare the cathode material.

The effect of the modifications was determined by studying the difference in structural, chemical and electrochemical performance of the modified material versus the pristine material.

2.8. Aim of the thesis

The aim of this work is to study the electrochemical performance of $LiNi_{0.6}Mn_{0.2}Co_{0.2}O_2$ (NMC622) that has been coated with CeO_2 , and to interrogate the effects of microwave-assisted surface-coating and doping with a little amount of CeO_2 on the electrochemical performance of $LiNi_{0.8}Mn_{0.1}Co_{0.1}O_2$ (NMC811).

These were achieved by the following objectives:

1. To synthesise CeO_2 coated NMC622 from commercial NMC622
2. To investigate the effect of synthesising NMC811, CeO_2 coated NMC811 and Ce doped NMC811 using the conventional lab method and a laminar flow reactor.
3. To subject the synthesised materials to microwave irradiation.
4. To investigate the physicochemical characterization of the synthesised materials using PXRD, Raman, TGA, SEM, TEM and HRTEM.
5. To Fabricate coin cells using the materials and apply them as cathode material.
6. To Investigate the electrochemical performance of Ni-rich NMC NMC622 and NMC 811 using coin type Li-ion cells.

REFERENCES

1. The history and development of batteries https://phys.org/news/2015-04-history-batteries.html
2. Mizushima, K.J.P.C., Jones, P.C., Wiseman, P.J. and Goodenough, J.B., 1980. Li_xCoO_2 (0< x<-1): A new cathode material for batteries of high energy density. *Materials Research Bulletin*, *15*(6), pp.783-789.
3. Ozawa, K., 1994. Lithium-ion rechargeable batteries with $LiCoO_2$ and carbon electrodes: the $LiCoO_2$/C system. *Solid State Ionics*, *69*(3-4), pp.212-221.
4. Nagaura, T.; Tozawa, K., 1990. Progress in batteries solar cells, *JEC Press*, 9, 209.
5. Zhou, D., Shanmukaraj, D., Tkacheva, A., Armand, M. and Wang, G., 2019. Polymer electrolytes for lithium-based batteries: advances and prospects. *Chem*, *5*(9), pp.2326-2352.
6. Nitta, N., Wu, F., Lee, J.T. and Yushin, G., 2015. Li-ion battery materials: present and future. *Mat. Today*, *18* (5), , pp.252-264
7. Battery showdown: Lead-acid-vs lithium-ion https://medium.com/solar-microgrid/battery-showdown-lead-acid-vs-lithium-ion-1d37a1998287
8. Soloveichik, G. L., 2011. Battery Technologies for Large-Scale Stationary Energy Storage, *Annu. Rev. Chem. Biomol*. *Eng. 2*, pp. 503-527.
9. Kim T.H., Park J.S., Chang S.K., Choi S., Ryu J.H., Song H.K., 2012. The current move of lithium-ion batteries towards the next phase. *Adv, Energy Mater.*, *2*(7), 860-72.
10. Armand, M., Tarascon, J.M., 2008. Building better batteries. *Nature*, *451*(7179), pp. 652-657.
11. Li, W., Liu, X., Celio, H., Smith, P., Dolocan, A., Chi, M., Manthiram, A., 2018. Mn versus Al in Layered Oxide Cathodes in Lithium-Ion Batteries: A Reviving on Long-Term Cyclability. *Adv, Energy Mater., 8*(15), 1703154.
12. Thackeray, M.M., Kang, S.H., Johnson, C.S., Vaughey, J.T., Benedek, R., Hackney, S.A., 2007. Li_2MnO_3-stabilized $LiMO_2$ (M= Mn, Ni, Co) electrodes for lithium-ion batteries. *J. Mater. Chem.*, *17*(30), pp. 3112-3125.
13. Jung R, Metzger M, Maglia F, Stinner C, Gasteiger HA., 2017 Oxygen release and its effect on the cycling stability of $LiNi_xMn_yCo_zO_2$ (NMC) cathode materials for Li-ion batteries. *J. Electrochem. Soc., 164*(7), A1361-77.
14. Christensen, J., Albertus, P., Sanchez-Carrera, R.S., Lohmann, T, Kozinsky, B., Liedtke, R., Ahmed, J., Kojic, A., 2011. A critical review of Li/air batteries. *J. Electrochem. Soc*., *159*(2), R1-30.
15. Mohanty, D., Dahlberg, K., King, D.M., David, L.A., Sefat, A.S., Wood, D.L., Daniel, C., Dhar S, Mahajan V, Lee M, Albano F.,2016. Modification of Ni-rich FCG NMC and NCA cathodes by atomic layer

deposition: Preventing surface phase transitions for high-voltage lithium-ion batteries. *Sci. Rep*, *6*, 26532.
16. Lu, Y., Tu, Z., Archer, L. A., 2014. Stable lithium electrodeposition in liquid and nanoporous solid electrolytes. *Nature materials*, *13* (10), pp. 961-969.
17. Whittingham, M. S., 2004. Lithium Batteries and Cathode Materials. *Chem. Rev. 104*, pp. 4271-4302.
18. Gamble, F. R., Thompson, A. H., 1978. Superconductivity in layer compounds intercalated with paramagnetic molecules, *Solid State Commun*., *27*, 379-382
19. Whittingham, M.S., 1976. Electrical energy storage and intercalation chemistry. *Science*, *192* (4244), pp. 1126-1127.
20. Whittingham, M.S., 2020. Lithium batteries: 50 years of advances to address the next 20 years of climate issues. *Nano Lett., 20*(12)*,* pp. 8435-8437
21. Whittingham, M. S., Chianelli, R. R., 1980. Layered compounds and intercalation chemistry, *J. Chem. Educ*., *57*, pp. 569-574.
22. Burrard-Lucas, M., Free, D.G., Sedlmaier, S.J., Wright, J.D., Cassidy, S.J., Hara, Y., Corkett, A.J., Lancaster, T., Baker, P.J., Blundell, S.J. and Clarke, S.J., 2013. Enhancement of the superconducting transition temperature of FeSe by intercalation of a molecular spacer layer. *Nature materials*, *12*(1), pp.15-19.
23. Manthiram, A.,2020. A reflection on lithium-ion battery cathode chemistry. *Nat. Commun*, *11* (1), pp.1-9.
24. Berlinsky, A.J., Unruh, W.G., McKinnon, W.R. and Haering, R.R.,1979. Theory of lithium ordering in Li_xTiS_2. *Solid State Commun.*, *31*(3), pp.135-138.
25. Li, W., Dahn, J.R., Wainwright, D.S., 1994. Rechargeable lithium batteries with aqueous electrolytes. *Science*, *264*(5162), pp.1115-1118.
26. Thackery, M.M., David, W.I.F., Bruce, P.G., Goodenough, J.B.,1983. Lithium insertion into manganese spinels, *Mater. Res. Bull.*, *18*(4) p. 461-472.
27. Manthiram, A. and Goodenough, J.B., 1987. Lithium insertion into $Fe_2(MO_4)_3$ frameworks: comparison of M= W with M= Mo. *J. Solid State Chem., 71*(2), , pp.349-360.
28. Manthiram, A. and Goodenough, J.B., 1989. Lithium insertion into $Fe_2(SO_4)_3$ frameworks. *J. Power Sources*, *26*(3-4) , 403-408.
29. Tripathi, R., Ramesh, T.N., Ellis, B.L. and Nazar, L.F., 2010. Scalable synthesis of tavorite $LiFeSO_4F$ and $NaFeSO_4F$ cathode materials. *Angew. Chem.*, *122*(46), pp.8920-8924.
30. Marx, N., Croguennec, L., Carlier, D., Wattiaux, A., Le Cras, F., Suard, E. and Delmas, C., 2010. The structure of tavorite $LiFePO_4(OH)$ from diffraction and GGA+ U studies and its preliminary electrochemical characterization. *Dalton Trans.*,*39*(21), pp.5108-5116.

31. Julien, C.M., Mauger, A., Zaghib, K. and Groult, H., 2014. Comparative issues of cathode materials for Li-ion batteries. *Inorganics*, *2*(1), pp.132-154.
32. Liu, T., Dai, A., Lu, J., Yuan, Y., Xiao, Y., Yu, L., Li, M., Gim, J., Ma, L., Liu, J. and Zhan, C., 2019. Correlation between manganese dissolution and dynamic phase stability in spinel-based lithium-ion battery. *Nat. Commun*, *10*(1), pp.1-11.
33. https://www.tycorun.com/blogs/news/what-is-the-high-temperature-study-of-spinel-limn2o4
34. Thackeray, M.M. and Amine, K., 2021. $LiMn_2O_4$ spinel and substituted cathodes. *Nat. Energy*,*6* (5), pp.566-566.
35. Gabrielli, G., Marinaro, M., Mancini, M., Axmann, P. and Wohlfahrt-Mehrens, M., 2017. A new approach for compensating the irreversible capacity loss of high-energy Si/C | $LiNi_{0.5}Mn_{1.5}O_4$ lithium-ion batteries. *J. Power Sources*,*351*, pp.35-44.
36. Choi, N.S., Han, J.G., Ha, S.Y., Park, I. and Back, C.K., 2015. Recent advances in the electrolytes for interfacial stability of high-voltage cathodes in lithium-ion batteries. *RCS Adv.*, *5*(4), pp.2732-2748.
37. Zheng, F., Kotobuki, M., Song, S., Lai, M.O. and Lu, L., 2018. Review on solid electrolytes for all-solid-state lithium-ion batteries. *J. Power Sources*, *389*, pp.198-213.
38. Schmidt, M., Heider, U., Kuehner, A., Oesten, R., Jungnitz, M., Ignat'Ev, N. and Sartori, P., 2001. Lithium fluoroalkylphosphates: a new class of conducting salts for electrolytes for high energy lithium-ion batteries. *J. Power Sources*, *97*, pp.557-560.
39. Suo, L., Hu, Y.S., Li, H., Armand, M. and Chen, L., 2013. A new class of solvent-in-salt electrolyte for high-energy rechargeable metallic lithium batteries. *Nat. Commun.*, *4*(1), pp.1-9.
40. Brutti, S., Simonetti, E., De Francesco, M., Sarra, A., Paolone, A., Palumbo, O., Fantini, S., Lin, R., Falgayrat, A., Choi, H. and Kuenzel, M., 2020. Ionic liquid electrolytes for high-voltage, lithium-ion batteries. *J. Power Sources*, *479*, p.228791.
41. Haruna, A.B., Mwonga, P., Barrett, D., Rodella, C.B., Forbes, R.P., Venter, A., Sentsho, Z., Fletcher, P.J., Marken, F. and Ozoemena, K.I., 2021. Defect-Engineered β-$MnO_{2-\delta}$ Precursors Control the Structure–Property Relationships in High-Voltage Spinel $LiMn_{1.5}Ni_{0.5}O_{4-\delta}$. *ACS Omega, 6*(39), pp. 25562-25573.
42. Armand, M., Gauthier, M., Magnan, J.F. and Ravet, N., 2009. Universite de Montreal, Hydro Quebec Corp and Centre National de la Recherche Scientifique CNRS, *Method for synthesis of carbon-coated redox materials with controlled size*. U.S. Patent 7601318B2.
43. Chung S-Y, Bloking JT, Chiang Y-M., 2002. Electronically conductive phosphor-olivines as lithium storage electrode. *Nat. Mater.*, *1*, pp.123-128
44. Ling, J., Karuppiah, C., Krishnan, S.G., Reddy, M.V., Misnon, I.I., Ab Rahim, M.H., Yang, C.C. and Jose, R., 2021. Phosphate polyanion materials as high-voltage lithium-ion battery cathode: a review. *Energy Fuels*, *35*(13), pp.10428-10450.

45. Nishizawa, M. and Yamamura, S., 1998. Irreversible conductivity change of $Li_{1-x}CoO_2$ on electrochemical lithium insertion/extraction, desirable for battery applications. *ChemComm.*, *16*, pp.1631-1632.
46. Chebiam, R.V., Prado, F. and Manthiram, A., 2001. Soft Chemistry Synthesis and Characterization of Layered $Li_{1-x}Ni_{1-y}Co_yO_{2-\delta}$ ($0 \leq x \leq 1$ and $0 \leq y \leq 1$). *Chem. Mater.*, *13*(9), pp.2951-2957.
47. Doughty D, Rother E.P., 2012. A general discussion of Li-ion battery safety, *Electrochem, Soc. Interface, 21*(2), 37-44. Meng, L., Wang, G., See, K.W., Wang, Y., Zhang, Y., Zang, C., Zhou, R. and Xie, B., 2022. Large-scale Li-ion battery research and application in mining industry. *Energies*, *15*(11), p.3884.
48. Meng, L., Wang, G., See, K.W., Wang, Y., Zhang, Y., Zang, C., Zhou, R. and Xie, B., 2022. Large-scale Li-ion battery research and application in mining industry. *Energies*, *15*(11), p.3884.
49. Sun, H. and Zhao, K., 2017. Electronic structure and comparative properties of LiNi x Mn y Co z O2 cathode materials. *J. Phys. Chem. C.*, *121*(11), pp.6002-6010.
50. https://www.cfr.org/blog/why-cobalt-mining-drc-needs-urgent-attention
51. Calvão, F., Mcdonald, C.E.A. and Bolay, M., 2021. Cobalt mining and the corporate outsourcing of responsibility in the Democratic Republic of Congo. *Extr Ind Soc*, *8*(4), p.100884.
52. Li, J., Camardese, J., Glazier, S., Dahn, J.R., 2014. Structural and electrochemical study of the Li–Mn–Ni oxide system within the layered single phase region. *Chem. Mater. 26*(24), pp.7059-66.
53. Garcia, J.C., Bareño, J., Yan, J., Chen, G., Hauser, A., Croy, J.R., Iddir, H., 2017. Surface structure, morphology, and stability of Li $(Ni_{1/3}Mn_{1/3}Co_{1/3})$ O_2 cathode material. *J. Phys. Chem. C.*, *121*(15), pp 8290-8299.
54. https://batteryuniversity.com/article/bu-205-types-of-lithium-ion
55. Kim, U. H., Kuo, L.Y., Kaghazchi, P., Yoon, C.S., Sun, Y. K., 2019. Quaternary Layered Ni-Rich NCMA Cathode for Lithium-Ion Batteries. *ACS Energy Lett*. *4*(2), 576-582.
56. Yoon, W.S., Chung, K.Y., McBreen, J. and Yang, X.Q., 2006. A comparative study on structural changes of $LiCo_{1/3}Ni_{1/3}Mn_{1/3}O_2$ and $LiNi_{0.8}Co_{0.15}Al_{0.05}O_2$ during first charge using in situ XRD. *Electrochem. Commun*, *8*(8), pp.1257-1262.
57. Kerlau, M., Marcinek, M., Srinivasan, V. and Kostecki, R.M., 2007. Reprint of “Studies of local degradation phenomena in composite cathodes for lithium-ion batteries”. *Electrochim. Acta*, *53*(3), pp.1385-1392.
58. Abraham, D.P., Reynolds, E.M., Sammann, E., Jansen, A.N. and Dees, D.W., 2005. Aging characteristics of high-power lithium-ion cells with $LiNi_{0.8}Co_{0.15}Al_{0.05}O_2$ and $Li_{4/3}Ti_{5/3}O_4$ electrodes. *Electrochim. Acta*, *51*(3), pp.502-510.
59. Yoon, W.S., Grey, C.P., Balasubramanian, M., Yang, X.Q. and McBreen, J., 2003. In situ X-ray absorption spectroscopic study on

$LiNi_{0.5}Mn_{0.5}O_2$ cathode material during electrochemical cycling. *Chem. Mater.*, *15*(16), pp.3161-3169.
60. Shizuka K, Kobayashi T, Okahara K, Okamoto K, Kanzaki S, Kanno R.,2005. Characterization of $Li_{1+y}Ni_xCo_{1-2x}Mn_xO_2$ positive active materials for lithium-ion batteries. *J. Power Sources*., *146*(1-2), 589-93.
61. Ohzuku, T., Makimura, Y., 2001. Layered lithium insertion material of $LiCo_{1/3}Ni_{1/3}Mn_{1/3}O_2$ for lithium-ion batteries. *Chem. Lett.*, *30* (7), pp. 642-643
62. Todorov, Y. M., Hideshima, Y., Noguchi, H., Yoshio, M., 1999. Determination of theoretical capacity of metal ion-doped LiMn2O4 as the positive electrode in Li-ion batteries. *J. Power Sources*. *77*(2), pp. 198-201.
63. Zhu, L., Liu, Y., Wu, W., Wu, X., Tang, W., Wu, Y., 2015. Surface fluorinated $LiNi_{0.8}Co_{0.15}Al_{0.05}O_2$ as a positive electrode material for lithium-ion batteries. *J. Mater. Chem. A*., *3*(29), pp. 15156-15162.
64. Çetin, B., Camtakan, Z. and Yuca, N., 2020. Synthesis and characterization of li-rich cathode material for lithium-ion batteries. *Mater. Lett.*, , p.127927.
65. Thackeray, M.M., Johnson, C.S., Vaughey, J.T., Li N., Hackney, S.A.,2005. Advances in manganese-oxide 'composite' electrodes for lithium-ion batteries, *J. Mater. Chem*., *15,* pp. 2257–2267
66. Noh, H.J., Youn, S., Yoon, C.S., Sun, Y.K, 2013. Comparison of the structural and electrochemical properties of layered $Li(Ni_xCo_yMn_z)O_2$ (x= 1/3, 0.5, 0.6, 0.7, 0.8 and 0.85) cathode material for lithium-ion batteries. *J. Power Sources*, *233*, pp.121-30.
67. Amine, K., 2012. Next generation batteries to enable expansion of vehicle electrification, *Electrochemistry*, **80** (10), 2012, p. 694.
68. Olivetti, E.A., Ceder, G., Gaustad, G.G., Fu, X., 2017. Lithium-ion battery supply chain considerations: analysis of potential bottlenecks in critical metals, *Joule*, *1*(2), pp. 229-43.
69. Jung, S.K., Gwon, H., Hong, J., Park, K.Y., Seo, D.H., Kim, H., Hyun, J., Yang, W., Kang, K., 2014. Understanding the degradation mechanisms of $LiNi_{0.5}Co_{0.2}Mn_{0.3}O_2$ cathode material in lithium-ion batteries. *Adv. Energy Mater.*, *4*(1), 1300787.
70. Liang L, Sun X, Wu C, Hou L, Sun J, Zhang X, Yuan C., 2018. Nasicon-type surface functional modification in core–shell $LiNi_{0.5}Mn_{0.3}Co_{0.2}O_2$@$NaTi_2(PO_4)_3$ cathode enhances its high-voltage cycling stability and rate capacity toward Li-Ion batteries. *ACS Appl. Mater. Interfaces*, *10*(6), pp. 5498-5510.
71. NMC Powder (LiNiMnCoO2) https://www.targray.com/li-ion-battery/cathode-materials/nmc accessed
72. Lu, H., Zhou, H., Svensson, A.M., Fossdal, A., Sheridan, E., Lu, S. and Vullum-Bruer, F., 2013. High capacity Li $(Ni_{0.8}Co_{0.1}Mn_{0.1})O_2$ synthesized by sol–gel and co-precipitation methods as cathode materials for lithium-ion batteries. *Solid State Ion.*, *249*, pp.105-111.
73. Dahbi, M., Wikberg, J.M., Saadoune, I., Gustafsson, T., Svedlindh, P. and Edström, K., 2012. Electrochemical behavior of

$LiNi_{1-y-z}Co_yMn_zO_2$ probed through structural and magnetic properties. *J. of Appl. Phys.*, *111*(2), p.023904.
74. Zhang, W., Hanxing, L.I.U., Chen, H.U., Xianjun, Z.H.U. and Yanxi, L.I., 2008. Preparation of layered oxide $Li(Co_{1/3}Ni_{1/3}Mn_{1/3})O_2$ via the sol-gel process. *Rare Metals*, *27*(2), pp.158-164.
75. Leifer, N., Penki, T., Nanda, R., Grinblat, J., Luski, S., Aurbach, D. and Goobes, G., 2020. Linking structure to performance of $Li_{1.2}Mn_{0.54}Ni_{0.13}Co_{0.13}O_2$ (Li and Mn rich NMC) cathode materials synthesized by different methods. *Phys. Chem.*, *22*(16), pp.9098-9109.
76. Liu, A., Dahn, J. R., 2019. The formation of layered double hydroxide phases in the coprecipitation syntheses of $[Ni_{0.80}Co_{0.15}]_{(1-x)/0.95}Al_x(OH)_2$ $(anion^{n-})_{x/n}$ (x= 0–0.2, n= 1, 2). *Chem. Eng.*, *3*(2), p.38.
77. Li, H., Li, J., Ma, X. and Dahn, J.R., 2018. Synthesis of single crystal $LiNi_{0.6}Mn_{0.2}Co_{0.2}O_2$ with enhanced electrochemical performance for lithium-ion batteries. *J. Electrochem. Soc.*, *165*(5), p.A1038.
78. Lee, M. H., Kang, Y. J., Myung, S. T., & Sun, Y. K. (2004). Synthetic optimization of $Li[Ni_{1/3}Co_{1/3}Mn_{1/3}]O_2$ via co-precipitation. *Electrochim. Acta*, *50*(4), pp. 939-948.
79. Kim, J., Lee H., Cha, H., Yoon, M., Park, M., Cho, J., 2018. Prospect and Reality of Ni-Rich Cathode for Commercialization. *Adv. Energy Mater*., *8*(6), pp. 1702028.
80. Zeng, X., Zhan, C., Lu, J., Amine, K., 2018. Stabilization of a high-capacity and high-power nickel-based cathode for Li-ion batteries. *Chem*, *4*(4), pp. 690-704.
81. Cho, D.H., Jo, C.H., Cho, W., Kim, Y.J., Yashiro, H., Sun, Y.K., Myung, S.T., 2014. Effect of residual lithium compounds on layer Ni-rich $Li(Ni_{0.7}Mn_{0.3})O_2$. *J. Electrochem. Soc.*, *161*(6), 2014, A920-6.
82. Li, J., Downie, L.E., Ma, L., Qiu, W. and Dahn, J.R.,2015. Study of the failure mechanisms of $LiNi_{0.8}Mn_{0.1}Co_{0.1}O_2$ cathode material for lithium-ion batteries. *J. Electrochem. Soc.*, *162*(7), p.A1401.2
83. Kim, Y., 2013. Mechanism of gas evolution from the cathode of lithium-ion batteries at the initial stage of high-temperature storage. *J. Mater. Sci.*, *48*(24), pp.8547-8551.
84. Solchenbach, S., Metzger, M., Egawa, M., Beyer, H. and Gasteiger, H.A., 2018. Quantification of PF5 and POF3 from side reactions of LiPF6 in Li-ion batteries. *J. Electrochem. Soc.*, *165*(13), p.A3022.
85. Aurbach, D., Ein-Eli, Y., Markovsky, B., Zaban, A., Luski, S., Carmeli, Y., Yamin, H., 1995. The study of electrolyte solutions based on ethylene and diethyl carbonates for rechargeable Li batteries II. Graphite electrodes. *J. Electrochem. Soc.*, *142*(9), 2882-90.
86. Aurbach, D., Moshkovich, M., 1998. A Study of Lithium Deposition-Dissolution Processes in a Few Selected Electrolyte Solutions by Electrochemical Quartz Crystal Microbalance. *J. Electrochem. Soc., 145*(8), 2629-39.

87. Zhao, X., Zhuang, Q.C., Wu, C., Wu, K., Xu, J.M., Zhang, M.Y., Sun, X.L., 2015. Impedance studies on the capacity fading mechanism of

$Li(Ni_{0.5}Co_{0.2}Mn_{0.3})O_2$ cathode with high-voltage and high-temperature. *J. Electrochem. Soc.*, *162*(14), A2770-9.
88. Berkesm, B.B., Schiele, A., Sommer, H., Brezesinski, T., Janek, J., 2016. On the gassing behavior of lithium-ion batteries with NCM5 23 cathodes. J*. Solid State Electrochem*., *20*(11), pp. 2961-2967.
89. Li, C.C., Lee, J.T., Tung, Y.L., Yang, C.R., 2007. Effects of pH on the dispersion and cell performance of $LiCoO_2$ cathodes based on the aqueous process. *J. Mater. Sci.*, *42*(14), 5773, pp. 5777.
90. Loeffler, N., Kim, G.T., Mueller, F., Diemant, T., Kim, J.K., Behm, R.J., Passerini, S., 2016. In situ coating of $Li(Ni_{0.33}Mn_{0.33}Co_{0.33})O_2$ particles to enable aqueous electrode processing. *ChemSusChem*, *9*(10), pp. 1112-7.
91. Bang, H.J.; Joachin, H.; Yang, H.; Amine, K.; Prakash, J., 2006. Contribution of the structural changes of $LiNi_{0.8}Co_{0.15}Al_{0.05}O_2$ cathodes on the exothermic reactions in Li-ion cells. *J. Electrochem. Soc.*, *153*, A731–A737
92. Self, J., Aiken, C.P., Petibon, R., Dahn, J.R., 2015. Survey of gas expansion in Li-ion pouch cells. *J. Electrochem. Soc.*, *162*(6), A796-802.
93. Bak S.M., Hu E, Zhou Y, Yu X, Senanayake SD, Cho SJ, Kim KB, Chung KY, Yang XQ, Nam KW., 2014. Structural changes and thermal stability of charged $LiNi_xMn_yCo_zO_2$ cathode materials studied by combined in situ time-resolved XRD and mass spectroscopy. *ACS Appl. Mater. Interfaces*. *6*(24), pp. 22594-22601.
94. Börner M., Horsthemke F., Kollmer F., Haseloff S., Friesen A., Niehoff P., Nowak S., Winter M., 2016. Schappacher FM. Degradation effects on the surface of commercial $LiNi_{0.5}Co_{0.2}Mn_{0.3}O_2$ electrodes. *J. Power Sources*, *335*, pp. 45-55.
95. Bak, S.M., Nam, K.W., Chang, W., Yu, X., Hu, E., Hwang, S., Stach, E.A., Kim, K.B., Chung, K.Y., Yang, X.Q., 2013. Correlating Structural Changes and Gas Evolution during the Thermal Decomposition of Charged $Li_xNi_{0.8}Co_{0.15}Al_{0.05}O_2$ Cathode Materials. *Chem. Mater*, *25* (3), pp. 337-351.
96. Rossen, E., Jones, C.D., Dahn, J.R., 1992. Structure and electrochemistry of $Li_xMn_yNi_{(1-y)}O_2$, *Solid State Ion.*, *57*(3/4), pp. 311-318
97. Wu, Z., Ji, S., Liu, T., Duan, Y., Xiao, S., Lin, Y., Xu, K., Pan, F., 2016. Aligned Li^+ Tunnels in Core-Shell $Li(Ni_xMn_yCo_z)O_2$@ $LiFePO_4$ Enhances Its High Voltage Cycling Stability as Li-ion Battery Cathode. *Nano Lett.*, *16*, pp. 6357−6363.
98. Kang, S.H., Thackeray, M.M. 2008 Stabilization of $xLi_2MnO_3 \cdot (1-x)LiMO_2$ electrode surfaces (M= Mn, Ni, Co) with mildly acidic, fluorinated solutions. *J. Electrochem. Soc.*, *155* (4), pp. A269-275
99. Sun, H.H., Ryu, H.H., Kim, U.H., Weeks, J.A., Heller, A., Sun, Y.K. and Mullins, C.B., 2020. Beyond doping and coating: prospective strategies for stable high-capacity layered Ni-rich cathodes. *ACS Energy Lett.*, *5*(4), pp.1136-1146.

100. Ishidzu, K., Oka, Y., Nakamura, T.,2016. Lattice volume change during charge/discharge reaction and cycle performance of Li ($Ni_xCo_yMn_z$)O_2. *Solid State Ionics; 288*, pp. 176-179.
101. Kondrakov AO, Schmidt A, Xu J, Geßwein H, Mönig R, Hartmann P, Sommer H, Brezesinski T, Janek J., 2017. Anisotropic lattice strain and mechanical degradation of high-and low-nickel NCM cathode materials for Li-ion batteries. *J. Phys. Chem. C*., *121* (6), pp. 3286-3294.
102. Liu, H., Wolf, M., Karki, K., Yu, Y.S., Stach, E.A., Cabana, J., Chapman, K.W., Chupas, P.J., 2017. Intergranular cracking as a major cause of long-term capacity fading of layered cathodes. *Nano Lett*. *17*(6), pp. 3452-3457.
103. Li W, Asl HY, Xie Q, Manthiram A. Collapse of LiNi1–x–y Co x Mn y O2 Lattice at Deep Charge Irrespective of Nickel Content in Lithium-Ion Batteries. *J. Am. Chem. Soc*., *141*(13), 2019, pp. 5097-5101.
104. Li, T., Yuan, X.Z., Zhang, L., Song, D., Shi, K., Bock, C., 2020. Degradation mechanisms and mitigation strategies of nickel-rich NMC-based lithium-ion batteries. *Electrochem. Energy Rev.*, *3*(1), pp.43-80.
105. Shishvan, S.S., Fleck, N.A., McMeeking, R.M. and Deshpande, V.S., 2023. Cracking and associated volumetric expansion of NMC811 secondary particles. *J. Power Sources*, *588*, p.233745.
106. Krause, T., Nusko, D., Pitta Bauermann, L., Vetter, M., Schäfer, M. and Holly, C., 2024. Methods for Quantifying Expansion in Lithium-Ion Battery Cells Resulting from Cycling: A Review. *Energies*, *17*(7), p.1566.
107. Xiong X, Wang Z, Yue P, Guo H, Wu F, Wang J, Li X., 2013. Washing effects on electrochemical performance and storage characteristics of $LiNi_{0.8}Co_{0.1}Mn_{0.1}O_2$ as cathode material for lithium-ion batteries. J*. Power Sources, 222*. pp. 318-325.
108. Reddy, M.V., Jie, T.W., Jafta, C.J., Ozoemena, K.I., Mathe, M.K., Nair, A.S., Peng, S.S., Idris, M.S., Balakrishna, G., Ezema, F.I. and Chowdari, B. V. R.,2014. Studies on bare and Mg-doped $LiCoO_2$ as a cathode material for lithium-ion batteries. *Electrochim. Acta*, *128*, pp.192-197.
109. Lin, D., Liu, Y., Cui, Y., 2017. Reviving the lithium metal anode for high-energy batteries. *Nat. Nanotechnol.*, *12*(3), pp. 194-206.
110. Erickson, E. M., Markevich, E., Salitra, G., Sharon, D., Hirshberg, D., de la Llave, E., Shterenberg, I., Rosenman, A., Frimer, A. and Aurbach, D., 2015. Development of advanced rechargeable batteries: a continuous challenge in the choice of suitable electrolyte solutions. *J. Electrochem. Soc.*, *162*(14), A2424
111. Chen, Z., Qin, Y., Amine, K., Sun, Y. K. Role of surface coating on cathode materials for lithium-ion batteries. *J. Mater. Chem*., *20* (36), 2010, pp. 7606-7612.

112. Huang, X., Zhang, Z., He, J., Bai, Z., Lu, L. and Li, J., 2021. Effects of chromium/fluorine co-doping on the electrochemical performance of $Li_{1.2}Ni_{0.13}Co_{0.13}Mn_{0.54}O_2$ cathode material for lithium-ion batteries. *J. Mater. Sci.*, *56*(16), pp. 9836-9851.
113. Huang, Z., Wang, Z., Guo, H. and Li, X., 2016. Influence of Mg^{2+} doping on the structure and electrochemical performances of layered $LiNi_{0.6}Co_{0.2-x}Mn_{0.2}Mg_xO_2$ cathode materials. *J. Compd.*, *671*, pp.479-485.
114. Huang, B., Li, X., Wang, Z., Guo, H. and Xiong, X., 2014, Synthesis of Mg-doped $LiNi_{0.8}Co_{0.15}Al_{0.05}O_2$ oxide and its electrochemical behavior in high-voltage lithium-ion batteries. *Ceram. Int.*, *40*(8), pp.13223-13230.
115. Myung, S.T., Izumi, K., Komaba, S., Sun, Y.K., Yashiro, H., Kumagai, N. 2005. Role of alumina coating on Li−Ni− Co− Mn− O particles as positive electrode material for lithium-ion batteries. *Chem. Mater.*, 17(14), pp.3695-3704.
116. Xin, F., Zhou, H., Chen, X., Zuba, M., Chernova, N., Zhou, G., Whittingham, M.S., 2019. Li–Nb–O Coating/Substitution Enhances the Electrochemical Performance of the $LiNi_{0.8}Mn_{0.1}Co_{0.1}O_2$ (NMC811) Cathode. *ACS appl. Mater. Interfaces*, *11*(38), pp. 34889-34894.
117. Chen, C. H., Liu, J., Stoll, M. E., Henriksen, G., Vissers, D. R., Amine, K., 2004. Aluminum-doped lithium nickel cobalt oxide electrodes for high-power lithium-ion batteries. *J. Power Sources*, *128*(2), pp.278-285.
118. Mofid, E., Ivanov, W., S., Konkin, A., Bund, A., 2014. A high performance layered transition metal oxide cathode material obtained by simultaneous aluminum and iron cationic substitution. *J. Power Sources*, *268*, pp. pp.414-422.
119. Idemoto, Y., Kitamura, N., Ueki, K., Vogel, S.C. and Uchimoto, Y., 2012. Average and local structure analyses of Li $(Mn_{1/3}Ni_{1/3}Co_{1/3-x}Al_x)$ O_2 using neutron and synchrotron X-ray sources. *J. Electrochem. Soc.*, *159*(5), p.A673.
120. Aurbach, D., Srur-Lavi, O., Ghanty, C., Dixit, M., Haik, O., Talianker, M., Grinblat, Y., Leifer, N., Lavi, R., Major, D.T. and Goobes, G., 2015. Studies of aluminum-doped $LiNi_{0.5}Co_{0.2}Mn_{0.3}O_2$: electrochemical behavior, aging, structural transformations, and thermal characteristics. *J. Electrochem. Soc.*, *162*(6), p.A1014.
121. You, Y., Celio, H., Li, J., Dolocan, A. and Manthiram, A., 2018. Modified high-nickel cathodes with stable surface chemistry against ambient air for lithium-ion batteries. *Angew. Chem.*, *130*(22), pp. 6590-6595.
122. Yoshinaga, N., Kumakura, S., Kubota, K., Horiba, T., Komaba, S., 2019. Lithium Magnesium Tungstate Solid as an Additive into $Li(Ni_{1/3}Mn_{1/3}Co_{1/3})O_2$ Electrodes for Li-Ion Batteries. *J. Electrochem. Soc.*, *166*(3), p. A5430.
123. Chen, Y., Zhang, Y., Chen, B., Wang, Z., Lu, C., 2014. An approach to application for $LiNi_{0.6}Co_{0.2}Mn_{0.2}O_2$ cathode material at

high cut-off voltage by TiO_2 coating. *J. Power Sources*, *256*, pp. 20–27.

124. Jun, D.W., Yoon, C.S., Kim, U.H., Sun, Y.K., 2017. High-energy density core–shell structured $Li(Ni_{0.95}Co_{0.025}Mn_{0.025})O_2$ cathode for lithium-ion batteries. *Chem. Mater*., *29*(12), pp. 5048-5052.

125. Yan, P., Zheng, J., Liu, J., Wang, B., Cheng, X., Zhang, Y., Sun, X., Wang, C., Zhang, J. G., 2018. Tailoring grain boundary structures and chemistry of Ni-rich layered cathodes for enhanced cycle stability of lithium-ion batteries. *Nat. Energy*. *3*, pp. 600-605.

126. Chikkannanavar S.B., Bernardi, D. M., Liu, L. 2014. A review of blended cathode materials for use in Li-ion batteries. *J. Power Sources*, *248*(2014),pp91-100

127. Zhao, J., Wang, Y., 2013. Surface modifications of Li-ion battery electrodes with various ultrathin amphoteric oxide coatings for enhanced cycleability, *J. Solid State Electrochem.*, *17*, pp. 1049-1058.

128. Morales-Ugarte, J. E., Bolimowska, E., Rouault, H., Santos-Pena, J., Santini, C. C., and Benayad, A., 2018. EIS and XPS investigation on SEI layer formation during first discharge on graphite electrode with a vinylene carbonate doped imidazolium based ionic liquid electrolyte. *J. Phys. Chem*. C, *122*, pp. 18223–18230

129. Heineman W.R. and Kissinger P. T. in *Laboratory Techniques in Electrochemistry* Marcel Dekker (1996) New York.

130. Taewhan, K., Woosung, C., Heon-Cheol, S., Jae-Young, C., Ji, M. K., Min-Sik, P., Won-Sub, Y., 2020. Applications of voltammetry in lithium-ion battery research. *J. Electrochem. Sci. and Technol., 11*(1), pp. 14-25

131. Lee, W., Muhammad, S., Kim, T., Kim, H., Lee, E., Jeong, M., Son, S., Ryou, J.H. and Yoon, W.S., 2018. New insight into Ni-rich layered structure for next-generation Li rechargeable batteries. *Adv, Energy Mater.*, *8*(4), p.1701788.

132. Bard, A. J., and Faulkner L.R., 1980. *Electrochemical methods: Fundamentals and application,* 1980. John Wiley & Sons, New York 1st ed.

133. Wang, J., 1994. *Analytical Electrochemistry* VCH publishers Inc. New York.

134. Brownson, D.A., Kampouris, D.K. and Banks, C.E., 2012, Graphene electrochemistry: fundamental concepts through to prominent applications. *Chem. Soc. Rev.*, *41*(21), pp. 6944-6976.

135. Aoki, K., Tokuda, K. and Matsuda, H., 1983. Theory of linear sweep voltammetry with finite diffusion space. *J. Electroanal. Chem. Interfacial Electrochem.*, *146*(2), pp.417-424.

136. Aoki, K., Tokuda, K. and Matsuda, H., 1984. Theory of linear sweep voltammetry with finite diffusion space: Part II. Totally irreversible and quasi-reversible cases. *J. Electroanal. Chem. Interfacial Electrochem.*, *160*(1-2), pp.33-45.

137. Lindström, H., Södergren, S., Solbrand, A., Rensmo, H., Hjelm, J., Hagfeldt, A., Lindquist, S.E., 1997. Li^+ ion insertion in TiO_2 (anatase). 2. Voltammetry on nanoporous films. *J. Phys. Chem. B.*, *101*(39), , pp.7717-7722.
138. Yang, S., Zhou, X., Zhang, J. and Liu, Z., 2010. Morphology-controlled solvothermal synthesis of $LiFePO_4$ as a cathode material for lithium-ion batteries. *J. Mater. Chem.*, *20*(37), pp.8086-8091.
139. Kim, T., Choi, W., Shin, H.C., Choi, J.Y., Kim, J.M., Park, M.S. and Yoon, W.S., 2020. Applications of voltammetry in lithium-ion battery research. *J. Electrochem. Sci. Technol.*, *11*(1), pp.14-25.
140. Kim, Y., Kim, D.S., Um, J.H., Yoon, J., Kim, J.M., Kim, H. and Yoon, W.S., 2018. Revisiting solid electrolyte interphase on the carbonaceous electrodes using soft X-ray absorption spectroscopy. *ACS Appl. Mater. Interfaces*, *10*(35), pp.29992-29999.
141. Li, T., Yuan, X. Z., Zhang, L., Song, D., Shi, K., and Bock, C., 2020, Degradation mechanisms and mitigation strategies of nickel-rich NMC-based lithium-ion batteries. *Electrochem. Energy Rev.*, *3*(1), pp. 43-80
142. Jiang, L.H., Wang, Q.S., Sun, J.H., 2018. Electrochemical performance and thermal stability analysis of $LiNiCoMnO_2$ cathode based on a composite safety electrolyte. *J. Hazard. Mater. 351*, pp. 260–269
143. Makgopa, K., Ejikeme, P. M., Jafta, C. J., Raju, K., Zeiger, M., Presser, V., Ozoemena, K. I., 2015. A high-rate aqueous symmetric pseudocapacitor based on highly graphitized onion-like carbon/birnessite-type manganese oxide nanohybrids. *J. Mater. Chem. A*, *3*(7), 3480-3490.
144. Krause, A., Kossyrev, P., Oljaca, M., Passerini, S., Winter, M., and Balducci, A., 2011. Electrochemical double layer capacitor and lithium-ion capacitor based on carbon black. *J. Power Sources*, *196*(20), pp. 8836-8842.
145. Jung, R., Morasch, R., Karayaylali, P., Phillips, K., Maglia, F., Stinner, C., Shao-Horn, Y., Gasteiger, H. A., 2018. Effect of ambient storage on the degradation of Ni-rich positive electrode materials (NMC811) for Li-ion batteries, *J. Electrochem. Soc.*, *165*(2), A132.
146. Yang, J., Xia, Y., 2016. Suppressing the phase transition of the layered Ni-rich oxide cathode during high-voltage cycling by introducing low-content Li_2MnO_3, *ACS Appl. Mater. Interfaces*, **8**(2), pp. 1297-1308.
147. Ohzuku, T., Ueda, A., Nagayama, M., 1993. Electrochemistry and structural chemistry of $LiNiO_2$ (R-3m) for 4 V secondary lithium cells, *J. Electrochem. Soc., 140***,** pp. 1862−1870.
148. Dahn, H. M., Smith, A. J., Burns, J. C., Stevens, D. A., Dahn, J. R., 2012. User-friendly differential voltage analysis freeware for the analysis of degradation mechanisms in Li-ion batteries. *J. Electrochem. Soc.*, *159*, pp. A1405–A1409

149. Günter, F. J., Habedank, J. B., Schreiner, D., Neuwirth, T., Gilles, R., & Reinhart, G., 2018. Introduction to electrochemical impedance spectroscopy as a measurement method for the wetting degree of lithium-ion cells. *J. Electrochem. Soc.*, *165*(14), A3249.
150. Meddings, N., Heinrich, M., Overney, F., Lee, J.S., Ruiz, V., Napolitano, E., Seitz, S., Hinds, G., Raccichini, R., Gaberšček, M., Park, J., 2020. Application of electrochemical impedance spectroscopy to commercial Li-ion cells: A review. *J. Power Sources*, *480*, p.228742.
151. Liang, L., Hu, G., Jiang, F., Cao, Y., 2016. Electrochemical behaviours of SiO_2-coated $LiNi_{0.8}Co_{0.1}Mn_{0.1}O_2$ cathode materials by novel modification method, *J. Alloys Compd.*, *657*, pp. 570-581.

Chapter 3

Experimental

3. Experimental

3.1. Reagents and characterizations

In this section reagents used, instruments employed, and experimental procedures are going to be outlined.

3.1.1. Reagents

Commercial NMC622, Carbon black, polyvinylidene fluoride (PVDF), N-Methyl pyrrolidine (NMP) and $LiPF_6$, were used without modification while ethylene carbonate (EC). Diethyl carbonate (DEC) and dimethyl carbonate (DMC) were dried using molecular sieves before use. They were all from Shandong Gelon LIB Co. LTD. The reagents $Mn(NO_3)_2{\cdot}4H_2O$, $LiNO_3$, LiOH, $MnSO_4{\cdot}H_2O$, $Co(NO_3)_2{\cdot}6H_2O$, $Ni(NO_3)_2{\cdot}6H_2O$, $Ce(NO_3)_3{\cdot}6H_2O$, ammonium hydroxide and NaOH from Sigma Aldrich were also used without further purification.

3.1.2. Instruments

Heating was done in a programmable tube furnace. Temperature of this furnace is controlled by a highly precise SCR power controller with +/-1°C accuracy and it was programmed to heat at 3°C/min each time. The crystal structures were analysed using Raman spectroscopy, scanning electron

microscopy (SEM), TEM and powder X-ray diffraction. A Horiba Jobin-Yvon LabRAM HR Raman spectrometer equipped with an Olympus BX41 microscope attachment was used to obtain the Raman spectra. PXRD was carried using Bruker D2 diffractometer 580 equipped with Cu Kα radiation (λ = 1.54178 Å and scanned within range 10º-90º at a scanning rate of 2.7º/min. The morphology of the powders was studied using the Zeiss SEM and TEM to characterise the coating.

3.1.3. Electrochemical measurement

Electrochemical tests were carried out as half-cell measurements using R2032 coin cells. Typically, cathode electrodes were fabricated from an 8:1:1 mass ratio of the active LIB material, PVDF binder and carbon black. First the binder was placed in an agate mortar and NMP was added as the solvent and combined, then the combined LIB and carbon powders were added, and all were mixed into a slurry. The prepared slurry was evenly applied onto an aluminium foil current collector using a coating machine. The coated sheet was placed in a vacuum oven at 120 ºC overnight to dry before calendaring. The coated electrode sheet was then cut into 12 mm diameter discs and transferred to an argon-filled MBraun glovebox for cell fabrication. The R2032 coin cells were assembled in an argon-filled glovebox using the coated cathode discs, lithium foil discs as an anode, 1 M LiPF6 in EC/DEC/DMC (1:1:1 volume ratio) as the electrolyte and micro-porous polypropylene Celgard H1612/16 µm as the separator, Figure 3-1.

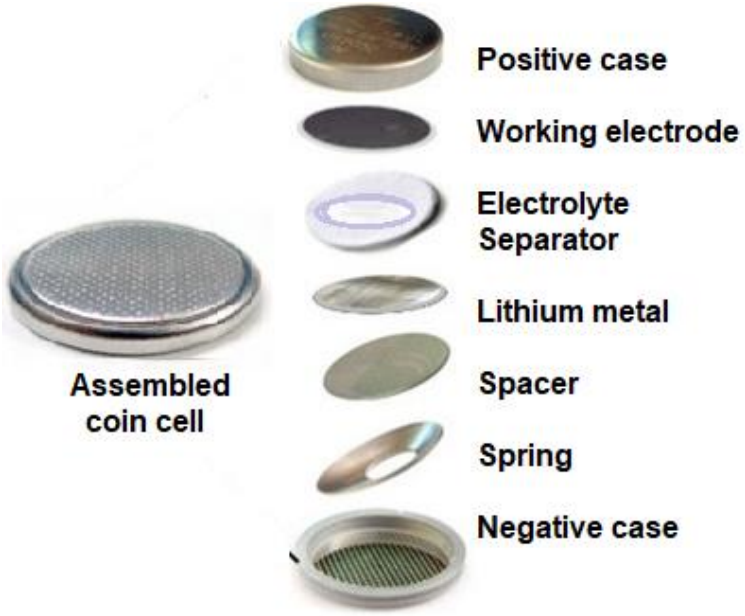


Figure 3-1 Schematic of a coin cell assembly for half cells.

The electrochemical measurements: Cyclic voltammetry (CV), galvanostatic charge-discharge cycling (GC-D) and electrochemical impedance spectroscopy (EIS) were carried out on a BioLogic system (BCS-8xx series). A BT-Lab program was used for data acquisition and analysis.

3.2. Synthesis of compounds

Synthesis of NMC811 was carried out as outlined in literature.[1] The variation is that analytical reagents $Ni(NO_3)_2{\cdot}6H_2O$, $MnSO_4{\cdot}H_2O$ and $Co(NO_3)_2{\cdot}6H_2O$ were used to make the precursor $Ni_{0.8}Co_{0.1}Mn_{0.1}(OH)_2$ instead of the corresponding sulphates.

3.2.1. Preparation of NMC811

Pristine NMC811 was prepared as summarised in Figure 3-2. Co-precipitation method was used to prepare $Ni_{0.8}Mn_{0.1}Co_{0.1}(OH)_2$, a precursor for pristine NMC811 (NMC811-p) and microwave treated NMC811(NMC811-p_MW). The analytical reagents $Ni(NO_3)_2{\cdot}6H2O$, $MnSO_4{\cdot}H_2O$ and $Co(NO_3)_2{\cdot}6H_2O$ were weighed according to the molar ratio 8:1:1, combined and dissolved in degassed deionized water to form a 2 M solution by total mole fraction of the metal salts and kept aside. Another solution of 1 M NH_4OH was prepared and added to a laminar flow reactor and heated to 60 °C. A nitrogen blanket was created over the solution. A complexing buffer was also prepared using 4 M NaOH as the precipitating agent and 2 M NH_4OH as the chelating agent. The metal salts' solution and the complexing buffer were then pumped into a rapidly whirling laminar flow reactor at the rate of 0.5 ml/min and 0.15 ml/min, respectively. The pH value was maintained between pH11$\pm$ 0.5 by adjusting the flow of NaOH. This mixture was allowed to age for 19 h while under nitrogen at 60 °C. Finally, the precipitated $Ni_{0.8}Mn_{0.1}Co_{0.1}(OH)_2$ precursor was filtered out, repeatedly washed with distilled water and then vacuum dried at 80 °C for 12 h. The dry $Ni_{0.8}Mn_{0.1}Co_{0.1}(OH)_2$ and LiOH were weighed according to the mole ratio of 1:1.05 then ground into a uniform mixture in an agate mortar and pestle. The extra 5% Li was to compensate for loss of Li during elevated temperature calcination. The mixture was then pre-calcined at 500 °C for 5 h. It was allowed to cool, ground again into a powder divided into two portions. One portion was further calcined for 16 h at 750 °C in an oxygen-

blanket atmosphere in a tube furnace to form pristine NMC811 (NMC811-p). The other portion was microwave treated at 600 W for 20 min before further calcining at 750°C for 16h C in an oxygen-blanket atmosphere in a tube furnace to form microwave-treated pristine NMC811 (NMC811-p_MW).

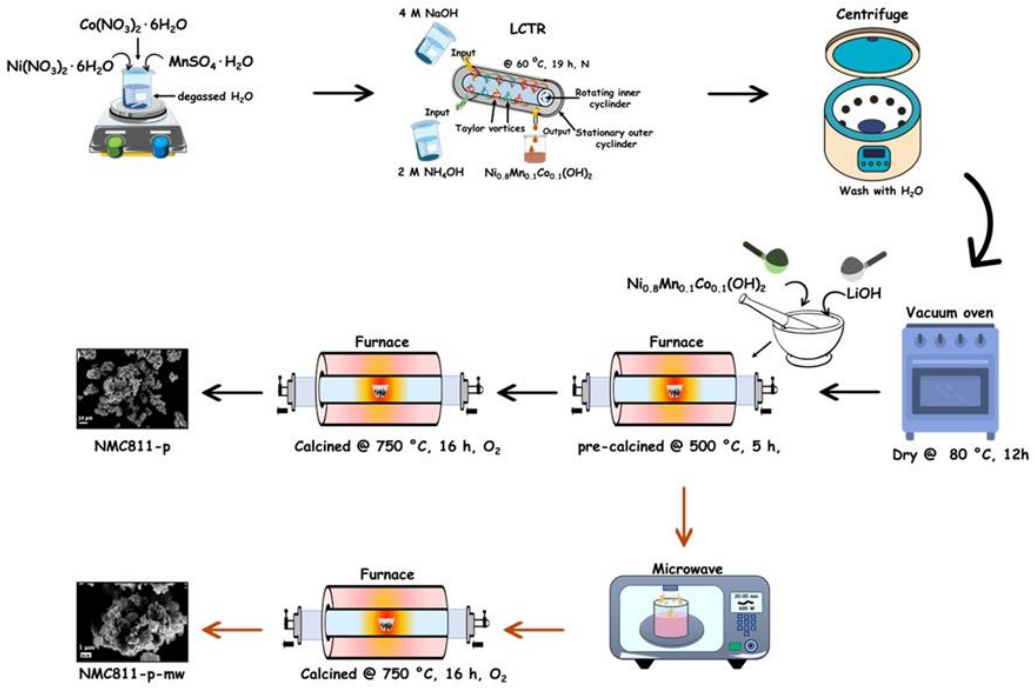


Figure 3-2 Schematic of the synthesis of NMC811-p and NMC811-p_MW

In the same way used to prepare the pristine cathode powder, CeO_2-doped NMC811 and its microwave treated adduct were prepared by the co-precipitation method from the precursor $Ce_\delta(Ni_{0.8}Mn_{0.1}Co_{0.1})_{-\delta}(OH)_2$ as summarised in Figure 3-3. A metal solution mixture was made in the same way as in the preparation of NMC811 but with the addition of an amount of $Ce(NO_3)_3 \cdot 6H_2O$ to contribute enough Ce^{3+}.

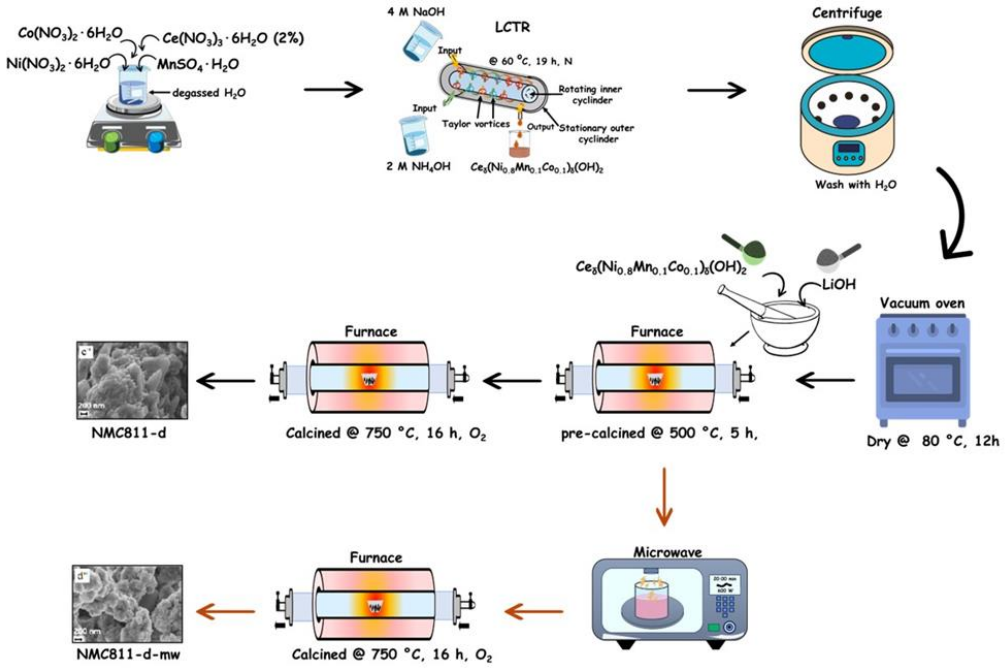


Figure 3-3 Schematic of the synthesis of NMC811-d and NMC811-d_MW.

Relatively the same amount of Ce ions per mass of NMC was used for the NMC811-d as was used in NMC811-c. A portion each of NMC811-c and NMC811-d were irradiated with microwaves for 20 min at 600 W to form NMC811-d_MW and NMC811-c_MW.

3.2.2. Preparation of coated NMC

Synthesis of CeO_2-coated NMC811 by mass was made by weighing out enough $Ce(NO_3)_3 \cdot 6H_2O$ to contribute the Ce^{3+} ions for a 2% CeO_2 by mass of NMC811-p. The nitrate salt was then dissolved in deionised water and the weighed NMC811-p was added and dispersed in an ultrasound sonicator bath. Polyvinyl alcohol (PVA) was stirred into the mixture. The resultant suspension was left to dry in a vacuum oven at 80 ºC. The dry residue was ground and thoroughly mixed in an agate mortar and pestle

and divided into two portions. A portion of the powder was subjected to heat treatment at 450ºC for 5 hours in a tube furnace. It was finally cooled, ground, and stored as CeO_2-coated NMC811 (NMC811-c). The other portion was microwave treated at 600 W for 20 min and it was finally heat treated at 450 ºC for 5 hours in a tube furnace to form NMC811-c_MW. The synthetic route is summarised in Figure 3-4.

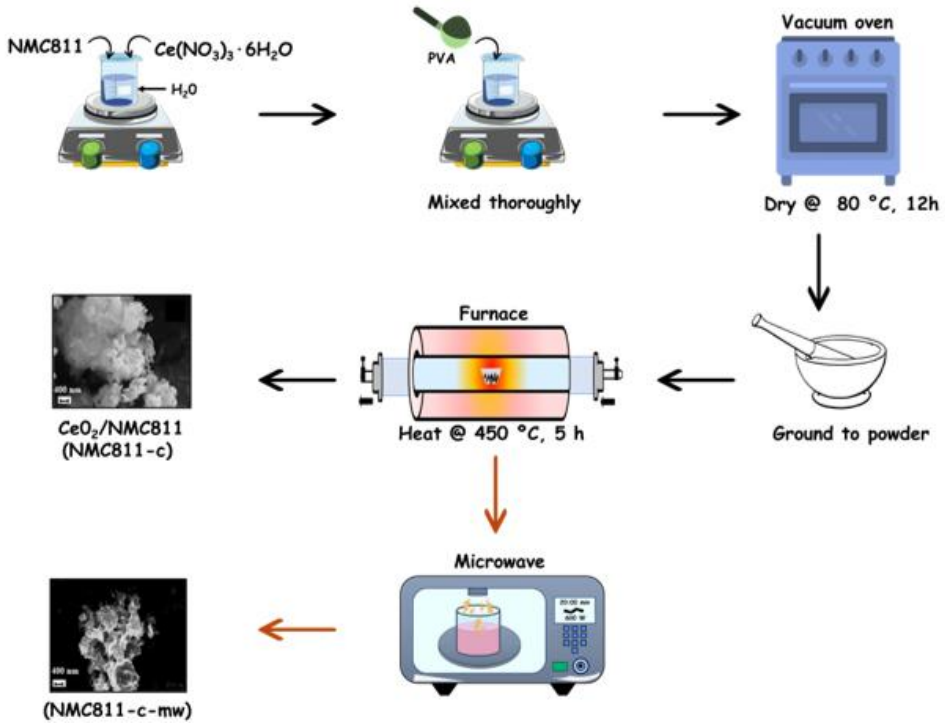


Figure 3-4 Schematic of the synthesis of NMC811-c and NMC811-c_MW.

The same method was followed for CeO_2 -coated NMC622 (NMC622-c)as summarised by Figure 3-5. Commercial NMC622 (NMC622).was analysed and used as is.

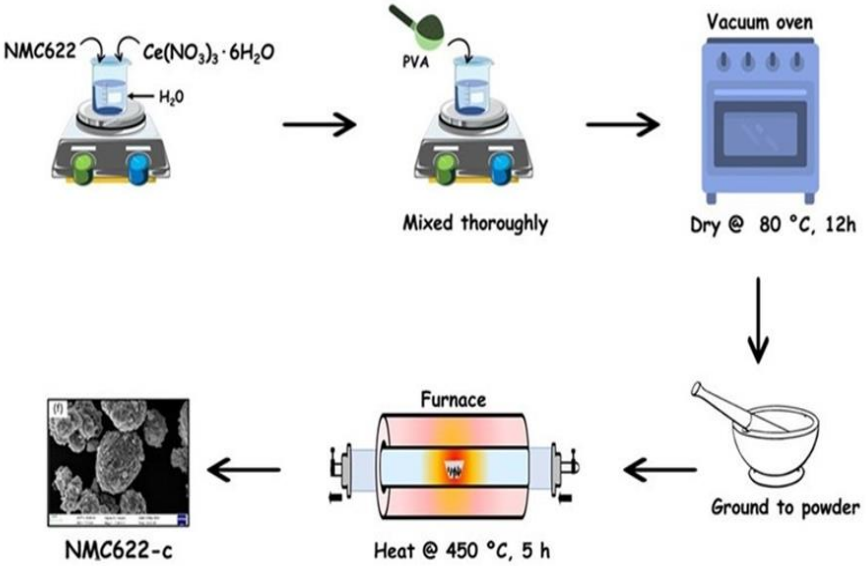


Figure 3-5 Schematic of the synthesis method of NMC NMC622-c

REFERENCES

1. Wu, L., Tang, X., Chen, X., Rong, Z., Dang, W., Wang, Y., Li, X., Huang, L., Zhang, Y., Improvement of electrochemical reversibility of the Ni-Rich cathode material by gallium doping, *J. Power Sources*, **445**, 2020, 227337.

Chapter 4

Enhancing the electrochemical performance of $LiNi_{0.6}Mn_{0.2}Co_{0.2}O_2$ (NMC NMC622) by ultrathin conductive CeO_2 surface coating

---

4. Introduction

In this chapter we report on the coating of NMC622 with a small amount of CeO_2.

4.1. Introduction to $LiMn_{0.6}Ni_{0.2}Co_{0.2}O_2$

The development of EVs and PHEVs has caused a stir in modern technology as the need to substitute fossil fuels with more green energy intensifies.[1-3] As Armand and Tarascon wrote, “Researchers must find a sustainable way of providing the power our modern lifestyles demand”.[4] The latest war in European Russia has even forced some European states to review and advance their plans to fulfil their electricity supply with 100% renewable sources by 2035. Germany which has made this declaration sources its green energy mainly from biomass, wind, solar and hydropower power. Some of these are intermittent and need energy conversion and storage from source to consumption point. Concerning EVs, consumers are still wary about the properties of the batteries, such as battery life, driving range and safety. Most of these properties can be corrected by improved or the discovery of new cathode material with improved specific capacity.[3]

Nickel-rich NMC with the general formula $LiNi_xMn_yCo_zO_2$ where $x \geq 0.6$) has been touted to be a good candidate for energy-intense applications.[4-6] They are layered materials, and better poised for easy diffusion of lithium ions. Their limiting shortfalls were discussed earlier in Section 2.5. Their high theoretical capacities (~275 mA. hg^{-1}) make them highly desirable. Nickel-enriched NMC material (where $x \geq 0.6$) have less cobalt and as such they are cheaper; they have higher specific capacity and are more benign to the environment. However, Ni-rich NMC has a poor life cycle, high capacity-decay, high thermal instability, and high instability in environmental conditions including in ambient air. These are caused by cationic mixing between Ni and Li ions,[7,8] side reactions with the electrolyte and the residual lithium on the surface of the material and high delithiation which leads to the formation of highly oxidising Ni^{4+}. The presence of Ni^{4+} hastens structural degradation which could lead thermal runaway through the reaction with the electrolyte and cause battery failure.[9] The highly oxidising Ni^{+} ions combine with oxygen and other groups to form solid compounds such as nickel's only known stable oxide, NiO. The solid oxide deposits on the surface of the cathode increases the solid electrolyte interface (SEI) which leads to an increase in ion transfer resistance and capacity fading. Alongside these are structural failures that occur due to the loss of oxygen from the crystal structure framework, and which also lead to capacity loss.[5,8,10] Surface degradation of nickel rich NMC cathode material is deemed to be the major cause of capacity decay during long cycling for this class of cathode materials. Surface degradation can occur due to side reactions with the

electrolyte. Also, there is anisotropic volume change that happens especially in Ni-rich cathodes during the charge-discharge process.[11-15] This induces stress on the structural integrity of the cathode, ultimately resulting in the development of microcracks. These microcracks allow seepage of the electrolyte into the core of the secondary cathode units, hence augmenting the surface area that comes into contact with the electrolyte leading to higher interphase resistance, and consequently capacity loss.

Successful commercialization of NMC has been achieved with the low Ni content formulation, however, these tend to have slightly lower energy density. Recently NMC NMC622 has also been commercialised amid the challenges discussed here.

Strategies adopted by researchers to combat these problems are meant to reinforce the structure of the cathode material including by coating and doping to slightly alter the composition of the material. Coating the surface of materials has been used for protection against corrosion by acting as a physical barrier which protects and cuts down surface degradation because of direct cathode-electrolyte contact. Surface and near-surface properties are largely responsible for some of the reactions of the material, and they can determine the performance behaviour of a material. Since NMC degradation mechanisms can be chemical or structural, coating that modifies these aspects can affect the materials efficiency as a cathode. The properties of the coat can impact the electrochemical properties such as electronic and or ionic conductivity and in turn boost performance in capacity. They may also affect the kinetics of the charge-discharge cycling

while preventing chemical fouling by the reactions with the electrolyte.[16] For instance, Al_2O_3 has been reported to improve Li conductivity thereby supporting good Li migration kinetics during cycling. Many researchers have investigated metal oxides such as ZrO_2, Al_2O_3,[8,16] CeO_2 [17-20] and others like AlF_3,[9] C and SiO_2,[4] as coating materials for different cathode materials. It is expected that coating electrode material should increase the cell impedance since the coat adds to the migration distance.

In this work we report the study of coating Ni-rich NMC622 with CeO_2. Cerium is a rare earth metal however, cerium is the 26th most abundant element in the earth's crust after copper. Its rarity is associated with the fact that it is not found as concentrated deposits in the earth's crust. Patel et al. reported that coating LMO and LMNO with CeO_2 more than doubled the electronic and ionic conductivities of those cathode materials and reported an improvement in discharge capacity and cycle life.[19, 20]

4.2. Experimental

Commercial NMC622, Carbon black, PVDF, NMP and $LiPF_6$, were used without modification while EC. DEC and DMC were dried using molecular sieves before use and kept within the argon-filled glovebox. These materials were all from Shandong Gelon LIB Co. LTD. The reagents $Ce(NO_3)_3 \cdot 6H_2O$ (Sigma-Aldrich) and ammonium hydroxide, NaOH (Sigma Aldrich), were also used without further purification.

4.2.1. Instrumentation

The crystal structures were analysed using Raman spectroscopy, scanning electron microscopy (SEM), TEM and powder X-ray diffraction. A Horiba

Jobin-Yvon LabRAM HR Raman spectrometer equipped with an Olympus BX41 microscope attachment was used to obtain the Raman spectra. PXRD was carried using Bruker D2 diffractometer 580 equipped with Cu Kα radiation (λ = 1.54178 Å and scanned within the range of 10º-90º at a scanning rate of 2.7º/min. Zeiss SEM and TEM microscopes were used to characterise the morphology of the powders.

4.2.2. Electrochemical measurement

Electrochemical tests were carried out using R2032 coin cells. Typically, cathode electrodes were fabricated from an 8:1:1 mass ratio of the LIBs (NMC622 and CeO_2 coated NMC622), polyvinylidene fluoride (PVDF) binder and carbon black were used. First the binder was placed in an agate mortar and N-Methyl pyrrolidine (NMP) was added as the solvent, then thoroughly combined LIB and carbon were added and mixed into a slurry. The prepared slurry was evenly applied onto an aluminium foil current collector using a coating machine. The coated sheet was placed in a vacuum oven at 120 ºC overnight to dry before calendaring. The coated electrode sheet was then cut into 12 mm diameter discs and transferred to an argon-filled MBraun glovebox for cell fabrication. The R2032 coin cells were assembled using the coated cathode discs, lithium foil discs as anode, 1 M LiPF6 in EC/DEC/DMC (1:1:1 volume ratio) as the electrolyte and micro-porous polypropylene Celgard H1612/16 µm as the separator. The electrochemical measurements: Cyclic voltammetry (CV), galvanostatic charge-discharge cycling (GC-D) and electrochemical impedance

spectroscopy (EIS) were carried out on a BioLogic system (BCS-8xx series). A BT-Lab program was used for data acquisition and analysis.

4.2.3. Preparation of CeO_2 coated NMC622.

A 2% CeO_2 coat for NMC622 was prepared by weighing out enough $Ce(NO_3)_3{\cdot}6H_2O$ to contribute the Ce^{3+} ions for a sample of NMC622. The nitrate salt was then dissolved in deionised water and NMC NMC622 was added and dispersed in an ultrasound sonicator bath. Then PVA was added and mixed thoroughly. The resultant suspension was dried in a vacuum oven at 80 ºC. The dry residue was further mixed in an agate mortar and pestle before treating with heat at 450 ºC for 5 h in a tube furnace. The CeO_2 coated NMC622 was cooled and ground into a powder as outlined in Figure 3-5 brought in from chapter 3.

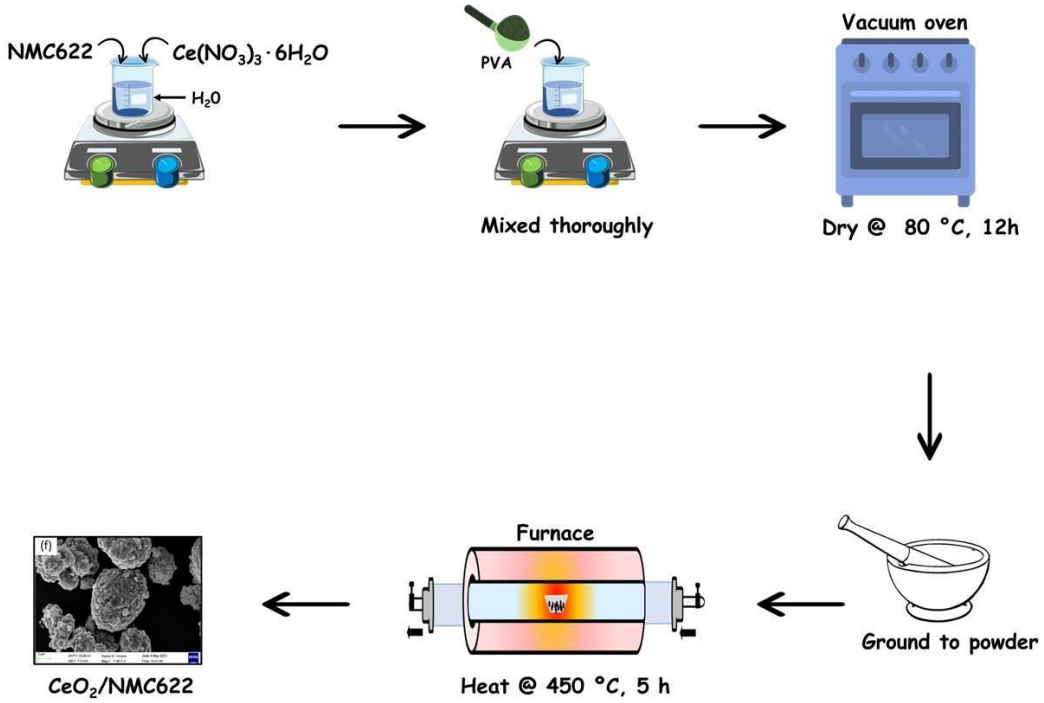


Figure 3-5 Schematic of the synthesis method of NMC622-c

4.3. Results and discussion

4.3.1. XRD

The powder XRD pattern of NMC622 and coated NMC622-c captured between 5-90° is shown in Figure 4-1. They both have a typical $LiMO_2$ structure of $\alpha NaFeO_2$ layered structure with a R3m space group that has been indexed to hexagonal lattice (JCPDS No. 00-066-0854) with the atoms Li, M (M=Ni, Mn, Co) and O, at 3a, 3b and 6c sites as describe for NMC111.[21] The peaks are sharp and with high intensity proving that the particles are crystalline and thus have structural periodicity. The highly crystalline materials show a clear separation of the peaks in the doublets of

(006)/(102) and (018)/(110) which is characteristic of highly ordered layered structure that is free from impurities.[22]

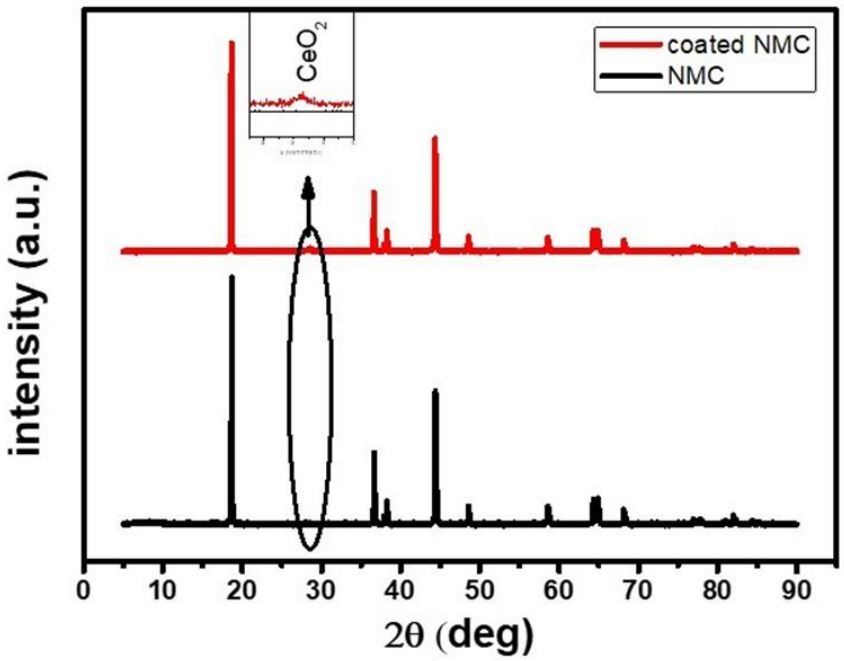


Figure 4-1 XRD patterns of A, NMC622, and B, CeO2-coated NMC622 and the insert shows the expanded area between 27-32 °.

Crystalline CeO_2 is a highly refractive material. The fact that strong fingerprint peaks on the pattern due to CeO_2 are missing suggests that it did not form as a crystalline material. Previous work showed that XRD of a coated material may or may not result in extra peaks of the coating material depending on the amount of the coat added [3,14] and the temperature used to apply the coat. Often much higher temperatures, higher than 700°C, are needed to insert an atom into the host lattice,[14] and this will most likely also cause some shifts in the peak positions. The peak positions are similar for both materials except for the weak signal at ~28.6 ° as shown in the insert in Figure 4-1. This signal is produced by CeO_2, and it is broad which

suggests that the coat may be lacking the close packed structural periodicity of crystalline solids. The broadness is caused by the non-coherence in the arrangement or the positioning of the atoms in the M-O frame. This is a proof that the coating is amorphous, adhering to the surface of the host material and it is most likely thin layered as can be expected because of the small amount, 2% by mass that was theoretically expected. This coating has preserved the layered structure of the bulk material which is suited for easy diffusion of the Li ions. Table 4-1 shows the summary of calculations made from the XRD patterns of NMC622 and NMC622-c. with the ratio of intensity of $I_{(003)}/I_{(104)}$ being 1.85 and 1.87 for NMC622 and NMC622-c, respectively. A ratio >1.2 indicates absence of cationic mixing. The r_1 factor obtained by $I_{(006)}+ I_{(102)}/ I_{(101)}$ is an indicator of hexagonal ordering, where $r_1 < 0.6$ signifies a distinct highly ordered hexagonal structure. This is true for both samples. Thus, the coating neither affected the ordering nor the cationic mixing. Owing to the high similarity in patterns, the CeO_2 coating is not to expected to adversely affect the diffusion of Li within the cathode because it did not change the layered structure of NMC622.

Table 4.1 Cation mixing parameters and lattice parameters of NMC622 and NMC622-c

Cathode material	Intensity ratio ($\frac{I_{003}}{I_{104}}$)	r_1 factor $\frac{I_{(006)}+II_{((102)}}{I_{(102)}}$
NMC622	1.85	0.44
NMC622-c	1.87	0.42

4.3.2. Raman spectra

Figure 4-2(a) shows the Raman spectra of NMC622-c and NMC622 between 350 and 700 Raman shifts. Both spectra are almost similar without an observable signal by O-Ce-O stretches which agrees with the XRD data which could be overlapping with E_g (Ni) around 460 cm^{-1}. This is because of the small amount of CeO_2 formed. Both samples have strong bands between 430 and 640 cm^{-1} which are due to the Raman active A_{1g} and E_g modes of M-O and O-M-O stretches and vibrations for the Ni, Co and Mn found in this region. All six Raman active modes were not easily distinguishable and upon deconvolution only five were picked; the A_{1g}(Ni) mode could not be picked. This is another indication of little cationic mixing as Ni-O and O-Ni-O vibrations are narrower when there is more ordering and little cationic mixing of the Ni and Li atoms.[24]

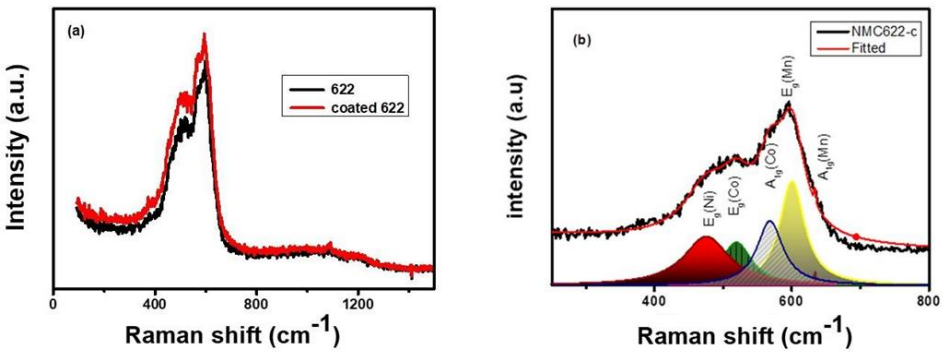


Figure 4-2 Raman spectra of (a) NMC622-c and NMC622 (b) peak assignment

4.3.3. SEM and TEM

Morphology of the samples was studied using SEM. Figure 4-3 shows the SEM images of both NMC622 and NMC622-c. NMC622, Figure 4-3(a) has hexagonal particles with some rough flaky surface while Figure 4-3 (b) shows that NMC622-c, has a smooth topical surface. This shows successful application of the CeO_2 coat.

Probing by energy-dispersive X-ray spectroscopy (EDX) analysis was done on the flaky part and the hexagonal particle and it showed the presence of all expected elements. However, the data on elemental composition shows that the expected atomic and weight percentages were accurate only for the hexagonal particle (cube) as listed in Table 4-2.

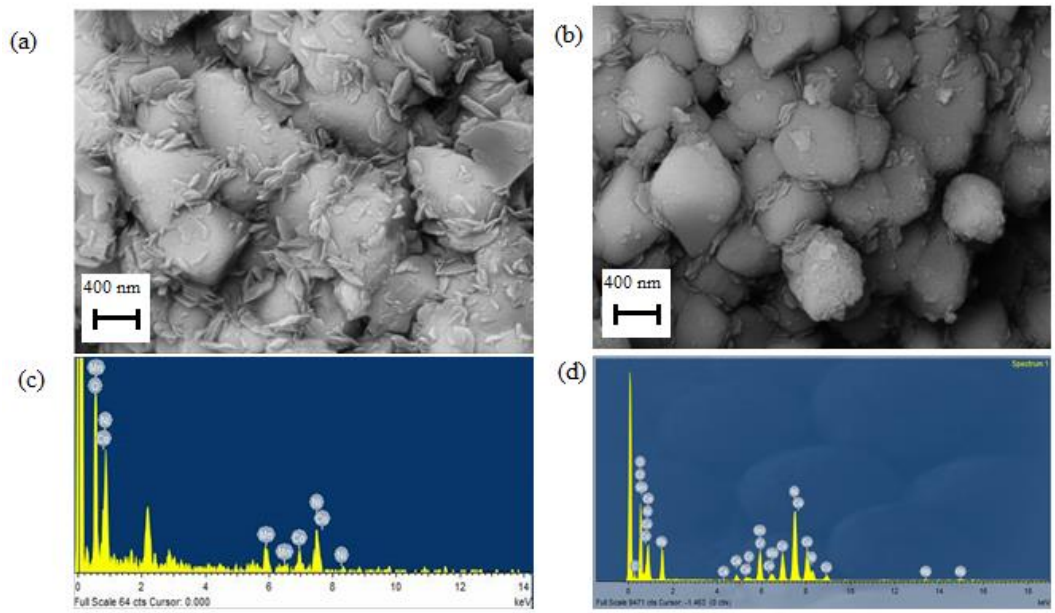


Figure 4-3 SEM images of (a) NMC622 and (b) NMC622-c and EDS of (c) NMC622 and (d) NMC622-c.

Table 4-2. EDX data for NMC622-c

ELEMENT	Weight %			ATOMIC %		
	Flake	Cube	Theoretical	Flake	Cube	Theoretical
O	19.6	32.9	35.6	46.9	64.0	66.7
Mn	13.4	11.2	12.2	9.3	6.4	6.7
Co	21.1	14.8	13.1	13.7	7.8	6.7
Ni	46.0	41.0	39.1	30.1	21.8	20.0

The flakes seen on highest magnification with SEM are most likely degradation products and their elemental composition does not match the theoretically expected one, while the theoretical elemental composition fits for the cube region.

4.3.4. Mapping

Element mapping images are shown in Figure 4-4. Uniform distribution and coverage of the host metal elements can be seen throughout the sampled specimens of both NMC622 and NMC622-c. The metal Ce was also evenly and selectively spread on the NMC622-c sample proving further that indeed Ce was successfully introduced onto the cathode material. An interesting observation can be drawn from the mapping of oxygen and carbon, whereby the pattern by both elements seem to follow the electron image of the sample. However, on the uncoated NMC622 sample, a lot more signal from carbon is found on the sample than on the NMC622-c sample. This further confirms that products of the surface degradation formed could be carbon containing like carbonates from the reaction of surface lithium with atmospheric humidity and carbon dioxide. Comparatively, there is less carbon on the coated sample less carbon on the sample further proves how the CeO_2 has protected the surface of the material against opportunistic side reactions which form carbonates. Quantitatively, Ce seems to be denser even though it was only 2% because it was only on the surface coat, and this implies that it most likely did not penetrate deep into the material in agreement with the SEM observation.

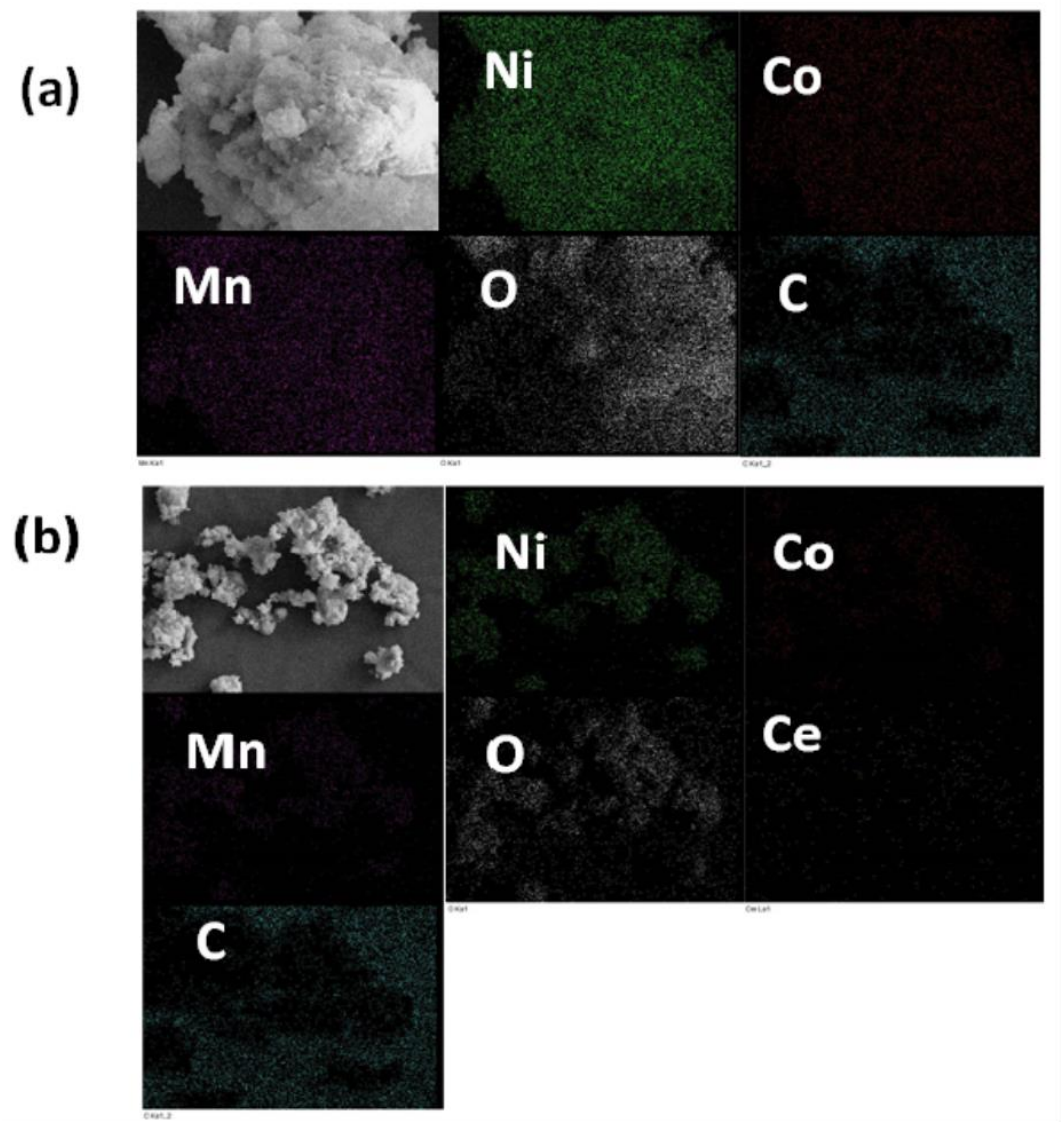


Figure 4-4 EDS mapping of (a) Ni, Mn, Co, C and O for NMC622 and (b) Ni, Mn, Co, Ce, C and O for NMC622-c.

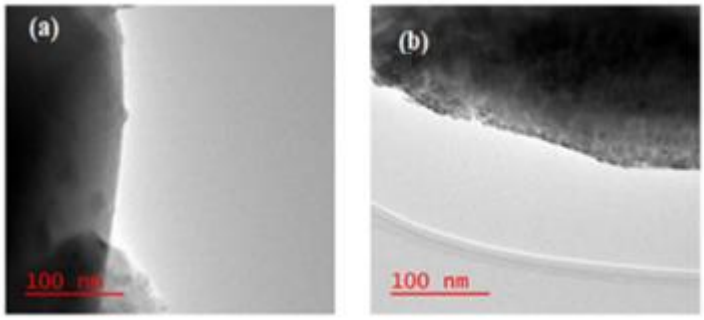


Figure 4-5 TEM images of (a) NMC622, (b) NMC622-c

TEM imaging was carried out to further analyse the surface of the materials. Figure 4-5 shows the image for primary particles of NMC622 and NMC622-c. The particles have variable macro-sized diameter of around 100-150 nm. A thin layer of CeO_2 nanoparticles was formed. The thickness of the layer is around 20-40 nm and is present on the surface of the bulk NMC622-c material while NMC622 has a smooth surface.

4.4. Electrochemical measurements

4.4.1. Cyclic Voltammetry

Figure 4-6 shows the first cyclic voltammogram of NMC622 in 1 M LiPF6 in EC/DEC/DMC (1:1:1 volume ratio) at 0.1 mV/s scan rate. Two oxidation processes were observed for NMC622 with half wave potentials of $E_{\frac{1}{2}} = 3.93\ V$ and 4.32 V vs Li/Li^+ for process I and II, respectively and summarised in Table 4-3. However, on reduction three processes were seen. The first dominant process was the reverse of the first oxidation process at half wave potential of $E_{\frac{1}{2}} = 3.67\ V$, then there was a hump to mark the second process (I*) at $E_{\frac{1}{2}} = 3.92\ V$ and a third process,(II`) as a hump at $E_{\frac{1}{2}} = 4.18$ V vs $Li/Li^+$ The process labelled as II/II` is quasi reversible and it has been

assigned to irreversible Co^{3+}/Co^{4+} reactions processes.

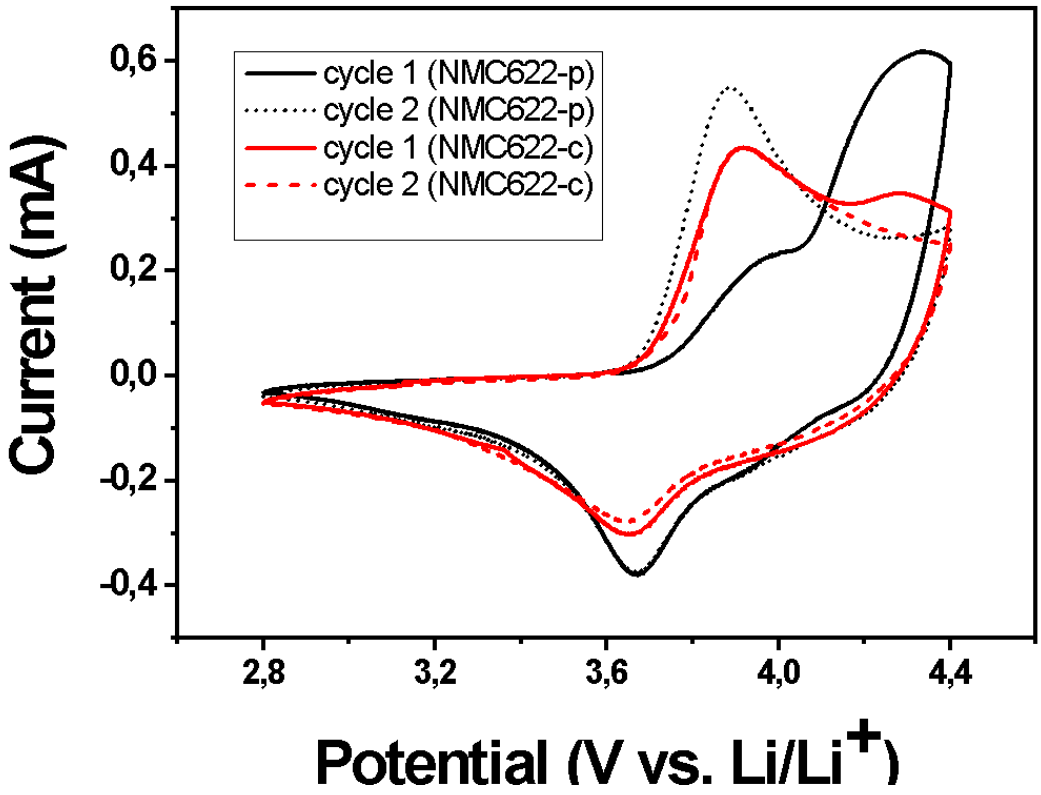


Figure 4-6 Comparative cyclic voltammograms of NMC622 and NMC622-c at 0.1 mVs^{-1}.

Table 4-3 CV peak potentials for NMC622 and NMC622-c and for the dominant peak**.**

compound	***Peak potential ($E_{1/2,\ V\ vs\ Li/Li^+}$)***					
	Oxidation 1st cycle	*Reduction 1st cycle*	*ΔE_P*	*Oxidation 2nd cycle*	*Reduction 2nd cycle*	*ΔE_P*
NMC622	4.32 3.93	3.67	0.26	3.89	3.67	0.22
NMC622-c	4.19 3.92	3.67	0.25	3.95	3.67	0.21

For NMC622 on second cycling the shape and peak currents changed to show a single redox couple, with the oxidation peak at $E_{\frac{1}{2}} = 3.89$ V with a reverse peak on reverse scan at $E_{\frac{1}{2}} = 3.67$ V vs. Li/Li. In contrast NMC622-c has one dominant redox couple with the oxidation peak at $E_{\frac{1}{2}}$ =3.92 V while the reduction is at $E_{\frac{1}{2}} = 3.67$ V vs. Li/Li. The shape of the CV curves and $\triangle E_P$ shows fast kinetics for both the pristine NMC622 and NMC622-c with proves the good electrochemical characteristics of NMC622. NMC622 exhibits faster diffusion than NMC622-c. This is expected owing to the presence of a CeO_2 coat which would lead to slower diffusion of Li ions because of greater distances the ions would have to travel, and the formation of the SEI has negatively affected the performance of the battery.

The oxidation peak at high potential, 4.19 V process II disappeared, suggesting that the process was an irreversible process on the second cycle. The oxidation process at high voltage has been assigned to irreversible Co^{3+}/Co^{4+} redox process. The lack or very low current peak of the reduction peak at 4.21 V seen on scanning of NMC622-c confirms the irreversibility of this process, but it may also show suppression of that redox process by coating. The cyclic voltammograms of NMC622 and NMC622-c had almost similar half potential peaks as summarised in Table 4-3 which further indicates that an ultrathin layer of CeO_2 does not totally block the electrochemical processes of NMC 622.

4.4.2. Galvanostatic charge-discharge.

Galvanostatic charge-discharge was investigated between the potential window of 2.8 - 4.3 V at room temperature. Figure 4-7 shows the rate capabilities that were determined at different C rates (0.1, 0.2, 0.5, 1, 2, 5, 10 and 0.1C). The coated sample, NMC622-c, delivered an initial discharge capacity of ~175 mA hg^{-1} while the NMC622 delivered 17 % more at 202 $mA.hg^{-1-}$ at 0.1 C. Both materials exhibited excellent capabilities, with the coated sample showing an improvement in capacity after the return of the current density to 0.1 C by surpassing its initial capacity by 14% to deliver 200 $mA.hg^{-1}$. This indicates that activation for efficient Li diffusion was initially less efficient for the coated material since it started off at lower capacity, however once it had developed a lithium ions 'highway', the intercalation/deintercalation process improved. This observation suggests that the CeO_2 coat improves conductivity of the NMC622 cathode material and limits the formation of the SEI layer.

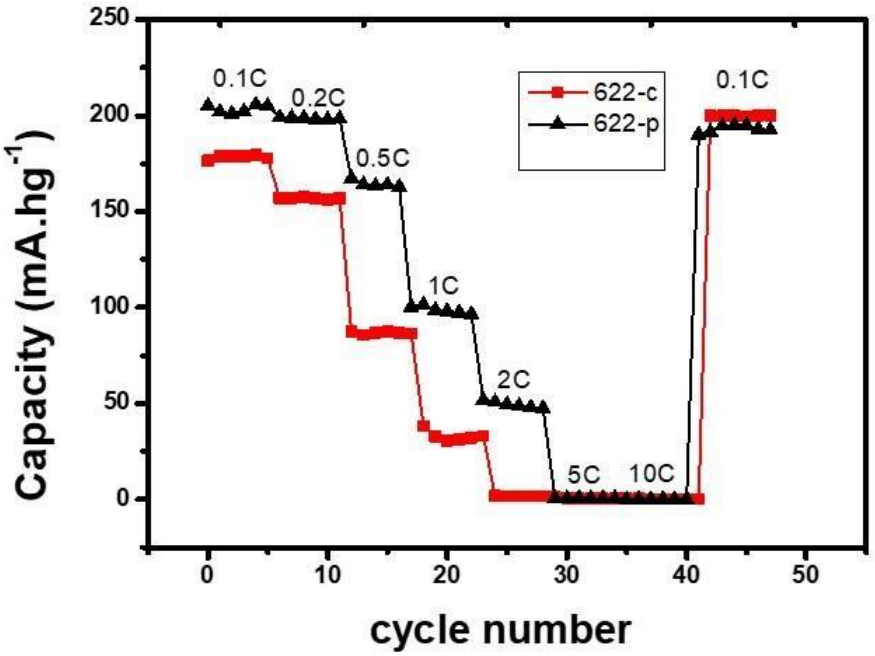


Figure 4-7 Comparison of discharge capacities of pristine NMC and CeO_2 coated NMC622 at different C rates.

Capacity retention and cycling efficiency were tested using a battery by cycling both materials at 0.1 C, (1C = 270 $mA.hg^{-1}$) over 50 cycles. Figure 4-8 shows a representation of the galvanostatic charge-discharge profiles for several cycles between 1 and 50. The pristine NMC622 delivers more discharge capacity of ~205 mA.hg-1 while NMC622-c had an initial discharge capacity of 150 $mA.hg^{-1}$. Similar to the rate capability results, NMC622-c took several cycles to get activated reaching a capacity of 170 $mA.hg^{-1}$ on its 40th cycle while pristine NMC622 started at its maximum capacity and started wasting down almost immediately. Calculated from the maximum capacity, pristine NMC622 delivered a capacity retention of 82% after 50 cycles while NMC622-c gave a 98% retention after 50 cycles, Table 4-4.

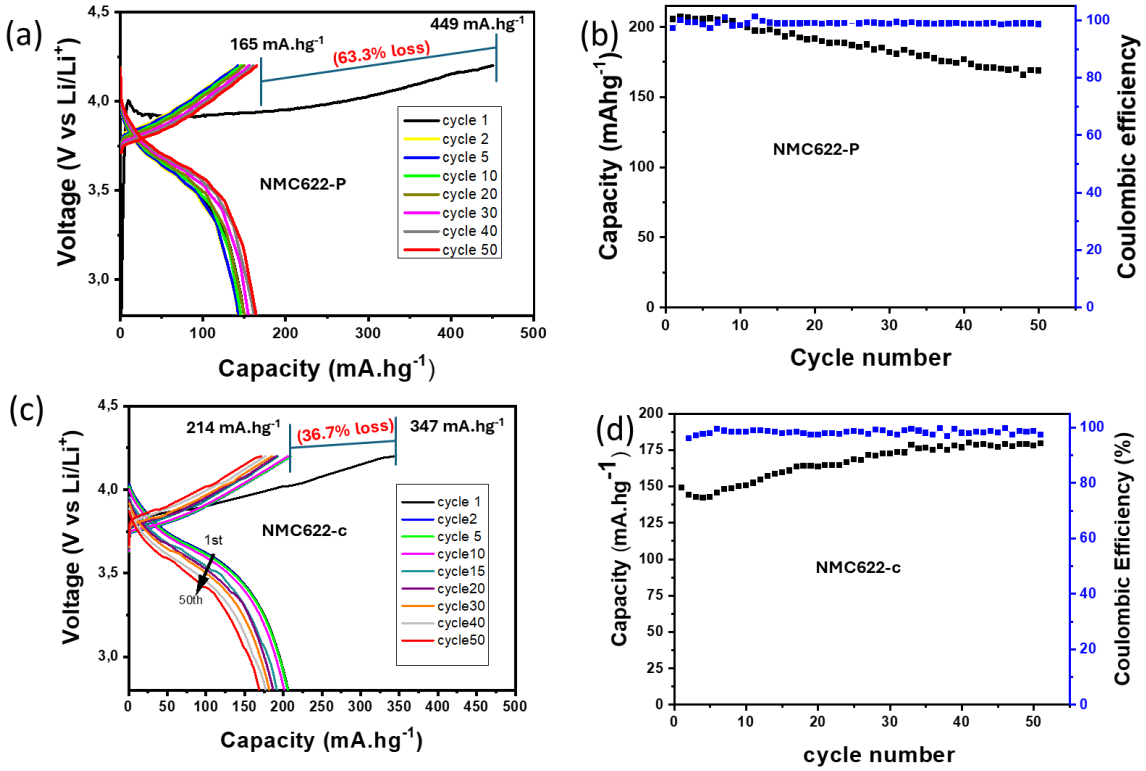


Figure 4-8 Charge-discharge profiles and cycle performance with CE plots for (a),(b) NMC622 and (c), (d) NMC622-c over 50 cycles.

The coulombic efficiency (CE) for the two materials range between 97% and 100% except for the first cycle where it was 60% and 65% for NMC622 and NMC622-c, respectively. Even during the electrode activation stage, the coulombic efficiency is high. High CE is an indication of an efficient operating cell with little side reactions and little loss of lithium during cycling.[25] Such cells are expected to run for a long time. The initial low EC is attributed to the formation of the SEI, while the less than 100% efficiency can be an indication of the growth of the SEI.

Table 4-4 Summary of cyclability studies for NMC622 and NMC622-c

Compound	Specific Capacity ($mAhg^{-1}$)		Capacity retention (%)
	1^{st} cycle	50^{th} cycle	
NMC622	202	169	82
NMC622-c	150	167	98

4.4.3. Electrochemical Impedance Spectroscopy (EIS)

To further probe the effect of coating on diffusion and interfacial resistance, electrochemical impedance spectroscopy (EIS) experiments were carried out on the cells. Figure 4-9(a) compares the Nyquist plots NMC622 and NMC622-c which were satisfactorily fitted with two RC electrical equivalent circuit (EEC) for the NMC622 (Figure 4-9b). However, for the NMC622-c, the EIS data was fitted with one RC combined with the Randles (Figure 4-9c). The profile is attributed to the mixed electronic and ionic kinetic behaviour of materials.[19] The EEC comprises the electrolyte resistance (R_e); the charge-transfer resistance (R_{ct}) corresponding to the redox processes involving the Li^+ ions; the C_f and C_{dl} which denote double layer capacitance arising from the surface film at the high-frequency and pure double layer to the medium frequency region, respectively; the R_{SEI} signifying the high-frequency resistance due to the solid-electrolyte interface (SEI); and Warburg impedance (Z_w) at the low frequency region and signifies the impedance of Li^+ ion diffusion in bulk electrode materials. As shown in Table 4-5, the overall resistance ($R_e + R_{SEI} + R_{ct}$) values are approximately 307 and 167 Ω for NMC622 and NMC622-c, respectively. The results show that

NMC622-c gives the best electrical conductivity relative to NMC622. The EIS results are consistent with the physicochemical data described above.

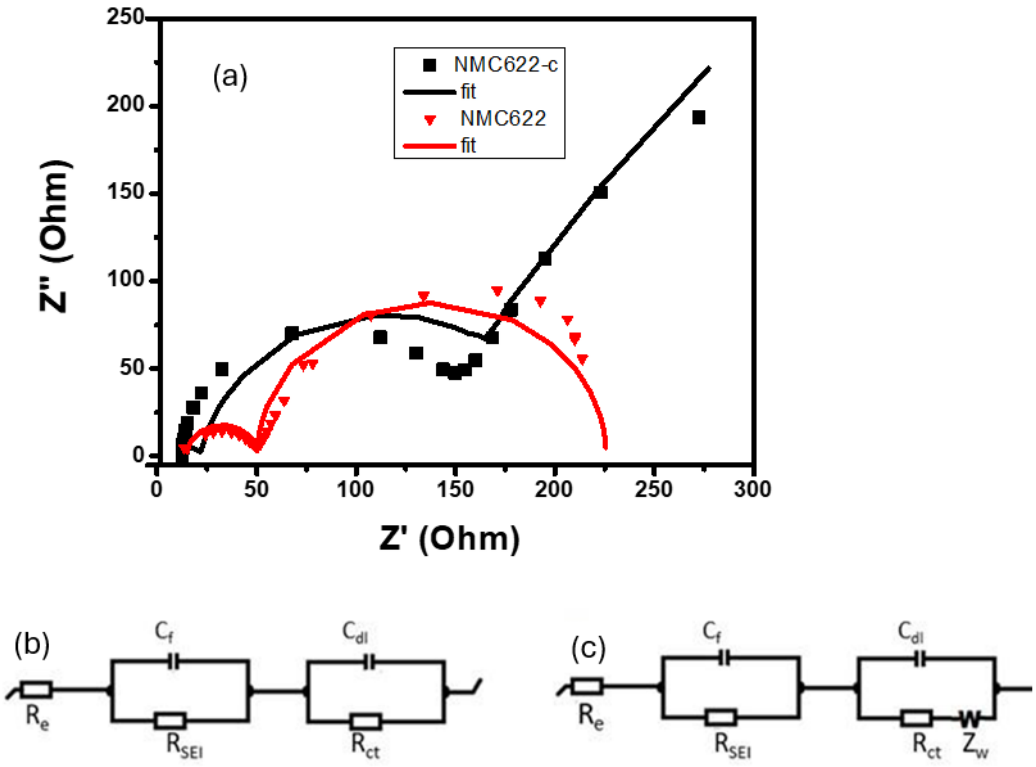


Figure 4-9 Comparative Nyquist plots of cells of (a) NMC622 and NMC622-c and (b, c)Equivalent electrical circuits used to fit NMC622 and NMC622-c, respectively.

Table 4-5 Parameters from fitting EIS Nyquist's plots using the equivalent circuits.

Electrode	R_e (Ω)	C_f (μF)	R_{SEI}(Ω)	C_{dl} (mF)	R_{ct} (Ω)	Z_W($\Omega s^{-1/2}$)
NMC622	13.1±0.3	1680±0.1	118.1±0.5	480±0.03	175.4±0.4	
NMC622-c	14.9±0.3	6.1±0.4	34.9±0.5	2189±0.05	116.8±0.3	29.08±0.3

NMC622 material showed higher $C_{f,}$ R_{SEI} but a lower R_{ct}. These can be expected because the formation of SEI increases with the number of charge-discharge cycling which leads to a slower charge transfer process and in turn a decrease in capacity. The much higher R_{SEI} for the uncoated NMC622 indicates that an SEI layer had already formed on the surface of the material, whereas much less was formed from the surface of the NMC622-c. A marked increase of the R_{ct} shows the non-conducting nature of the SEI layer formed. The NMC622-c cell initially behaved like NMC622, but it had much higher C_{dl} with lower R_{ct} and C_f and R_{SEI} which can be explained by the presence of an oxide layer. Initially the oxide layer seems to be poorly permeable and thus insulating hence the lower capacity that was obtained when first cycled. However, after 50 cycles both the C_{ct} and R_{ct} are lower for the coated material which means the capacitance of the CeO_2 layer changes, as it absorbs more electrolyte it becomes more conductive hence the observed improved capacity that was observed with cycling. The development of the Warburg impedance also shows a significant contribution to lithium ions diffusion which shows that the Li-channels are more active in the coated material which means the CeO_2

layer allows bulk movement of lithium ions hence the improved capacity. The layer improves conductivity and causes a decrease in R_{ct} value. The development of the Warburg impedance indicates that it is a mixed kinetic and diffusion control process which allows for a faster lithium-ion diffusion. The R total after cycling is 225.8 and 166.6 Ω for NMC622 and NMC622-c, respectively. The main contributing element the R_{ct} is much higher for NMC622 suggesting that the coating has suppressed the formation of an SEI layer.

layer.

4.5. Conclusion

Synthesis of NMC622-c was successful as seen from the XRD, the SEM and TEM micrographs which were supported by EDX results. NMC622-c has superior electrochemical properties with a maximum discharge capacity of 165 $mA.hg^{-1}$and a capacity retention of 98 % after 50 cycles. The ultrathin CeO_2 layer stabilised the surface of NMC622 thereby protecting it from parasitic reactions that could lead to capacity loss. The layer helps to curb the loss of capacity during the first cycle by significantly blocking the H2/H3 phase transition, thus improving the first charge capacity loss 36.7 % from the 63.3 % of the NMC622. It enhanced the capacity retention to 98 %. It has a low of between 97-100% except for the first cycle. This overall improvement in structural stability and electrochemical properties makes ceria oxide coating a potential method to use on NMC622 to improve its performance and expand its use in energy thirsty operations and it uses very little ceria.

REFERENCES

1. https://www.scopus.com/term/analyzer.uri?sid=a608fdf7da715155f0fce9e9a41e02dd& origin=resultslist&src=s&s=TITLE-ABS-KEY%28Lithium+ion+batteries+%2c+electric+vehicles%29&sort=plff&sdt=b&sot=b&sl=56&count=8295&analyzeResults=Analyze+results&txGid=45806ae1ff16b563ead83393d9db796f
2. Li, M., Lu, J., Chen, Z. and Amine, K., 2018. 30 years of lithium-ion batteries. *Adv. Mater.*, *30*(33), p.1800561
3. Andre, D., Kim, S.J., Lamp, P., Lux, S.F., Maglia, F., Paschos, O., Stiaszny, B., 2015. Future generations of cathode materials: an automotive industry perspective. *J. Mater. Chem. A*, *3* (13), pp.6709-6732.
4. Armand, M. and Tarascon, J.M., 2008. Building better batteries. *Nature*, *451* (7179), pp. 652-657.
5. Li, H., Li, J., Ma, X. and Dahn, J.R., 2018. Synthesis of single crystal LiNi0. 6Mn0. 2Co0. 2O2with enhanced electrochemical performance for lithium-ion batteries. *J. Electrochem Soc.*, *165*(5), pp.A1038-A1045.
6. Lu, X., Zhang, N., Jahn, M., Pfleging, W., Seifert, H.J., 2019. Improved capacity retention of SiO_2-coated $LiNi_{0.6}Mn_{0.2}Co_{0.2}O_2$ cathode material for lithium-ion batteries. *Appl. Sci.*, *9*(18), p.3671.
7. Mueller-Neuhaus, J.R., Dunlap, R.A. and Dahn, J.R., 2000. Understanding Irreversible Capacity in $Li_xNi_{1-y}Fe_yO_2$ Cathode Materials. *J. Electrochem. Soc*, *147*(10), p.3598.
8. Zhang, H., Xu, J. and Zhang, J., 2019. Surface-coated $LiNi_{0.8}Co_{0.1}Mn_{0.1}O_2$ (NCM811) cathode materials by Al_2O_3, ZrO_2, and $Li_2O_2B_2O_3$ thin-layers for improving the performance of lithium-ion batteries. *Front. Mater.*, *6*, p.309.
9. Myung, S.T., Lee, K.S., Yoon, C.S., Sun, Y.K., Amine, K. and Yashiro, H., 2010. Effect of AlF3 coating on thermal behavior of chemically delithiated $Li_{0.35}[Ni_{1/3}Co_{1/3}Mn_{1/3}]O_2$. *J. Phys. Chem. C*, *114*(10), pp.4710-4718.
10. Ryu, H.H., Park, K.J., Yoon, C.S. and Sun, Y.K., 2018. Capacity fading of Ni-rich Li $[Ni_x Co_y Mn_{1-x-y}] O_2$ ($0.6 \leq x \leq 0.95$) cathodes for high-energy-density lithium-ion batteries: bulk or surface degradation? *Chem. Mater.*, *30*(3), pp.1155-1163.
11. Sun, H.H., Ryu, H.H., Kim, U.H., Weeks, J.A., Heller, A., Sun, Y.K. and Mullins, C.B., 2020. Beyond doping and coating: prospective strategies for stable high-capacity layered Ni-rich cathodes. *ACS Energy Lett.*, *5*(4), pp.1136-1146.
12. Kondrakov, A.O., Schmidt, A., Xu, J., Geßwein, H., Mönig, R., Hartmann, P., Sommer, H., Brezesinski, T. and Janek, J., 2017. Anisotropic lattice strain and mechanical degradation of high-and low-nickel NCM cathode materials for Li-ion batteries. *J. Phys. Chem. C*, *121*(6), pp.3286-3294.

13. Li, W., Reimers, J.N. and Dahn, J.R., 1993. In situ x-ray diffraction and electrochemical studies of $Li_{1-x}NiO_2$. *Solid State Ion.*, *67*(1-2), pp.123-130.
14. Arai, H., Okada, S., Ohtsuka, H., Ichimura, M. and Yamaki, J., 1995. Characterization and cathode performance of $Li_{1-x}Ni_{1+x}O_2$ prepared with the excess lithium method. *Solid State Ion.*, *80*(3-4), pp.261-269.
15. Min, K., Kim, K., Jung, C., Seo, S.W., Song, Y.Y., Lee, H.S., Shin, J. and Cho, E., 2016. A comparative study of structural changes in lithium nickel cobalt manganese oxide as a function of Ni content during delithiation process. *J. Power Sources*, *315*, pp.111-119.
16. Patel, R.L., Xie, H., Park, J., Asl, H.Y., Choudhury, A. and Liang, X., 2015. Significant Capacity and Cycle-Life Improvement of Lithium-Ion Batteries through Ultrathin Conductive Film Stabilized Cathode Particles. *Adv. Mater. interfaces*, *2*(8), p.1500046.
17. Wu, F., Wang, M., Su, Y., Bao, L. and Chen, S., 2009. Surface of $LiCo_{1/3}Ni_{1/3}Mn_{1/3}O_2$ modified by CeO_2-coating. *Electrochim. Acta*, *54*(27), pp.6803-6807.
18. Liu, K., Yang, G.L., Dong, Y., Shi, T. and Chen, L., 2015. Enhanced cycling stability and rate performance of $Li[Ni_{0.5}Co_{0.2}Mn_{0.3}]O_2$ by CeO_2 coating at high cut-off voltage. *J. Power Sources*, *281*, pp.370-377.
19. Patel, R.L., Park, J. and Liang, X., 2016. Ionic and electronic conductivities of atomic layer deposition thin film coated lithium-ion battery cathode particles. *RSC Adv.*, *6*(101), pp.98768-98776.
20. Gao, Y., Patel, R.L., Shen, K.Y., Wang, X., Axelbaum, R.L. and Liang, X., 2018. Boosting the electrochemical performance of $Li_{1.2}Mn_{0.54}Ni_{0.13}Co_{0.13}O_2$ by atomic layer-deposited CeO_2 coating. *ACS Omega*, *3*(1), pp.906-916.
21. Shaju, K.M., Rao, G.S. and Chowdari, B.V.R., 2002. Performance of layered $Li(Ni_{1/3}Co_{1/3}Mn_{1/3})O_2$ as cathode for Li-ion batteries. *Electrochim. Acta*, *48*(2), pp.145-151.
22. Periasamy P.,Kalaiselvi, N., and Kim, H.S.ICAL, E., 2007. High voltage and high capacity characteristics of $LiNi_{1/3}Co_{1/3}Mn_{1/3}O_2$ cathode for lithium battery applications. *Int. J. Electrochem. Sci*, *2*, pp.689-699.
23. Xin, F., Zhou, H., Zong, Y., Zuba, M., Chen, Y., Chernova, N.A., Bai, J., Pei, B., Goel, A., Rana, J. and Wang, F., 2021. What is the Role of Nb in Nickel-Rich Layered Oxide Cathodes for Lithium-Ion Batteries?. *ACS Energy Lett.*, *6*(4), pp.1377-1382.
24. Julien, C.M. and Mauger, A., 2018. In situ Raman analyses of electrode materials for Li-ion batteries. *AIMS Mater. Sci.*, *5*(4), pp.650-698.
25. Yang, F., Wang, D., Zhao, Y., Tsui, K.L. and Bae, S.J., 2018. A study of the relationship between coulombic efficiency and capacity degradation of commercial lithium-ion batteries. *Energy*, *145*, pp.486-495.

Chapter 5

The effects of microwave-assisted surface-coating and doping with a little amount of CeO_2 on the electrochemical performance of $LiNi_{0.8}Mn_{0.1}Co_{0.1}O_2$ (NMC811)

5. Introduction

In this chapter we report on microwave assisted synthesis of NMC 811 treated with CeO_2.

5.1. Introduction to $LiMn_{0.8}Ni_{0.1}Co_{0.1}O_2$

Foreseeable depletion of fossil fuels, their mounting contribution to environmental pollution, and the booming sales and future of portable and wearable electronics have driven vast research around rechargeable lithium-ion batteries (LIBs)[1,2]. A few cathode materials for LIBs have been commercialised but some such as NMC still need to be further refined and improved to expand their application. The cathode materials, NMC, have a general chemical formula $LiNi_xMn_yCo_xO_2$ ($x + y + z = 1$). They exhibit layered structure and possess a theoretical capacity of about 270 $mAhg^{-1}$; however, practically, only a percentage of the capacity is accessible. The nickel rich NMC material where ($x \geq 0.6$) are front runners in energy thirsty applications such as electric vehicles and grid energy storage systems (ESS) because

of their high practical specific energy, relatively lower cost, and their more environmentally friendly outlook. Efforts have therefore been concentrated on further improving the energy density and operating voltage to satisfy the demand and calls for electric vehicles. Like other Ni-rich NMCs, $LiNi_{0.8}Mn_{0.1}Co_{0.1}O_2$ (NMC811) has poor cycling stability including over 20% capacity loss on its very first charge-discharge cycle, voltage fading during cycling and in storage; it is unstable in environmental conditions and in ambient air. These are mostly intrinsic degradation flaws brought about by residual Li during synthesis and high cationic mixing by Li^+ and Ni^{2+} due to their almost similar radii size of 0.074 nm and 0.069 nm, respectively. These impede on Li movement during intercalation and deintercalation. Dissolution of the transition metals into the electrolyte, irreversible phase transitions and limited operating voltage are other causes of its problems as mentioned in section 2.5.

Surface coating and bulk doping with other electrochemically inactive atoms has been done to change the lattice of the cathode materials, reinforce the structure and thus reduce degradation. In our other work we were able to change the electrochemical behaviour for the first cycle which affected performance of NMC622 by surface coating with CeO_2. The modification to the surface also led to a reduction in voltage decay at high potentials suggesting preservation of energy. Xin et. al. has reported similar work where NbO_y treatment was used to modify the lattice of or coat NMC811.[3] They were able to show that Nb can diffuse into the lattice when coating

temperature conditions vary. Their electrochemical studies revealed the best benefit of improved capacity retention and rate performance and extended cycling when Nb had infiltrated the structure. Other atoms previously used as dopants or their oxides as coatings include Zr, Al, B and Ce. These led to a decrease in cation mixing and stabilisation of the structure. In this section we report on the effect of coprecipitated Ce in NMC811 and surface coating with CeO_2 and the effect of Metal coatings have also been used to achieve the same thing.

5.2. Experimental

Two pristine NMC811 were prepared as previously summarised in Figure 3-2. Co-precipitation method was used to prepare $Ni_{0.8}Mn_{0.1}Co_{0.1}(OH)_2$, a precursor for pristine NMC811 (NMC811-p) and microwave treated NMC811(NMC811-p_MW). The analytical reagents $Ni(NO_3)_2$·6H2O, $MnSO_4$·H_2O and $Co(NO_3)_2$·$6H_2O$ were weighed according to the metal molar ratio of 8:1:1,respectively. They were combined and dissolved in degassed deionized water to form a 2 M solution by total mole fraction of the metal salts and kept aside. Another solution of 1 M NH_4OH was prepared and added to a laminar flow reactor and heated to 60 °C. A nitrogen blanket was created over the solution. A complexing buffer was also prepared using 4 M NaOH as the precipitating agent and 2 M NH_4OH as the chelating agent. The metal salts' solution and the complexing buffer were then pumped into a rapidly whirling laminar flow reactor at the rate of 0.5 ml/min and 0.15 ml/min, respectively. The pH value was maintained between pH11$\pm$ 0.5 by

adjusting the flow of NaOH. This mixture was allowed to age for 19 h while under nitrogen at 60 °C. Finally, the precipitated $Ni_{0.8}Mn_{0.1}Co_{0.1}(OH)_2$ precursor was filtered out, repeatedly washed with distilled water and then vacuum dried at 80 °C for 12 h. The dry $Ni_{0.8}Mn_{0.1}Co_{0.1}(OH)_2$ and LiOH were weighed according to the mole ratio of 1:1.05 then ground into a uniform mixture in an agate mortar and pestle. The mixture was then pre-calcined at 500 °C for 5 h. cooled, and ground into a powder. One portion of the hydroxide powder was further calcined for 16 h at 750 °C in an oxygen-blanket atmosphere in a tube furnace to form pristine NMC811, (NMC811-p). The other portion was microwave-treated at 600 W for 20 min before further calcining at 750°C for 16h in an oxygen-blanket atmosphere in a tube furnace to form microwave-treated pristine NMC811 (NMC811-p_MW).

In the same way used to prepare NMC811-p and NMC811-pMW, Ce-doped NMC811(NMC811-d), and NMC811-d_MW were prepared by the co-precipitation method from the precursor $Ce_\delta(Ni_{0.8}Mn_{0.1}Co_{0.1})_{-\delta}(OH)_2$ by adding weighed $Ce(NO_3)_3 \cdot 6H_2O$ to the metal solutions as represented by Figure 3-3 from Chapter 3.

A portion of NMC811-p was coated in a similar way to that done for NMC622 in Chapter 3 to yield NMC811-c and NMC811-cMW, Figure 3-4.

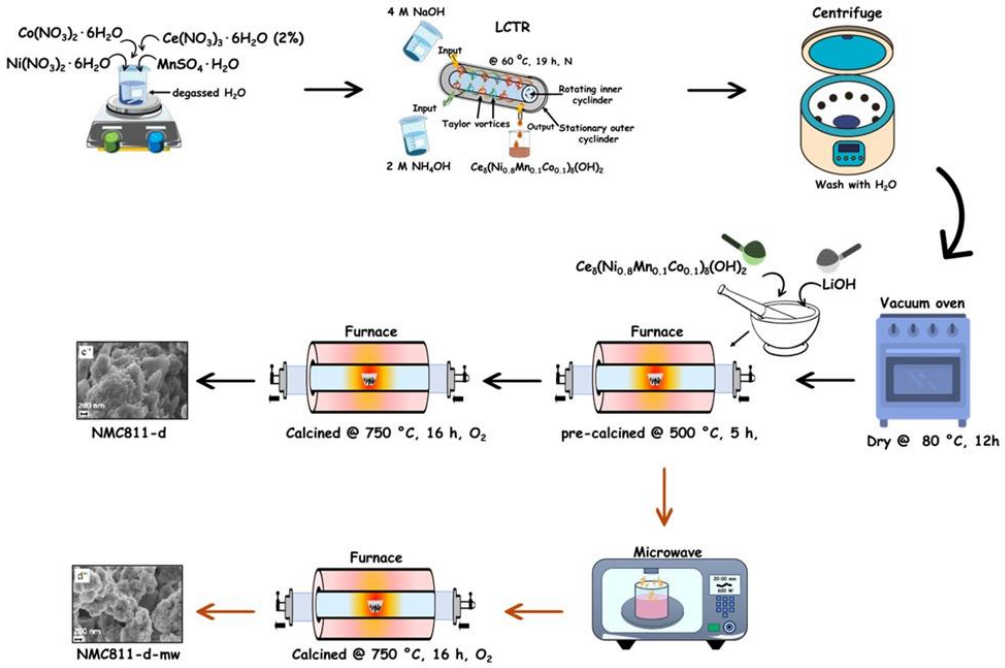


Figure 3-3 Schematic of the synthesis of NMC811-d and NMC811-d_MW.

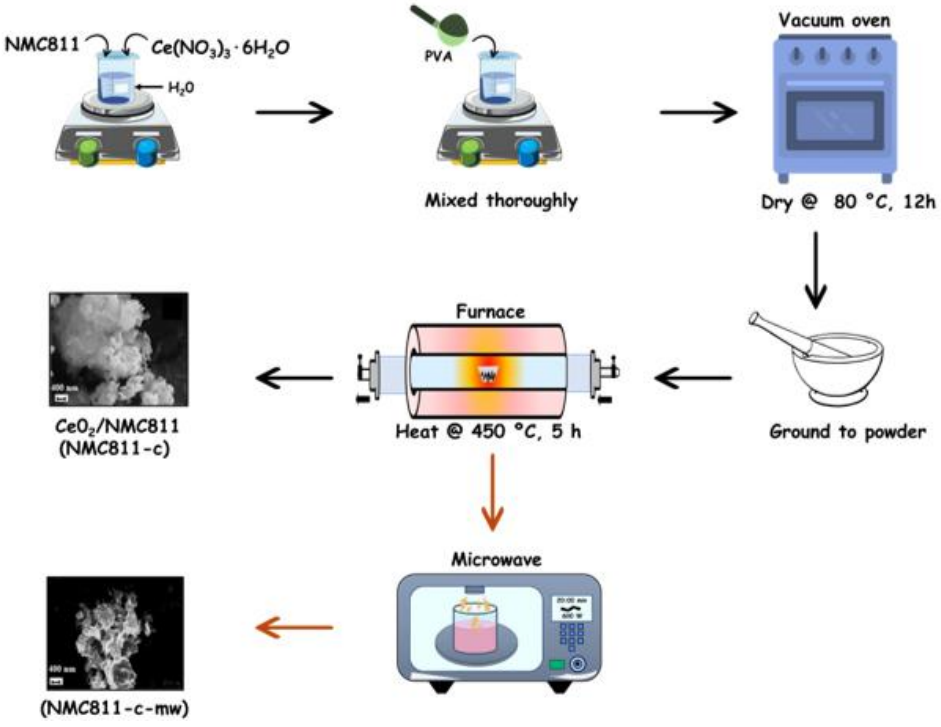


Figure 3-4 Schematic of the synthesis of NMC811-c and NMC811-c_MW

5.2.1. Characterization of the materials

The crystal structures were characterised by Horiba Jobin-Yvon LabRAM HR Raman spectrometer equipped with an Olympus BX41 microscope attachment was used to obtain the Raman spectra, scanning electron microscopy (SEM) using Zeiss high vacuum SEM for the surface topography and morphology and energy dispersive spectrometer mapping for the distribution of the elements, transmission electron microscopy (TEM) to study the particle size and thickness of the coatings and high resolution microscopy(JEM 2100) to further obtain the lattice spacings, and X-ray diffraction (XRD) was investigated using a Bruker D2 diffractometer 580 equipped with Cu Kα radiation (λ = 1.54178 Å and scanned within range 10º-90º at a scanning rate of 1.7 º/min to analyse the crystal phase structure and crystallographic nature of material. Thermal gravimetric analysis (TGA) was used to evaluate the effect of temperature on the material under nitrogen.

5.2.2. Electrochemical measurement

Electrochemical tests were carried out using R2032 coin cells. Typically, to fabricate cathode electrodes from an 8:1:1 mass ratio of the LIB cathode materials (NMC811-no laminar, NMC811, NMC811_MW, NMC811-c, NMC811-d and NMC811-d_MW), polyvinylidene fluoride (PVDF) and carbon black were used. First the PVDF binder was placed in an agate mortar and N-Methyl pyrrolidine (NMP) was added as the solvent. Secondly the cathode material and carbon were mixed then added to the combination in the mortar and gently mixed into a slurry. The slurry was evenly applied

onto an aluminium foil current collector using a coating machine. The coated sheet was placed in a vacuum oven at 120 ºC overnight to dry before calendaring. The coated electrode sheet was then cut into 12 mm diameter discs and transferred to an argon-filled MBraun glovebox for cell fabrication. The R2032 coin cells were assembled using the coated cathode discs, lithium foil discs as anode, 1M $LiPF_6$ in EC/DEC/DMC (1:1:1 volume ratio) as the electrolyte and micro-porous polypropylene Celgard H1612/16 µm as the separator. The voltage range between 2.8 and 4.2 V was used to test the batteries. The following electrochemical measurements were carried out; Cyclic voltammetry (CV), galvanostatic charge-discharge cycling (GC-D) and electrochemical impedance spectroscopy (EIS) on a BioLogic system (BCS-8xx series). BT-Lab program was used for data acquisition and analysis.

5.3. Results and discussion

5.3.1. XRD

Figure 5-1 shows the XRD patterns for the samples under study. The diffraction patterns have sharp peaks which indicate the periodic crystalline nature of all the compounds. Generally, all prepared samples have the parent pattern of a layered hexagonal structure in the R-$\bar{3}$m space group indexed for α-$NaFeO_2$ which shows that Ce doping, coating and microwave treatment do not alter the structure of the bulk NMC and thus the NMC can be expected to retain its properties as a cathode material. Peaks 108/110 and 006/110 appear as split doublets which further proves that the layered materials were highly crystalline. The expanded area shows that there is a

peak shift of peak (003) and other peaks. However, a calculation of (003) + (104)/(003) shows that the shift is not equal for all materials, clearly indicating that different new samples were made. For the Laminar synthesised samples, those in which Ce was coprecipitated have the peak shifts to lower 2θ degrees because the Ce^{3+} ions with its larger radius have replaced some of the transition metal ions in the bulk NMC structures.

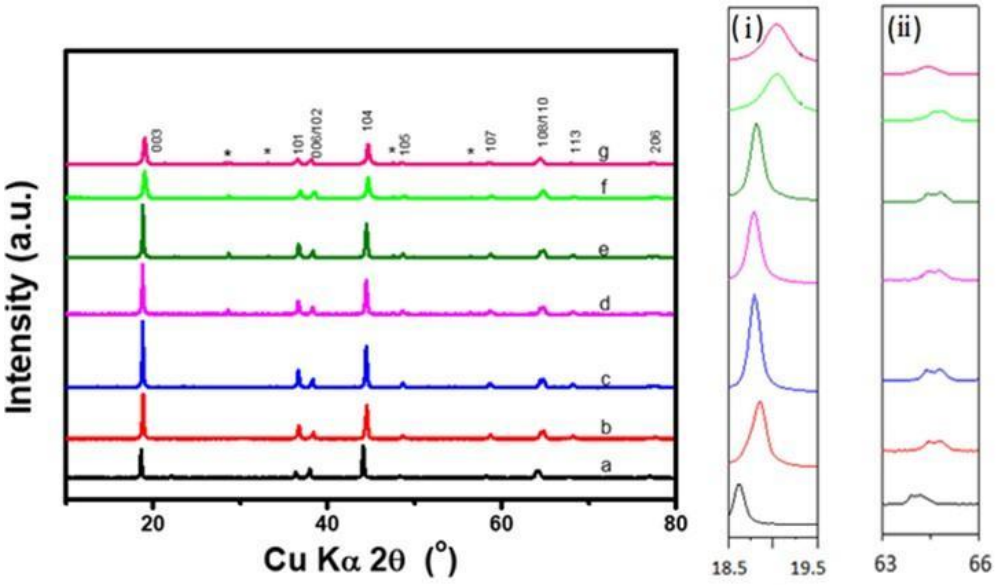


Figure 5-1 XRD pattern of the prepared NMC811 powder materials and the corresponding partial enlargement of peaks (i)(003) and (ii)(108) and (110)

Also, visible and marked with asterisk (*) are the fingerprints of CeO_2 on NMC811-c, NMC811-c_MW, NMC811-d and NMC811-d_MW. The strongest CeO_2 signal at around 28.6° from NMC811-c is more unstructured and weaker than from all the other samples in which this peak and corresponding peaks CeO_2 are relatively sharp. This suggests a lower degree of perfection of the crystals or even amorphous nature for the CeO_2

on NMC-c since crystalline CeO_2 is highly diffractive. Interestingly, subjecting NMC811-c to microwave irradiation seems to cause this amorphous coating to crystallise as the peak can be seen to be sharper. It is interesting to still see the fingerprint even in the coprecipitated samples, which can indicate that the Ce did not all go into the formation of the precursor hydroxide material product, but some was still available to independently form the CeO_2 responsible for the impurities seen on the pattern. This phenomenon has been documented before for Nb in NMC811 where samples calcined at high temperature still bore the impurities of niobium oxide which were identified on the xrd pattern. [4]

The cationic radii of Ni^{2+} is close in size to that of Li^{+} and with Ni-rich NMC, the two tend to mix and swop positions.[5] It is also known that nickel rich NMC samples tend to suffer more from catanionic mixing than samples in which it is lower.[6] The ratio of the intensity of (003) to (104) in hexagonal layered structures indicates the degree of cation mixing where a ratio $I_{(003)}$ / $I_{(104)}$ > 1.2 indicates considerable cation mixing.

Table 5-1 Intensity ratios, $I_{(003)}$ / $I_{(104)}$ and ($I_{(006)}$ / $I_{(102)}$)/ $I_{(101)}$ for the different cation materials

Sample	$\frac{I_{(003)}}{I_{(104)}}$	$\frac{I_{(006)} + I_{(102)}}{I_{(101)}}$
No laminar	0.87	2.10
NMC811-p	1.37	0.89
NMC811-p_MW	1.62	0.84
NMC811-d	1.44	0.72
NMC811-d_MW	1.57	0.65
NMC811-c	1.32	0.61

Table 5-1 summarises the ratio of intensities $I_{(003)}/ I_{(104)}$ and $(I_{(006)} / I_{(102)})/ I_{(101)}$. The 811-no laminar sample which was prepared the conventional way has its most intense peak as (104) and thus results in a subunit ratio of intensity of $I_{(003)}/ I_{(104)\ 4)}$, this means the 811-no laminar has the highest level of cation mixing. This observation suggests that the speed and style of mixing is one of the important determinants of the degree of cationic mixing. Only one of the samples studies has $I_{(003)} / I_{(104)}$ less than 1.2, which proves that most samples have low cationic mixing. The samples in decreasing order of the ratio are NMC811-p_MW > NMC811-d_MW > NMC811-d > NMC811-p > NMC811-c > No laminar. Another observation is that samples synthesised without microwave assistance have lower $I_{(003)}/I_{(104)}$ ratio of intensity and lower values of $(I_{(006)}/I_{(102)})/ I_{(101)}$ than their microwave treated counterparts. These suggest microwaves affect the alignment of the TM in the crystal to yield the best hexagonal ordering and least cation mixing.

5.3.2. Scanning electron microscopy (SEM)

The morphology of the particles was studied using scanning electron microscopy (SEM). The SEM images of the different NMC811 samples are as shown in Figure 5-2. The powders are made up of secondary particles with a nondescript shape built with aggregated primary particles making up different sizes and shapes of the larger aggregates. The primary particles are of different sizes ranging from 100-500 nm.

Some have cloud-like and fluffy looking surfaces while others have smooth surfaces. Images in Figure 5-2 c&d of NMC811-d and NMC811-d_MW, respectively show lots of tiny particles and some elongated plate-like

smooth structures. The other samples don't show this shape. This difference in shape could partly be due to the conditions during synthesis.

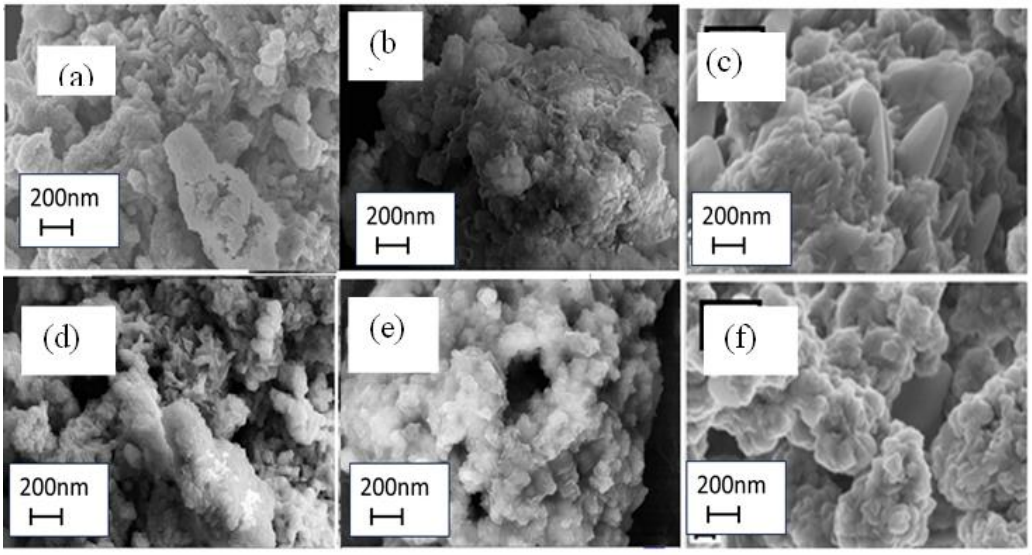


Figure 5-2 Comparison of SEM images of : (a) NMC811-p, (b) NMC811-p_MW, (c) NMC811-d, (d) NMC811-c, (e) NMC811-c_MW and (f) NMC811-d_MW.

Samples NMC811-p and NMC811-p_MW, show some flaky specks on the surface. Nickel-rich NMC are known to readily react in air and result in the formation of lithium compounds such as Li_2CO_3, LiOH and other lithium containing compounds that foul the surface. These may be the ones seen as flaky specks. In contrast, the surfaces of NMC811-c and NMC811-c_MW have a smooth surface that shows that a coat has been applied. The NMC811-d and NMC811-d_MW also have smooth surfaces.

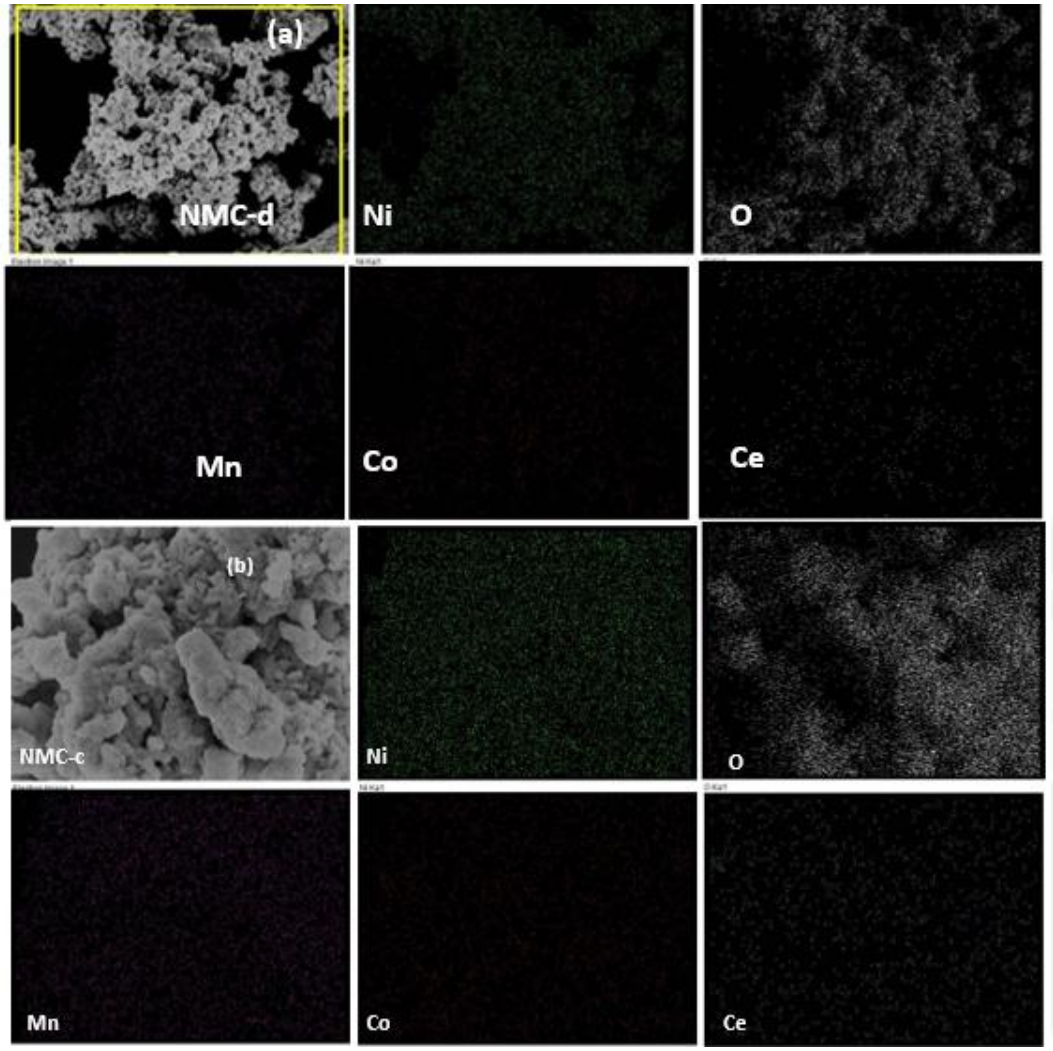


Figure 5-3. Typical EDS mapping of Ni, MN, Co, O and Ce for (a)NMC811-d and (b) NMC 811-c

To further establish composition whether Ce was successfully applied as a coating and doping EDS was obtained as indicated by the EDS images shown in Figure 5-3. The Ce nanoparticles are found more on the surface for NMC811-c than on NMC811-d giving an illusion of higher Ce density on the former. The other observation is that Ce was evenly distributed on the surface of NMC811-c.

5.3.3. Transmission electron microscopy (TEM)

Figure 5-4 displays the HRTEM images of NMC811-c and NMC811-d. Typically, the NMC811-c and NMC811-c_MW showed the presence of the coating with a thickness of approximately 5 nm. Although NMC811-d had a smooth surface when observed under SEM, it does not have a coating, as seen in the micrograph.

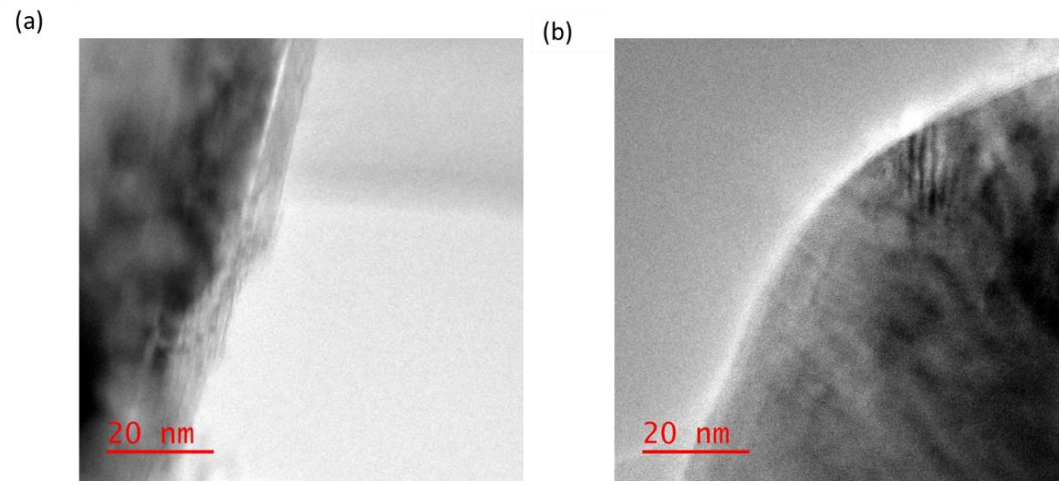


Figure 5-4. HRTEM images of (a) NMC811-c and (b) NMC811-d at high magnification.

High resolution electron microscopy coupled with X-ray spectroscopy was further employed on the NMC811-c and NMC811-d. The EDS spectrum that still revealed the presence of Ce, further establishing that both the coating and the doping were successfully done. HRTEM was further used to study the surfaces of the particles and the areas in the enclosed rectangles were expanded for line profile imaging which revealed the d-spacing between the lines of 0.21 and 0.24 nm for NMC811-c and NMC811-d, respectively.

Another interesting observation is that in both samples of NMC811-c and NMC811-d, areas showing orderly arrangement could be seen and some with blurred areas which were attributed to cationic disorder are both present. Also, looking deeper into at areas with cationic order different patches show different patterns, the layered structure, marked with a red arrow which was expected for a crystal structure with of R$\underline{3}$m space group, and a different microstructure marked with a blue arrow. The phenomenon of nickel-rich NMC material structure exhibiting this multi-phase structures has been reported before which is normally accompanied by cation disorder and or degradation of the material.[7]

Raman spectroscopy was used to further study the structure of the NMC powders and to see the vibrational modes of the M-O bonds. NMC 811 has a D_{5d} symmetry which typically has $r = 2A_{2u} + 2t_{2u} + A_{1g} + E_g$ and only the latter two are Raman active.[8] Figure 5-5 shows the Raman spectra of the NMC compounds. Julien and Mauger showed how the shape of Raman spectra changes depending on the crystal phases that exist at the time of capturing. The intensity and sharpness of the A_{1g} and the E_g modes also depends on the state of degradation.

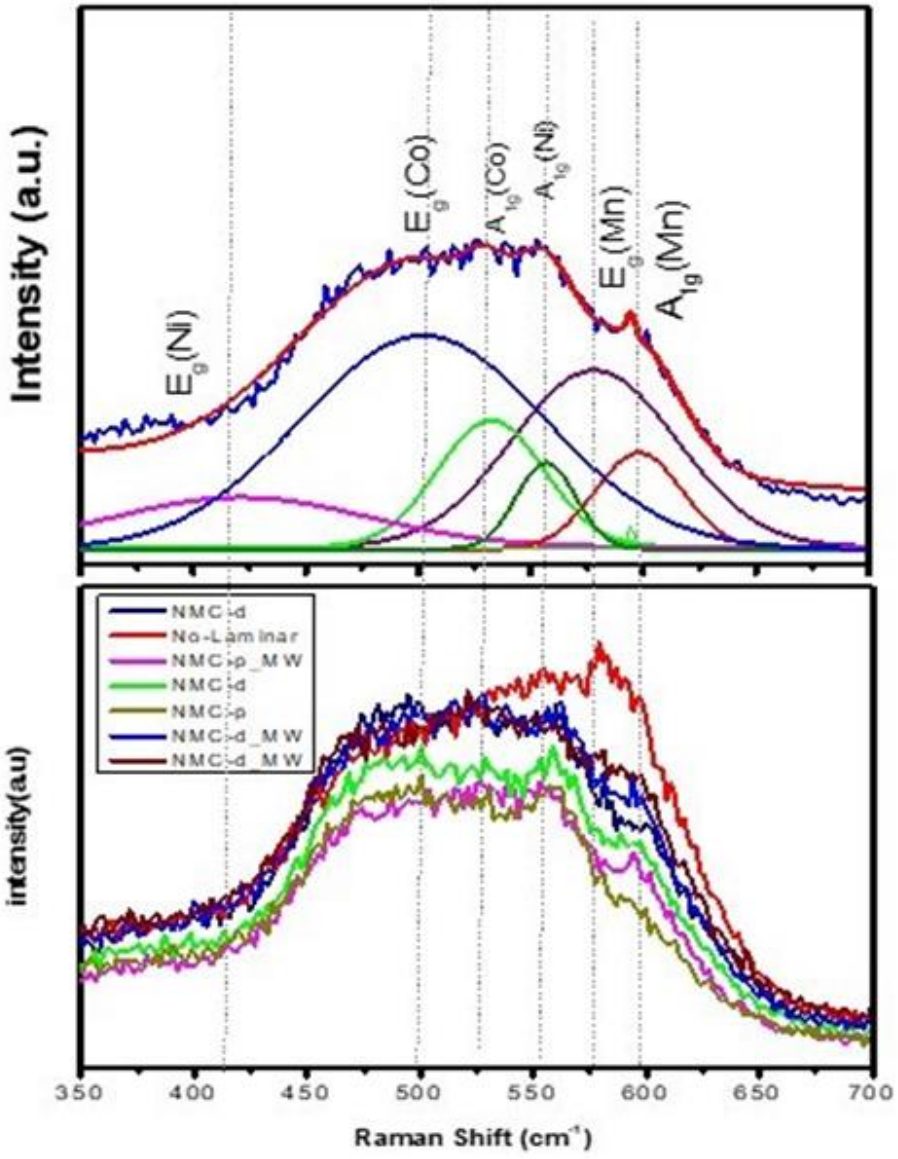


Figure 5-5 Raman spectra of the NMC811-d_MW with its deconvoluted components and the overlain spectra of the other NMC 811 powders.

It is therefore not surprising to see the spectra without clear peaks before deconvolution. These modes originate from the M-O vibrations and the symmetric stretching and bending origin. For the metals Ni, Mn and Co the modes overlap, some are broad and difficult to discern without deconvoluting. Thus, for the three primary metals a total of six vibrational

modes were found in this window which can only be seen on the spectrum that was deconvoluted using Gaussian resolution fit.

5.3.4. Thermogravimetric analysis

Thermogravimetric analysis was also used to characterise the cathode materials and quantify the amount of impurities on the surface. Contaminants formed on the surface of the material can originate from both storage and production stages and may vary depending on the reagents used.

Sicklinger et al. mimicked long storage conditions in ambient atmosphere and were able to show that unprotected cathode material is prone to moisture and CO_2 attack and they showed that dry material was less contaminated than wet material.[9] The cathode materials were stored for longer than three months at room temperature to mimic what could happen in a real-life situation where the material might not be stored in dry, oxygen free conditions and to study the effect of coating and doping on the material.

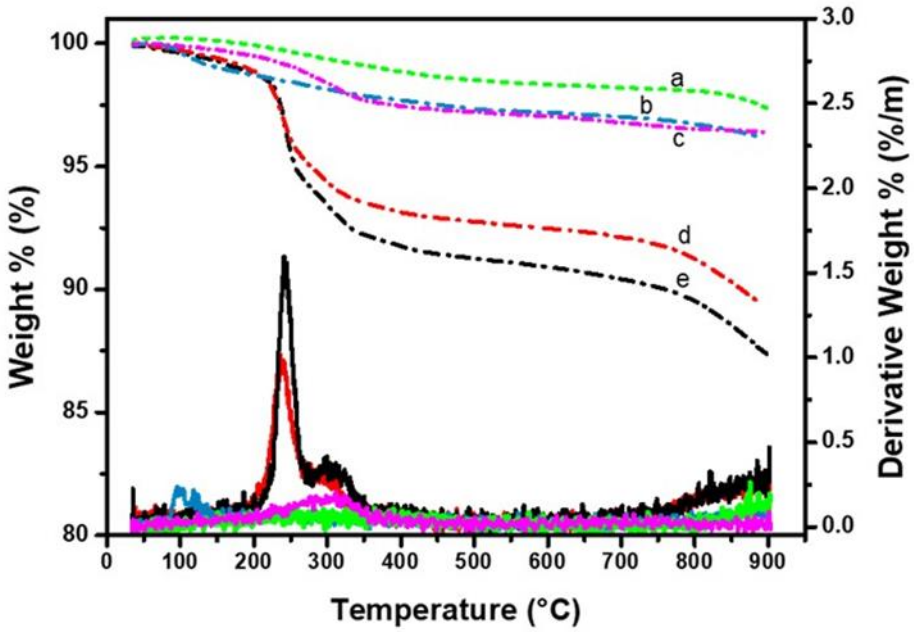


Figure 5-6 TGA of (a) 811-d_MW, (b)811-d, (c) 811-c, (e)811-p_MW and (f) 811-p and their corresponding mass signals curves in solid lines for 10K/min temperature ramp and 25-900 ^{0}C.

Figure 5-6 shows TGA-DTA analyses of NMC811-p and NMC811-p_MW showing their weight loss during heating from 35-930 °C under nitrogen with a flow rate of 20 ml/min. Generally, if impurities on metal oxides can undergo exothermic reaction, energy will be released as heat when a higher state of disorder is achieved within the system which will be seen by gain in temperature, in contrast, if an endothermic reaction occurs, the system will absorb energy and a drop in temperature will be observed. Three distinct areas that can be identified from the TGA curves. First is area I, from 30-125 °C, then area II which has been shaded is yellow between 125- 430 °C and lastly 750 °C upwards as area III. In area I, there is a small decrease in mass, ~0.5%, from around 70-100 °C which can be identified even on the derivative mass curve by the slight movement from the baseline. This loss

has been described before as due to loss of desorption water. Then in area II there is a substantial decrease that starts at around 136 °C and peaks at 242 °C with a hump at 300 °C and an even smaller one at 389 °C which accounts for a decrease in mass by 6.7 and 7.83% for NMC811-p and NMC811-p_MW, respectively. The mass loss has been assigned to the loss water at 235 °C, CO_2 at 305 °C and O_2 at 390 °C. The latter two are typical for the presence of Li_2CO_3 on the surface. Since the starting materials did not contain any carbonate then this can only be explained as Li_2CO_3 formed due to left over $LiOH.\cdot H_2O$ which can react with CO_2 in air to form Li_2CO_3. When annealing Ni rich NMC powders, they tend to have this loss in Li. All samples lack a footprint due to CeO_2 which would show as gradual mass loss between 53-800 °C with a peak at 500°C is not present.[10] This could be due to the low amount of CeO_2 present. Microwave treatment seems to also engineer material that is resistant to the formation of contaminants on the surfaces seen by the slightly less mass losses than their microwave untreated counterpart.

5.4. Electrochemical studies

5.4.1. Cyclic Voltammetry

Figure 5-7 compares the CV profiles of the NMC811 samples at first and second cycles. With the pristine samples (Figure 5.8a&b), both NMC811-p and NMC811-p-MW showed similar behaviour where the 2nd cycle ($\triangle$E = 0.19 V) showed better kinetics than the 1st cycle ($\geq$E = 0.49 V). With the coated samples (Figure 5.7b&c), the microwaved sample showed better

kinetics than the unmicrowaved sample: NMC811-c showed the first cycle (≥E = 0.30 V) with the 2nd cycle (≥E = 0.26V) , while the NMC811-c-MW showed ≥E = 0.28 V while the 2nd cycle showed ≥E = 0.17V. However, the doped samples (Figure 5.7e&f) showed similar kinetics (≥E H 0.21 V) for both 1st and 2nd cycles. These results confirm that both coating and doping, with and without microwave irradiation, eliminated the H2/H3 phase transition.

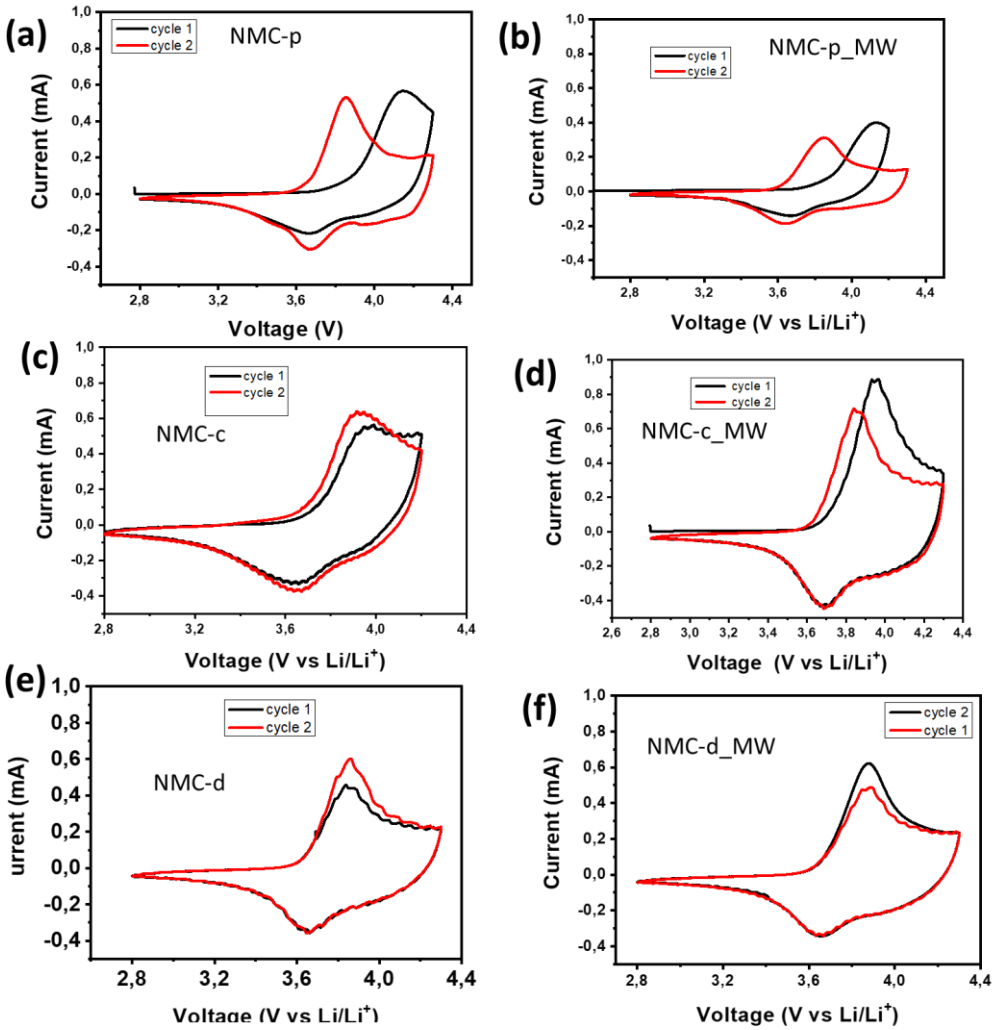


Figure 5-7. Comparative CVs of the NMC811 samples: (a) NMC811-p, (b)NMC811-p-MW, (c) NMC811-cv, (d) NMC811-c-MW, (e) NMC811-d, and (f) NMCV811-d-MW.

Table 5-2 The summary of CV potentials for NMC811 samples.

Compound	$E_{1/2}$ potential (V vs Li/Li^+)			
	Cycle number	Oxidation	Reduction	$\triangle E_p$
NMC811-p	1	4.15	3.66	0.49
	2	3.93	3.66	0.19
NMC811-p_MW	1	4.13	3.63	0.53
	2	3.85	3.67	0.19
NMC811-d	I and 2	3.86	3.64	0.21
NMC811-d_MW	1 and 2	3.88	3.65	0.23
NMC811-c	3.96	3.96	3.66	0.30
		3.92	3.66	0.26
NMC811-c_MW	1	3.96	3.68	0.28
	2	3.85	3.68	0.17

5.4.2 Charge-discharge properties

The galvanic charge-discharge curves were run between 2.8-4.3 V at a constant current rate of 0.1 C-rate as shown in Figure 5-8. The low initial charge capacities indicate slow activation of the material which results in a very inefficient first cycle for most of the powders.

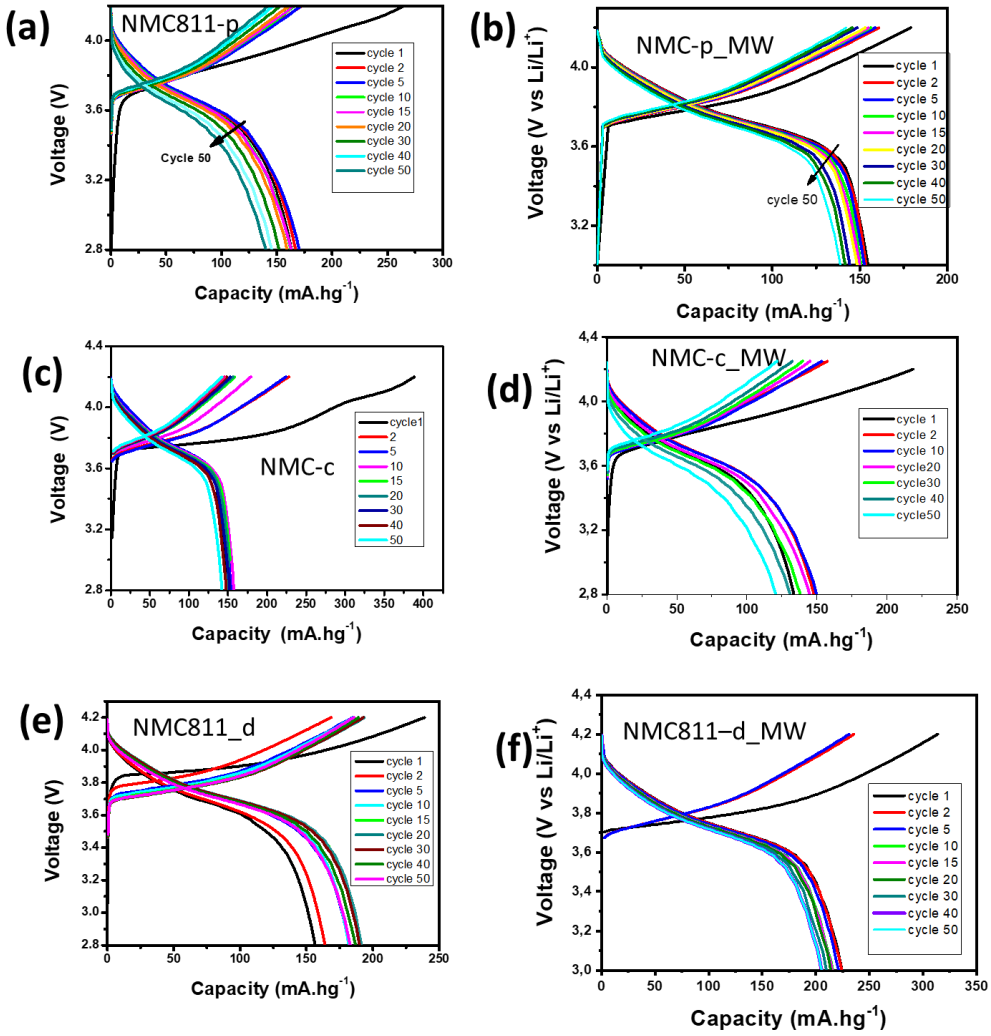


Figure 5-8. Comparative Charge-discharge voltage profiles showing 1st, 2nd, 5th, 10th, 20, 30th 40th and 50th cycle at 0.1C rate for: (a) NMC811-p, (b)NMC811-p-MW, (c) NMC811-cv, (d) NMC811-c-MW, (e) NMC811-d, and (f) NMCV811-d-MW.

The initial discharge capacity is not necessarily the highest discharge capacity obtained for each sample showing slow formation or activation of the charging process. Table 5-3 therefore presents information of the initial discharge capacities and the maximum initial capacity for each cathode of the NMC powders.

Table 5-3 Initial and maximum discharge capacities of the NMC powders.

Compound	Discharge Capacity (mAh g^{-1})	
	Initial	Maximum
NMC811-d	156	192
NMC811-d_MW	220	224
NMC811-p	170	170
NMC811-p_MW	153	154
NMC811-c	152	157
NMC811-c_MW	133	150

The highest capacities are for the Ce doped samples. This agrees with the XRD information that showed better lithium diffusion channels for the NMC811-d sample and the live profile information where the NMC811-d had much bigger d-spacing and would therefore be expected to give more efficient mobility of Li-ions during intercalation and consequently higher capacities would result. Compared with the NMC811-p, the coating resulted in the lowering of the discharge capacity. Although Ce is known to elicit improved conductivities, the added phase boundaries still pose some level of resistivity which resulted in lower capacities.

5.4.3 Cycling stability and coulombic efficiency

Figure 5-9 summarised the cycling and coulombic efficiency of the NMC811 samples studied in this work. The results showed the following: (i) the Coulombic efficiency was the same for all, and (ii) all the other samples (with the exception the NMC811-d) showed slight capacity degradation with cycling. The capacity retention is summarised in Table 5-4.

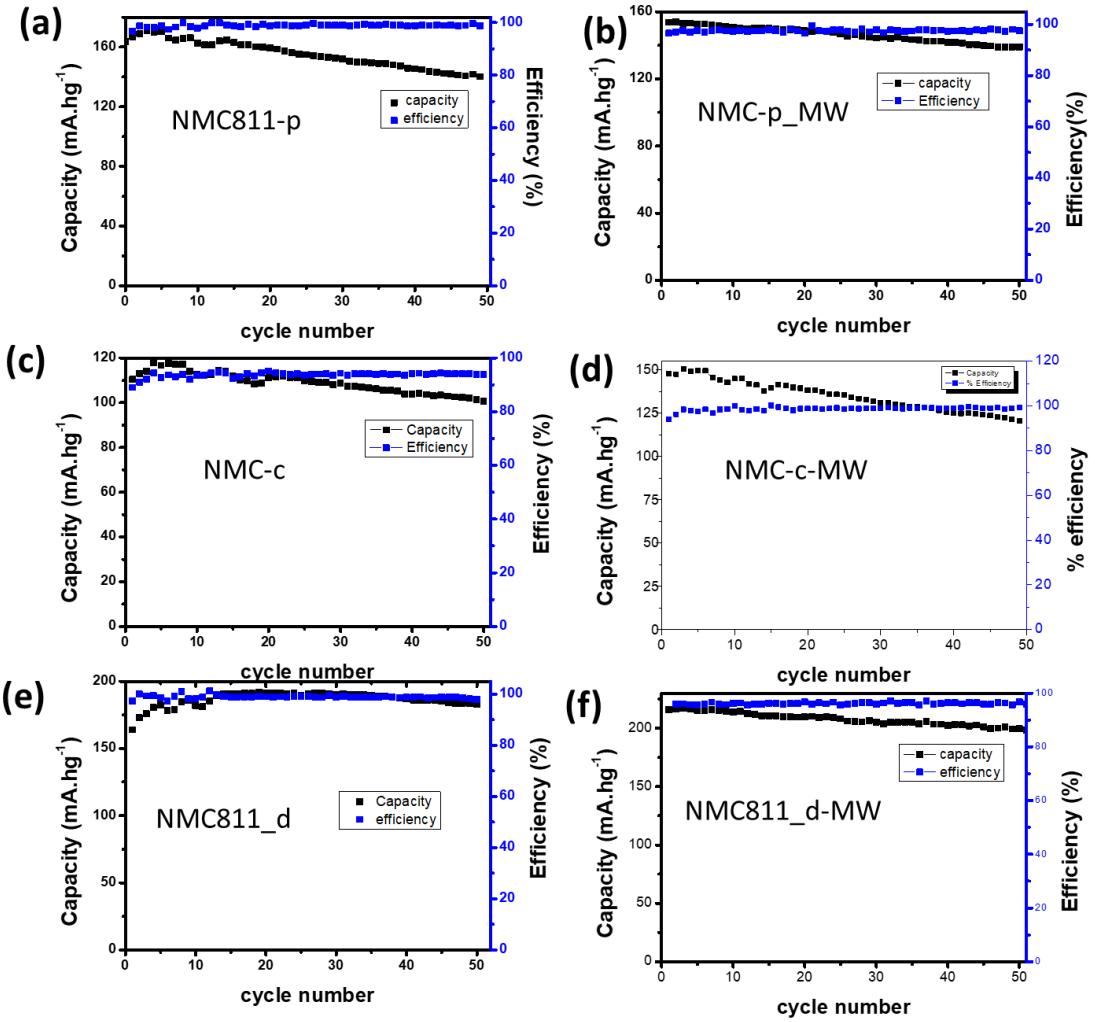


Figure 5-9 Capacity retention and coulombic efficiency for (a) NMC811-p, (b) NMC811-p_MW, (c) NMC811-c, (d) NMC811-c_MW, (e) NMC811-d and (f) NMC811-d_MW.

Table 5-4 Capacity retention of the NMC811 powders over 50 cycles at 0.1C.

Sample	Capacity Retention, %
NMC811-p	79
NMC811-p_MW	89
NMC811-c	85
NMC811-c_MW	78
NMC811-d	94
NMC811-d_MW	91

5.4.4 Rate capability

Figure 5-10 compares the rate capability of the 6 samples of the NMC811 investigated in this work

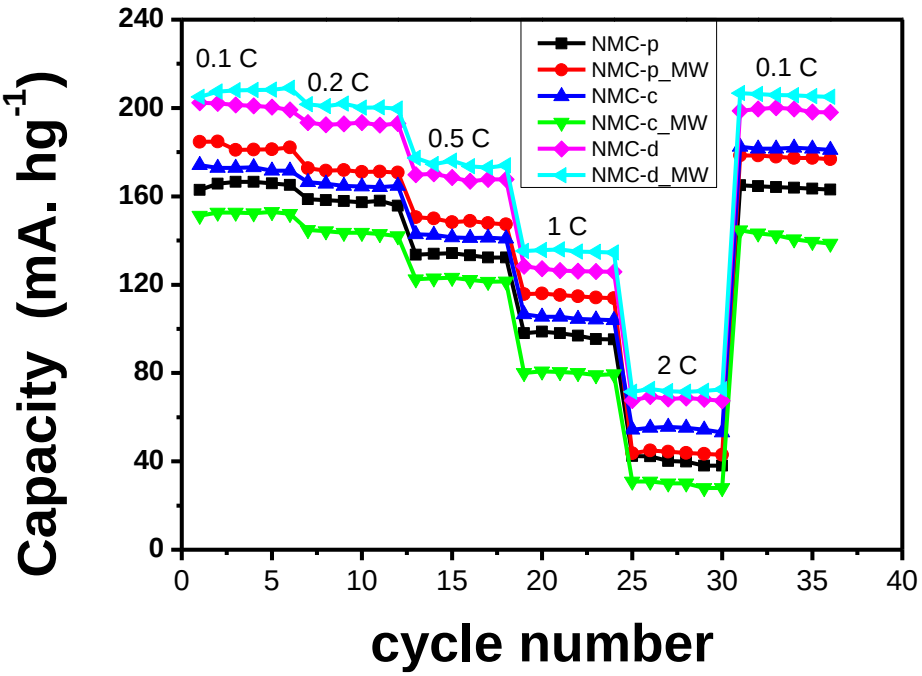


Figure 5-10 Rate performance of the samples of NMC811 at 0.1C, 0.2C, 0.5C, 1C and 2C rates.

The materials NMC811-p, NMC811-p_MW, NMC811-c, NMC811-c_MW, NMC811-d and NMC811d_MW show that they can be withstand both small/slow (0.1 C) and high/fast (2C) current loadings in a reversible manner. Interestingly, the best performing samples in terms of high capacity are the doped and microwave-assisted doped samples (NMC811-d and NMC811-d-MW).

References

1. Tarascon, J.M. and Armand, M., 2001. Issues and challenges facing rechargeable lithium batteries. *Nature*, *414*(6861), pp.359-367.
2. Andre, D., Kim, S.J., Lamp, P., Lux, S.F., Maglia, F., Paschos, O. and Stiaszny, B., 2015. Future generations of cathode materials: an automotive industry perspective. *J. Mater. Chem. A*, *3*(13), pp.6709-6732.
3. Xin, F., Zhou, H., Zong, Y., Zuba, M., Chen, Y., Chernova, N.A., Bai, J., Pei, B., Goel, A., Rana, J. and Wang, F., 2021. What is the role of Nb in nickel-rich layered oxide cathodes for lithium-ion batteries? *ACS Energy Lett.*, *6*(4), pp.1377-1382.
4. Shim, J.H., Kim, C.Y., Cho, S.W., Missiul, A., Kim, J.K., Ahn, Y.J. and Lee, S., 2014. Effects of heat-treatment atmosphere on electrochemical performances of Ni-rich mixed-metal oxide ($LiNi_{0.8}0Co_{0.15}Mn_{0.05}O_2$) as a cathode material for lithium-ion battery. *Electrochim. Acta*, *138*, pp.15-21.
5. Teichert, P., Eshetu, G.G., Jahnke, H. and Figgemeier, E., 2020. Degradation and aging routes of Ni-rich cathode based Li-ion batteries. *Batteries*, *6*(1), p.8.
6. Wang, Q., Shen, C.H., Shen, S.Y., Xu, Y.F., Shi, C.G., Huang, L., Li, J.T. and Sun, S.G., 2017. Origin of structural evolution in capacity degradation for overcharged NMC622 via operando coupled investigation. *ACS Appl. Mater. Interfaces*, *9*(29), pp.24731-24742.
7. Julien, C.M. and Mauger, A., 2018. In situ Raman analyses of electrode materials for Li-ion batteries. *AIMS Mater. Sci.*, *5*(4), pp.650-698.
8. Sicklinger, J., Metzger, M., Beyer, H., Pritzl, D. and Gasteiger, H.A., 2019. Ambient storage derived surface contamination of NCM811 and NCM111: performance implications and mitigation strategies. *J. Electrochem. Soc.*, *166*(12), pp.A2322-A2335.
9. Liu, I.T., Hon, M. H., Teoh, L.G., 2013. Structure and optical properties of CeO_2 nanoparticles synthesized by precipitation. *J. Electron. Mater*.;*42*:pp2536-2541.

CHAPTER 6

Conclusions

6. Conclusions

6.1. General Conclusion

NMC811-p, NMC811-p-MW, NMC811-d, NMC811-d_MW, NMC811-c, and NMC811-c-MW were successfully synthesised using coprecipitation method in a laminar reactor. NI-rich NMC materials NMC622 and NMC811 were successfully modified with Ce through coating with CeO_2 for both, and the latter was also doped with Ce. In addition, microwave treatment was applied to the modified NMC811 electrode materials. For comparative study purposes, microwave treatment was also done on the pristine material.

SEM, TEM and XRD were used to prove that the materials were successfully made. EDS was used to confirm the distribution of Ce ion both in coating and in doping. Treatment with MW further changes the properties of the cathode powders by either causing defects on the surface of the electrode or forming nanoparticles. These changes affect the normal electrochemical behaviour of the electrodes. With both coating and doping there is a decrease in the initial capacity loss. Doping improves capacity retention much more than coating with NMC 811. A combination of doping and microwave treatment produced the most superior material of them all. Coating enhanced the performance of NMC NMC622 a lot. However, Ce-doping achieved much better enhancement results and higher capacities for NMC811.

6.1.1. $LiNi_{0.6}Mn_{0.2}Co_{0.2}O_2/CeO_2$ Electrocatalysts for High performance Lithium- ion batteries

Cathode powder of CeO_2 coated NMC622 was successfully synthesised. Coating was investigated using TEM, SEM. XRD and Raman. EDS proved an even distribution of the coating. Impedance studies further confirmed the presence of a coat since the charge transfer (R_{ct}) of the coated material was initially higher at 199.5 Ω as evidence of a presence of a physical barrier. The XRD showed that the structure remained a well-defined hexagonal layered structure. The coated material had improved electrochemical properties. NMC coated material had faster kinetics, seen by the smaller $\triangle E_p$. This led to excellent discharge capacity of 150 $mAhg^{-1}$ It blocked the H2/H3 phase transitions. Which lowered the first cycle capacity loss by 38 % compared to a loss of 67 % on pristine material. It had excellent capacity retention of 98% over 50 cycles. Coating with CeO_2 promises to be a possible method of enhancing the electrochemical properties of NMC622 cathode material for future-generation Li-ion battery application and it uses little ceria so it does not add a lot to the mass of the material.

6.1.2. $LiNi_{0.8}Mn_{0.1}Co_{0.1}O_2/CeO_2$ Electrocatalysts for High performance Lithium- ion batteries

Samples of NMC811 were successfully synthesised using coprecipitation method in the Taylor-Laminar flow reactor combined with microwave-assisted surface-coating and bulk-doping with 2% CeO_2. The samples investigated are the pristine and microwaved samples (NMC811-p and

NMC811-p_MW), CeO_2-coated and microwaved samples (NMC811-c and NMC811-c_MW), and Ce-doped and microwaved samples (NMC811-d and NMC811-d_MW). Both Ce-doped samples outperformed the others The NMC811-d and NMC811-d_MW outperformed other samples investigated in terms of the first cycle Coulombic efficiency and capacity retention. For example, NMC811-d_MW delivered a capacity of 220 $mAhg^{-1}$ with a capacity retention of 90 % over 50 cycles followed by the non-microwaved NMC811-d. The CeO_2 coating/doping eliminated the H2/H3 phase transition, which is known to lead to microcracks that propagate the degradation process and thus stabilised the surface structure of the NMC811. In summary, CeO_2 treatment offers alternative treatments that can be used to overcome degradation problems that are inherent in Ni-rich cathodes for Li-ion batteries, which can pave the way to applications in electric vehicles and related high-energy demanding applications.

6.2. Future work

There is a need for conducting optimization of the amount of ceria to be used for coating and doping, especially the NMC811. High resolution XPS characterisation will be conducted to investigate the oxidation states of the metals to allow for proper optimization of the synthesis steps. Postmortem studies of the materials after cycling should be considered to inform whether the adopted coating percentages are adequate or not.